REVIEW ARTICLE

Check for updates

Braiding kinetics and spectroscopy in photo-catalysis: the spectro-kinetic approach

Mario J. Muñoz-Batista, [ID] [ab] María M. Ballari,[c] Anna Kubacka,[a] Orlando M. Alfano [ID] *[c] and Marcos Fernández-García [ID] *[a]

The combination of kinetic and spectroscopic tools has become a key scientific methodology for the understanding of catalytic behavior but its application in photocatalysis has inherent difficulties due to the nature of the energy source of the reaction. This review article provides an overview of its use by, first, presenting mechanistically derived kinetic formulations and spectroscopic data handling methods including intrinsic expressions for light and, second, highlighting representative examples of application. To do it we consider universal catalytic systems, particularly (although not exclusively) titania-based materials, and the most frequent hole and/or electron triggered reaction schemes. This review also provides a general framework to pave the way for the future progress of the spectro-kinetic approach in the photocatalysis area.

[a] *Instituto de Catálisis y Petroleoquímica, CSIC, C/Marie Curie, 2, 28049 Madrid, Spain. E-mail: mfg@icp.csic.es*

[b] *Departamento de Química Orgánica, Universidad de Córdoba, Edif. Marie Curie, Ctra Nnal IV-A, Km 396, E14014, Córdoba, Spain*

[c] *Instituto de Desarrollo Tecnológico para la Industria Química (INTEC, UNL-CONICET), Güemes 3450, 3000, Santa Fe, Argentina. E-mail: alfano@santafe-conicet.gov.ar*

1. Introduction

Heterogeneous photocatalysis is an advanced process that uses semiconductors as catalysts and light as an energy source of chemical processes. Basically, a semiconductor is able to absorb light and produce pairs of electron–hole charge carriers. Such charge carrier species travel to the surface of the semiconductor in order to react with adsorbed species and transform them through chemical reactions. Of course, these processes always compete with charge recombination. Photocatalysis is broadly

Dr Mario J. Muñoz-Batista is a researcher/professor from Departamento de Química Orgánica at Universidad de Córdoba, Spain. He received his BA (Chemical Engineering) from CUJAE, Havana, and MS and PhD in Applied Chemistry (2015) from Universidad Autónoma de Madrid – Instituto de Catálisis y Petroleoquímica (CSIC). After two years as a postdoctoral researcher in the Instituto de Catálisis of CSIC, he moved to Cordoba with a Juan de la Cierva postdoctoral scholarship. His current research interests focus on the development and characterization of new catalytic/photocatalytic/electrocatalytic materials, gas phase batch/flow catalytic reactions, biomass/waste valorisation and light–matter interactions and reactor modelling.

Mario J. Muñoz-Batista

Dr María de los Milagros Ballari is a Research Associate at the Institute of Technological Development for the Chemical Industry, INTEC (Universidad Nacional del Litoral-CONICET), and a Teaching Assistant at Universidad Nacional del Litoral, Argentina. She received her degree in Chemical Engineering from Universidad Nacional de Córdoba in 2002 and her PhD in Chemical Engineering from Universidad Nacional del Litoral in 2008, Argentina. Her postdoctoral formation was carried out at the University of Twente and at Eindhoven University of Technology, The Netherlands (2008–2010). Her current research focuses on photocatalytic materials, photoreactor engineering and novel technologies for environmental remediation.

María M. Ballari

This journal is © The Royal Society of Chemistry 2019

Chem. Soc. Rev., 2019, **48**, 637–682 | 637

applied in the degradation and transformation or valorization of organic pollutants,[1–5] reduction of metals or other chemical species,[1–3] production of hydrogen from water splitting or reforming with the help of bio-molecules,[6,7] conversion of CO_2 into high value-added industrial chemicals and hydrocarbon fuels,[8,9] as well as inactivation of biological microorganisms.[10] An immense number of solid semiconductors have shown activity in photo-catalytic processes although only TiO_2 and to some extent ZnO appear as universal systems. For universal systems we can focus on solids which can be used in gas and/or liquid phase processes considering all the above mentioned applications and under a wide range of operating conditions concerning light (intensity, wavenumber, *etc.*) and reaction medium (pH, chemical potential, *etc.*) characteristics.[1–3,6–11] We will focus most of the examples presented in this review

article on the use of universal systems and particularly (although not exclusively) titania materials.

Photoactive semiconductor materials require however improvements for practical or industrial application in many of the above mentioned research fields and a myriad of strategies have been developed. Although this contribution is only secondary concerned with such issues, here we briefly summarize them using a simple method differentiating between "practical" or "first principles" approaches. Such a summary simply attempts to take a glimpse of the immense activity of the field as well as to render a simple outlook into such activity.

A first and rather common approach considers the synthesis of photocatalytic materials. We can call it a "practical" approach which encompasses a number of different procedures and is probably a basic pillar for the majority of the studies published in the field of photocatalysis. Such an approach works along the synthetic pathway of the photocatalytic solids and, in recent times, concerns the production of (most often) hierarchical structures attempting to control the porosity, defect structure and surface and bulk (or generally speaking morphological) characteristics of single phase or composite materials.[1–3,6–10,12] Whether a surface–bulk gradient of physical properties exists and may generate or not surface (yet XRD and Raman silent) phase(s) is always a complex task to realize and makes the border between single and composite materials diffuse. In the case of composite structures, these are synthesized with control of the structural and electronic properties of the interface(s) among components as an additional issue to enhance photo-activity.[13]

Typical modern photo-catalytic systems can be high surface area, controlled surface to bulk ratio (rendering spherical or elongated particles, belts, sheets, and other morphologies), and/or controlled porosity solid(s). Also, they can have a specific polymorph (case of titania, the anatase polymorph for example),

Anna Kubacka

Dr Anna Kubacka is "Científico Titular" at the Institute of "Catálisis y Petroleoquímica" (CSIC, Spain). She serves as an editor or is part of the editorial board of several journals, books as well as scientific monographs published in SCI journals. Her research has yielded more than 100 peer reviewed publications, 10 book chapters and monographs and 7 patents. Her current work focuses on heterogeneous thermal- and photo-catalysis on single or
mixed oxides and related materials for environmental and fine chemistry applications as well as on oxide–polymer nanocomposites with advanced properties.

Orlando M. Alfano

Prof. Orlando Mario Alfano graduated as a Chemical Engineer (1976) from Universidad Nacional del Litoral (UNL), Argentina, and received his PhD in Chemical Engineering (1984) from the same University. Presently, he is a member of the Institute of Technological Development for the Chemical Industry (INTEC), Full Professor at UNL and Superior Researcher Ad-Honorem of the National Council of Scientific and Technical Research
of Argentina (CONICET). His main research interest focuses on Advanced Oxidation Processes for Water and Air Remediation, with special application on Photocatalytic and Photo-Fenton Solar Reactors. He has authored more than 190 peer-reviewed articles in indexed international journals and book chapters.

Marcos Fernández-García

Prof. M. Fernández-García is a full Professor at the Institute of "Catálisis y Petroleoquímica" (CSIC, Spain). During his carrier he received a European Fellowship by the Royal Society and several prices such as the Wolkswagen-CSIC, served as a member of editorial boards of several journals of catalysis and nano-materials and was part of the scientific panels and/or the advisory board of the Diamond (DLS) and European (ESRF)
Synchrotrons. He is the author of more than 250 SCI publications and 10 patents. His research interests now include gas/liquid catalytic/photocatalytic systems related to chemical/biological environmental and human health protection as well as added-value chemical processes.

or created by doping with metal and/or non-metal ions or solid solutions. All these typical strategies were applied in most cases to "single" phase systems to improve activity. For composite systems we can mention the construction of specific hetero-junctions or contacts (core–shell, 2D–3D, *etc.*), and (metal or oxide) plasmonic photocatalysts as two of the most successful ways attempted to improve photo-catalytic performance.[1–3,6–10,12–16] The synthesis is always complemented in research contributions with theoretical simulation and experimental characterization of the materials in order to shed light into the physico-chemical characteristics of the photocatalytic solids and the interpretation of the photocatalytic properties.[17] Needless to mention, controlling the synthesis of the semiconductor attempts to modulate or control a significant number of physico-chemical variables of the photocatalytic process. As the most common properties claimed to be modulated or controlled we can enumerate: (i) the wavelength range for photon absorption, from UV to near IR regions; (ii) the recombination of charge carriers; and (iii) thermodynamic aspects related to band gap energy as well as valence and conduction band edge positions.

Alternatively to such an approach, we can enumerate other ways of attacking the problem and focusing on understanding the specific physico-chemical issues pertaining to all photocatalytic processes. The first of them concerns light absorption and handling. The theoretical basis of light–matter interactions has been summarized in recent reviews.[18,19] From an experimental viewpoint, results from the application of vibrational and optical tools devoted to the understanding of the light–matter interaction and particularly of charge carriers generated after light absorption have been summarized in the reviews of Majima and others.[20,21] The thermodynamics and kinetics bases of the photo-catalytic systems have also been analyzed from a fundamental point of view in recent contributions.[22] Finally, the surface chemistry of photocatalytic materials has also been analyzed in review articles.[21] From this brief enumeration one can observe that typical tools of thermal catalysis concerning the joint application of kinetic and (*in situ*) spectroscopic tools are not very common or have been significantly less explored in photo-catalysis.

More specifically, kinetics analyses in photo-catalysis are relatively common but mostly based on *ad hoc* or phenomenological approaches. Although a significant number of valuable review articles have appeared for liquid or gas phase photo-catalytic reactions,[23–26] they use Langmuir or other types of mechanisms lacking first principles grounds. This would happen in two ways. First and contrarily to most studies in the field of thermal or classical catalysis, they usually do not define the elemental (corresponding to real physical elemental processes) steps sustaining the mechanism. Second, equally important, and also general, they do not include rigorously light into the mechanism and certainly into the corresponding kinetic studies. Both facts inhibit or strongly limit the potential use of kinetic results to combine information with spectroscopic tools.

Similarly, the use of spectroscopic tools in photocatalysis is mostly restricted to taking snapshots at specific states, typically initial and post-reaction stages, of the solid catalysts rather than a real *in situ* or operando analysis of the materials.[1–3,6–10] However, few exception can be highlighted; in particular,

the use of vibrational, electronic and optical tools to analyze charge carrier species generated upon light excitation and in the presence of relevant atmospheres.[7,20,21,27] Also, the analysis of the evolution of reactants under light excitation has been followed using mostly vibrational, X-ray absorption and optical spectroscopies.[28,29] All these review works summarize the most interesting results but rarely provide key information for fully interpreting the mechanism and kinetic behavior of photo-catalysts.

As mentioned, a powerful tool, extensively used in conventional catalysis to progress in the understanding of catalytic solids, corresponds to the so-called spectro-kinetic approach. Braiding kinetic and spectroscopic tools provides powerful insights and allows joining the information coming from both the reactant and solid perspectives, ultimately uncovering the elemental steps controlling the reaction mechanisms. A complete knowledge of such issues corresponds, as well known, to critical information to interpret catalytic behavior and therefore to provide the basis and shape the future developments of the research field. The spectro-kinetic analysis of photo-catalytic processes is at the core of the present contribution. In the photo-catalytic field, such a research field is at its infancy but valuable works have already been presented. Therefore, in the next section (Section 2) of this review, we present the main guidelines to construct intrinsic mechanisms considering rigorously the effect of the energy source and derived rate equations for light-triggered reactions in liquid and gas phase media. We focus on oxidation reactions as the more representative example although the mathematical formulation can be applied to all photo-catalytic reactions. Simplified approaches are derived from these mathematical expressions and their value and limitations considered. Section 3 presents the mathematical treatment of the photon absorption rate as the most general way of introducing light into kinetic expressions. Section 4 introduces the spectroscopic analysis of catalytic solids and divides the currently available studies into those contributions taking care of the electron and hole generation and fate and those concerning the detection of intermediate species occurring in photo-catalytic reactions. As mentioned *in situ* or operando reports are discussed and emphasized over others considering more static measurement conditions. Section 5 summarizes the spectro-kinetic studies currently available in the literature as well as presents key ideas from kinetics and spectroscopy which may boost the activity in the field and can promote the true understanding of photocatalytic mechanisms and their kinetically relevant steps. This section also takes care and reviews both the role of charge species as well as the chemical species originating from reactants. Finally, in Section 6 we summarize the most exciting information coming from the studies reviewed and provide some clues for the future of the field.

2. Mechanistically derived photocatalytic oxidation kinetics

2.1. Empirical photocatalytic kinetic expressions

In the literature simple reaction rate expressions can be very often found to describe the results of empirical photocatalytic

This journal is © The Royal Society of Chemistry 2019

Chem. Soc. Rev., 2019, **48**, 637–682 | **639**

Table 1 Empirical photocatalytic kinetic expressions

Model	Kinetic equation	Eqn	Ref.
Langmuir–Hinshelwood	$r_X = -\dfrac{kK[X]}{1 + K[X]}$	(1)	30 and 31
Simplified Langmuir–Hinshelwood	$r_X = -kK[X]$	(2)	32 and 33
Competitive Langmuir–Hinshelwood	$r_X = -\dfrac{kK[X]}{1 + K[X] + \sum_i K_i[Y_i]}$	(3)	44 and 45
Langmuir–Hinshelwood including light intensity dependence	$r_X = -k'I^n \dfrac{K[X]}{1 + K[X]}$	(4)	36 and 46
Competitive Langmuir–Hinshelwood including light intensity dependence	$r_X = -k'I^n \dfrac{K[X]}{1 + K[X] + \sum_i K_i[Y_i]}$	(5)	34
Langmuir–Hinshelwood including light intensity and humidity dependence	$r_X = -k''I^n \left[1 + f_H \left([H_2O] - [H_2O]^L \right) \right] \dfrac{K[X]}{1 + K[X]}$	(6)	37 and 38
Bimolecular Langmuir–Hinshelwood including light intensity dependence	$r_X = -k'I^n \left(\dfrac{K_1[X]}{1 + K_1[X] + K_2[H_2O]} \right)\left(\dfrac{K_4[H_2O]}{1 + K_3[X] + K_4[H_2O]} \right)$	(7)	35
Langmuir–Hinshelwood including LVRPA dependence	$r_X = -k' \left(\int_\lambda e_\lambda^a d\lambda \right)^n \dfrac{K[X]}{1 + K[X]}$	(8)	39
Quadratic-type	$r_X = -k'[X][O_2] \left(\sqrt{1 + \dfrac{2\int_\lambda e_\lambda^a d\lambda}{k'[X][O_2]C_{cat}}} - 1 \right)$	(9)	41–43

oxidation kinetic studies. In these cases, the presented results cannot be generalized and have limited scope. Yet they are very simple to apply and appealing in this sense.

Following a classical approach, the Langmuir–Hinshelwood mechanism has been used in several contributions (eqn (1), Table 1).[30,31] Besides, if the adsorption constant and concentration are much less than 1, a pseudo-first-order expression (simplified Langmuir–Hinshelwood form) is commonly utilized (eqn (2)).[32,33] On the other hand, when reaction intermediates are formed and compete for the same photocatalytic active sites, a competitive Langmuir–Hinshelwood form may be applied (eqn (3)).

The effect of the incident light irradiance on photocatalytic degradation has been previously analyzed using a reaction constant which is a function of light intensity ($k = k'I^n$) (eqn (4)–(7) in Table 1).[34,35] A value of 0.38 for the exponent n was obtained for photocatalytic degradation of acetone.[36] A similar approach was used for the photocatalytic removal of formaldehyde from air,[37,38] with $n = 1$ at low I, $0 < n < 1$ at medium I or $n = 0$ at high I. Also, in these last studies a dependence on the water vapor concentration [H₂O] was included (eqn (6)), where $[H_2O]^L$ is the water vapor concentration at the limit of the humidity regimen (low, medium or high humidity). On the other hand, to consider the humidity effect on the gas phase photocatalytic reaction rate, a form of the bimolecular Langmuir–Hinshelwood mechanism was considered in eqn (7).[35]

The explicit photon absorption effects are considered in a Langmuirian dependence of the reaction rate[39] as it was postulated previously during a mechanistic kinetic study.[40] In eqn (8) of Table 1, k' is a kinetic constant independent of photon absorption. This constant takes into account the primary quantum yield for electron–hole generation. $\int_\lambda e_\lambda^a d\lambda$ is the Local Volumetric Rate of Photon Absorption (LVRPA) averaged across the useful spectrum of the incident light. According to the

analysis of the authors, the exponent n depends on the efficiency of electron–hole formation and recombination at the catalyst's surface and takes a value between 0.5 and 1 provided the reaction is kinetically controlled.

Finally, we would like to highlight the semi-empirical approach used by Camera-Roda et al.[41,42] based on the work of Minero and Vione.[43] This approach uses one kinetic parameter quadratic-type model applicable to photocatalytic reactions in slurry reactors. In eqn (9) of Table 1, C_{cat} is the catalyst load and [O₂] the concentration of dissolved oxygen.

2.2. Photocatalytic oxidation mechanism

As opposed to phenomenological models, the setting up of a first principles kinetic formalism requires as the initial task the settlement of a general photocatalytic mechanism.

A simplified yet general photocatalytic mechanism for reactions and, particularly, concerning a general oxidation mechanism is proposed in Table 2. The single and elemental steps presented here are normally accepted for heterogeneous photocatalysis for the decontamination of a X compound, forming stable intermediates called Y$_i$.[24,26,47] The oxidation of the main compound X can occur basically through three pathways: (i) direct attack of the semiconductor hole formed during the irradiation step, (ii) oxidation by hydroxyl radicals formed during the hole trapping by water or hydroxyl ions, and (iii) reaction with the superoxide radical formed during the electron trapping by oxygen. Note that steps (i) and (ii) are also involved in mechanisms considering other chemical reactions such as the use of sacrificial molecules in the production of hydrogen. Thus, they are also of interest in such types of mechanism. The physico-chemical bases sustaining the generation of these three types of chemical species have been summarized in a recent review of Nosaka et al.[27] In subsequent sections of this review we will focus on their generation and understanding as tools in spectro-kinetic studies.

Table 2 General photocatalytic oxidation mechanism

Reaction step	Const.
Activation	
Photocatalyst + $h\nu \rightarrow$ h$^+$ + e$^-$	
Adsorption	
Site + X $\leftrightarrow$ X$_{ads}$	K_1
Site + Y$_i$ $\leftrightarrow$ Y$_{i,ads}$	K_{2i}
Site + H$_2$O $\leftrightarrow$ H$_2$O$_{ads}$	K_3
Site$_{O_2}$ + O$_2$ $\leftrightarrow$ O$_{2,ads}$	K_4
Electron capture	
O$_{2,ads}$ + e$^-$ $\rightarrow$ O$_2$$^{\bullet-}$	k_1
Hole trap	
H$_2$O$_{ads}$ + h$^+$ $\rightarrow$ HO$^\bullet$ + H$^+$	k_2
Recombination	
h$^+$ + e$^-$ $\rightarrow$ Heat	k_3
Contaminant oxidation	
X$_{ads}$ + h$^+$ $\rightarrow$ Y$_{ads}$	k_4
X$_{ads}$ + HO$^\bullet$ $\rightarrow$ Y$_{ads}$	k_5
X$_{ads}$ + O$_2$$^{\bullet-}$ $\rightarrow$ Y$_{ads}$	k_6
Stable intermediate oxidation	
Y$_{i,ads}$ + h$^+$ $\rightarrow$ Z$_{i,ads}$	k_{7i}
Y$_{i,ads}$ + HO$^\bullet$ $\rightarrow$ Z$_{i,ads}$	k_{8i}
Y$_{i,ads}$ + O$_2$$^{\bullet-}$ $\rightarrow$ Z$_{i,ads}$	k_{9i}
Termination of radicals	
HO$^\bullet$ + M $\rightarrow$ Products	k_{10}
O$_2$$^{\bullet-}$ + M $\rightarrow$ Products	k_{11}

The three pathways mentioned involving the reactant evolution can occur simultaneously and can compete with each other. However, normally, but not always, one of them is proposed as a dominant pathway in the photocatalytic oxidation process. On the other hand, the proposed general mechanism considers the radicals' termination reactions and the recombination reaction between holes and electrons that compete with the oxidation reaction.

2.3. Mechanistically derived photocatalytic oxidation kinetic models

2.3.1. Irradiated initiation step rate.
Any photochemical reaction begins with the absorption of a photon by a molecule that gives rise to some form of an excited state. In photocatalytic processes, it has been well established that in a single photon absorption process, the rate of the photocatalyst activation step (primary event) is proportional to the rate of energy absorbed. The proportionality constant for monochromatic radiation is the primary reaction quantum yield:

$$\Phi_\lambda = \frac{\text{Pair electron–hole formed per unit time}}{\text{Photons of wavelength } \lambda \text{ absorbed by the catalyst per unit time}} \quad (10)$$

The superficial rate of electron–hole generation, r_g, for all wavelengths where the photocatalyst absorbs radiation, is given by:[48]

$$r_g = \int_\lambda \Phi_\lambda e_\lambda^{a,s} d\lambda = \bar{\Phi}_\lambda \int_\lambda e_\lambda^{a,s} d\lambda \quad (11)$$

where $e_\lambda^{a,s}$ represents the Local Superficial Rate of Photon Absorption (LSRPA) and $\bar{\Phi}_\lambda$ is the primary quantum yield averaged over the wavelength range.

Also, the initiation rate can be expressed as a function of the Local Volumetric Rate of Photon Absorption (LVRPA, e_λ^a):[40]

$$r_g = \frac{\int_\lambda \Phi_\lambda e_\lambda^a d\lambda}{a_V} = \frac{\bar{\Phi}_\lambda}{a_V} \int_\lambda e_\lambda^a d\lambda \quad (12)$$

where a_V is the total active catalytic surface per unit volume of the reacting system. For slurry systems a_V is the product of the catalyst load C_{cat} and the specific surface area of the photocatalyst S_g.

2.3.2. Adsorption equilibrium.
Performing a balance of sites for the water, contaminant and intermediates, assuming the adsorption is in equilibrium and these species are competing for the same active sites, the adsorbed superficial concentration (eqn (13)–(15) in Table 3) can be expressed as a function of the bulk reaction space volumetric concentrations (Langmuir competitive adsorption model).

On the other hand, assuming that oxygen is absorbed over different active sites[47,49] eqn (16) is obtained in Table 3.

For low species concentrations, linear adsorption isotherms are recovered as limiting cases of eqn (13)–(16), obtaining eqn (17)–(20) in Table 3.

2.3.3. Photocatalytic oxidation rate.
According to the mass action law and the photocatalytic reaction mechanism given in Table 2, the oxidation superficial reaction rate of contaminant X considering different oxidation pathways is:

$$r_X = -k_4[X_{ads}][h^+] - k_5[X_{ads}][HO^\bullet] - k_6[X_{ads}][O_2^{\bullet-}] \quad (21)$$

As previously mentioned, normally only one of the oxidation pathways shown in Table 2 can be considered as the dominant step in a certain photocatalytic system. Thus, under the last posed hypothesis, the kinetic models considering the three oxidation pathways separately will be developed. Additionally, the reaction rate expressions with and without formation of stable intermediates will be worked out.

2.3.3.1. Hydroxyl radical oxidation without stable intermediate formation. The most frequent situation in photocatalysis is that the predominant oxidation reaction is the attack of hydroxyl radicals. Then:

$$r_X = -k_5[X_{ads}][HO^\bullet] \quad (22)$$

In order to evaluate the degradation rate of compound X, the hydroxyl radical concentration should be expressed in terms of measurable variables. Therefore, the superficial rate of the appearance and disappearance of the hydroxyl radical is proposed and, considering its very short lifetime, the Micro Steady State (MSS) approximation can be applied:

$$r_{HO^\bullet} = k_2[H_2O_{ads}][h^+] - k_5[X_{ads}][HO^\bullet] - k_{10}[M][HO^\bullet] = 0 \quad (23)$$

Table 3 Photocatalytic adsorption models

Model	Species	Equation	Eqn
Langmuir competitive adsorption	Main compound	$[X_{ads}] = \dfrac{K_1[\text{Sites}_T][X]}{1 + K_1[X] + \sum_i K_{2i}[Y_i] + K_3[H_2O]}$	(13)
	Stable intermediates	$[Y_{i,ads}] = \dfrac{K_{2i}[\text{Sites}_T][Y_i]}{1 + K_1[X] + \sum_i K_{2i}[Y_i] + K_3[H_2O]}$	(14)
	Water	$[H_2O_{ads}] = \dfrac{K_3[\text{Sites}_T][H_2O]}{1 + K_1[X] + \sum_i K_{2i}[Y_i] + K_3[H_2O]}$	(15)
Langmuir non-competitive adsorption	Oxygen	$[O_{2,ads}] = \dfrac{K_4[\text{Sites}_{O_2,T}][O_2]}{1 + K_4[O_2]}$	(16)
Linear adsorption	Main compound	$[X_{ads}] = K_1[\text{Sites}_T][X]$	(17)
	Stable intermediates	$[Y_{i,ads}] = K_{2i}[\text{Sites}_T][Y_i]$	(18)
	Water	$[H_2O_{ads}] = K_3[\text{Sites}_T][H_2O]$	(19)
	Oxygen	$[O_{2,ads}] = K_4[\text{Sites}_{O_2,T}][O_2]$	(20)

Solving for the hydroxyl radical concentration in the last expression:

$$[HO^\bullet] = \frac{k_2[H_2O_{ads}][h^+]}{k_5[X_{ads}] + k_{10}[M]} \tag{24}$$

Following the same procedure for the other unstable species of eqn (24), the next expression can be derived for the hole concentration:

$$[h^+] = \frac{r_g}{k_2[H_2O_{ads}] + k_3[e^-]} \tag{25}$$

In the same way, the electron concentration involved in eqn (25) can be obtained:

$$[e^-] = \frac{r_g}{k_1[O_{2,ads}] + k_3[h^+]} \tag{26}$$

Substituting eqn (26) into eqn (25) a quadratic equation for the hole concentration is obtained:

$$[h^+] = -\frac{k_1[O_{2,ads}]}{2k_3}\left(1 \pm \sqrt{1 + \frac{4k_3 r_g}{k_1 k_2[H_2O_{ads}][O_{2,ads}]}}\right) \tag{27}$$

Substituting eqn (27) into eqn (24), and then the resulting hydroxyl radical concentration into eqn (22), the final expression of the oxidation rate is illustrated in Table 4 (eqn (28)). Note that the negative sign of the quadratic equation solution (eqn (27)) is chosen to get a null reaction rate when there is no electron and hole generation ($r_g = 0$).

2.3.3.2. Direct hole attack without stable intermediate formation. If the contaminant X is directly attacked by the semiconductor hole:

$$r_X = -k_4[X_{ads}][h^+] \tag{29}$$

Considering the MSS approximation for holes, and assuming that they are only trapped by compound X and not by water:

$$[h^+] = \frac{r_g}{k_4[X_{ads}] + k_3[e^-]} \tag{30}$$

Combining eqn (30) and (26) and solving the hole concentration:

$$[h^+] = -\frac{k_1[O_{2,ads}]}{2k_3}\left(1 \pm \sqrt{1 + \frac{4k_3 r_g}{k_1 k_4[X_{ads}][O_{2,ads}]}}\right) \tag{31}$$

It should be noticed that the mathematical functionality of eqn (32) with the contaminant X concentration differs from eqn (28).

2.3.3.3. Superoxide radical oxidation without stable intermediate formation. In certain systems working with visible light photocatalysts, the step responsible for the contaminant degradation is the superoxide radical attack:[50]

$$r_X = -k_6[X_{ads}][O_2^{\bullet-}] \tag{33}$$

As this radical also has a very short lifetime, the MSS approximation can be applied:

$$r_{O_2^{\bullet-}} = k_1[O_{2,ads}][e^-] - k_6[X_{ads}][O_2^{\bullet-}] - k_{11}[M][O_2^{\bullet-}] = 0 \tag{34}$$

Solving the superoxide radical concentration in eqn (34):

$$[O_2^{\bullet-}] = \frac{k_1[O_{2,ads}][e^-]}{k_6[X_{ads}] + k_{11}[M]} \tag{35}$$

Substituting eqn (25) into eqn (26) and solving the electron concentration:

$$[e^-] = -\frac{k_2[H_2O_{ads}]}{2k_3}\left(1 - \sqrt{1 + \frac{4k_3 r_g}{k_1 k_2[H_2O_{ads}][O_{2,ads}]}}\right) \tag{36}$$

Replacing eqn (36) into eqn (35), and then the resulting superficial superoxide radical concentration into eqn (33), the photocatalytic oxidation rate is obtained (see Table 4 and eqn (37)).

The kinetic expression for the X compound degradation through the superoxide radical (eqn (37)) has the same parameter dependence as eqn (28) derived from the hydroxyl radical attack mechanism, which differs only from the kinetic constants involved.

Table 4 Photocatalytic oxidation rates for different pathways

Pathway	Formation of stable intermediates	Photocatalytic oxidation rates	Eqn
Hydroxyl radical attack	No	$r_X = \dfrac{k_5[X_{ads}]k_1[O_{2,ads}]k_2[H_2O_{ads}]\left(1 - \sqrt{1 + \dfrac{4k_3 r_g}{k_1 k_2 [H_2O_{ads}][O_{2,ads}]}}\right)}{2k_3(k_5[X_{ads}] + k_{10}[M])}$	(28)
	Yes	$r_X = \dfrac{k_5[X_{ads}]k_1[H_2O_{ads}]k_2[O_{2,ads}]\left(1 - \sqrt{1 + \dfrac{4k_3 r_g}{k_1 k_2 [H_2O_{ads}][O_{2,ads}]}}\right)}{2k_3\left(k_5[X_{ads}] + \sum_i k_{8i}[Y_{i,ads}] + k_{10}[M]\right)}$	(39)
		$r_{Y_i} = \dfrac{(k_{8i}[Y_{i,ads}] - k_5[X_{ads}])k_1[H_2O_{ads}]k_2[O_{2,ads}]\left(1 - \sqrt{1 + \dfrac{4k_3 r_g}{k_1 k_2 [H_2O_{ads}][O_{2,ads}]}}\right)}{2k_3\left(k_5[X_{ads}] + \sum_i k_{8i}[Y_{i,ads}] + k_{10}[M]\right)}$	(41)
Direct hole attack	No	$r_X = \dfrac{k_4[X_{ads}]k_1[O_{2,ads}]\left(1 - \sqrt{1 + \dfrac{4k_3 r_g}{k_1 k_4 [X_{ads}][O_{2,ads}]}}\right)}{2k_3}$	(32)
Superoxide radical attack	No	$r_X = \dfrac{k_6[X_{ads}]k_1[H_2O_{ads}]k_2[O_{2,ads}]\left(1 - \sqrt{1 + \dfrac{4k_3 r_g}{k_1 k_2 [H_2O_{ads}][O_{2,ads}]}}\right)}{2k_3(k_6[X_{ads}] + k_{11}[M])}$	(37)

2.3.3.4. Formation and degradation of stable intermediates through the hydroxyl radical attack. The formation and degradation of stable intermediates Y_i from the photocatalytic oxidation of compound X through the hydroxyl radical attack pathway will be considered. Therefore, taking into consideration that the hydroxyl radical is also consumed during the reaction with stable intermediates Y_i, and applying the MSS approximation:

$$[HO^\bullet] = \frac{k_2[H_2O_{ads}][h^+]}{k_5[X_{ads}] + \sum_i k_{8i}[Y_{i,ads}] + k_{10}[M]} \quad (38)$$

Replacing eqn (27) into eqn (38), and then into eqn (22), the expression of the X superficial reaction rate considering the formation of intermediates Y_i results in eqn (39) shown in Table 4.

On the other hand, the net superficial reaction rate of compound Y_i can be expressed as:

$$r_{Y_i} = k_5[X_{ads}][HO^\bullet] - k_{8i}[Y_{i,ads}][HO^\bullet] \quad (40)$$

Replacing the hydroxyl radical concentration in eqn (40), eqn (41) in Table 4 is obtained.

2.3.4. Photocatalytic kinetic models in the liquid phase. A very detailed overview of 10 different kinetics-based reaction mechanisms in aqueous phase photocatalytic slurries was carried out by Mills *et al.*[23] In the present review, only the first principles kinetic expressions derived from the photocatalytic reaction mechanism proposed in Table 2 will be explored and the principal publications that have applied them. As mentioned, this is based on the fact that useful results to understand spectroscopies studies would only come from kinetic expressions having intrinsic treatment of light.

2.3.4.1. Hydroxyl radical attack. When the photocatalytic oxidation kinetic study in slurry liquid phase systems is carried out,

the most frequently made assumptions are: (i) constant oxygen concentration, (ii) constant water or hydroxyl ion concentration, and (iii) no adsorption competition between water and other species.[51] Therefore and according to the last hypothesis, eqn (13) and (14) for the adsorption model of the main pollutant and intermediates can be simplified to:

$$[X_{ads}] = \frac{K_1[Sites_T][X]}{1 + K_1[X] + \sum_i K_{2i}[Y_i]} \quad (42)$$

$$[Y_{i,ads}] = \frac{K_{2i}[Sites_T][Y_i]}{1 + K_1[X] + \sum_i K_{2i}[Y_i]} \quad (43)$$

Then, considering the assumptions stated above and applying eqn (42) and (43) and eqn (12) for the irradiated initiation rate, eqn (39) and (41) can be expressed as eqn (44) and (45) in Table 5 with their respective constant kinetic parameters defined in eqn (46)–(50).

The mathematical equations for the superficial reaction rates (eqn (44) and (45)) were developed by Satuf *et al.*[51] and Manassero *et al.*[52] working with TiO$_2$ slurry systems for degrading organic compounds with the apparition of stable intermediates. Also, Marugan *et al.*[53] have derived the same mathematical expression for cyanide photocatalytic oxidation rate, but proposing a different reaction mechanism; thus, the kinetic parameters are defined by other reaction rate constants.

2.3.4.1.1. Limiting cases. • Low concentration of contaminant and intermediates. This is a common hypothesis assumed for contaminants present in water. The resulting superficial reaction rate considering that $\alpha_3[X] + \sum_i \alpha_i[Y_i] \ll 1$ follows first order kinetics with respect to substrates X and Y_i (eqn (51) and (52) of Table 5).[51,52]

This journal is © The Royal Society of Chemistry 2019

Chem. Soc. Rev., 2019, **48**, 637–682 | 643

Table 5 Photocatalytic oxidation rates for liquid phase reactions

Pathway	Case	Photocatalytic reaction rate	Eqn	Ref.
Hydroxyl radical attack	Complete expression	$r_X = \dfrac{\alpha_1[X]\left(1 - \sqrt{1 + \frac{\alpha_2}{a_V}\int_\lambda e_\lambda^a d\lambda}\right)}{1 + \alpha_3[X] + \sum_i \alpha_i[Y_i]}$	(44)	51–53, 55 and 56
		$r_{Y_i} = \dfrac{(\alpha_4[Y_i] - \alpha_1[X])\left(1 - \sqrt{1 + \frac{\alpha_2}{a_V}\int_\lambda e_\lambda^a d\lambda}\right)}{1 + \alpha_3[X] + \sum_i \alpha_i[Y_i]}$	(45)	
		$\alpha_1 = \dfrac{k_5 k_1 k_2 [H_2O_{ads}][O_{2,ads}] K_1 [Sites_T]}{2k_3 k_{10}[M]}$	(46)	
		$\alpha_2 = \dfrac{4k_3 \bar{\Phi}_\lambda}{k_1 k_2 [H_2O_{ads}][O_{2,ads}]}$	(47)	
		$\alpha_3 = \dfrac{k_5 K_1[Sites_T] + k_{10}[M]K_1}{k_{10}[M]}$	(48)	
		$\alpha_i = \dfrac{[Sites_T]k_{8i}K_{2i} + k_{10}[M]K_{2i}}{k_{10}[M]}$	(49)	
		$\alpha_4 = \dfrac{k_{8i}k_1 k_2 [H_2O_{ads}][O_{2,ads}] K_{2i}[Sites_T]}{2k_3 k_{10}[M]}$	(50)	
	Low concentration	$r_X = \alpha_1[X]\left(1 - \sqrt{1 + \frac{\alpha_2}{a_V}\int_\lambda e_\lambda^a d\lambda}\right)$	(51)	51, 52 and 55
		$r_{Y_i} = (\alpha_4[Y_i] - \alpha_1[X])\left(1 - \sqrt{1 + \frac{\alpha_2}{a_V}\int_\lambda e_\lambda^a d\lambda}\right)$	(52)	
	High irradiation level	$r_X = -\dfrac{\alpha_1[X]\sqrt{\frac{\alpha_2}{a_V}\int_\lambda e_\lambda^a d\lambda}}{1 + \alpha_3[X] + \sum_i \alpha_i[Y_i]}$	(53)	54 and 55
		Low concentration : $r_X = -\alpha_1[X]\sqrt{\frac{\alpha_2}{a_V}\int_\lambda e_\lambda^a d\lambda}$	(54)	40 and 47
	Low irradiation level	$r_X = -\dfrac{\alpha_1 \alpha_2[X]\int_\lambda e_\lambda^a d\lambda}{2a_V\left(1 + \alpha_3[X] + \sum_i \alpha_i[Y_i]\right)}$	(55)	56
		Low concentration : $r_X = -\dfrac{\alpha_1 \alpha_2[X]}{2a_V}\int_\lambda e_\lambda^a d\lambda$	(56)	
	Linear adsorption isotherms	$r_X = \dfrac{\alpha_1[X]\left(1 - \sqrt{1 + \frac{\alpha_2}{a_V}\int_\lambda e_\lambda^a d\lambda}\right)}{1 + \alpha_3'[X] + \sum_i \alpha_i'[Y_i]}$	(57)	
		$r_{Y_i} = \dfrac{(\alpha_4[Y_i] - \alpha_1[X])\left(1 - \sqrt{1 + \frac{\alpha_2}{a_V}\int_\lambda e_\lambda^a d\lambda}\right)}{1 + \alpha_3'[X] + \sum_i \alpha_i'[Y_i]}$	(58)	
		$\alpha_3' = \dfrac{k_5 K_1[Sites_T]}{k_{10}[M]}$	(59)	
		$\alpha_i' = \dfrac{[Sites_T]k_{8i}K_{2i}}{k_{10}[M]}$	(60)	
Direct hole attack	Complete expression	$r_X = \dfrac{\alpha_1[X]}{1 + K_1[X]}\left(1 - \sqrt{1 + \frac{\alpha_2 \int_\lambda e_\lambda^a d\lambda (1 + K_1[X])}{a_V[X]}}\right)$	(64)	58–60
		$\alpha_1 = \dfrac{k_4 k_1 [O_{2,ads}] K_1 [Sites_T]}{2k_3}$	(65)	
		$\alpha_2 = \dfrac{4k_3 \bar{\Phi}_\lambda}{k_4 k_1 [O_{2,ads}] K_1 [Sites_T]}$	(66)	
	Linear adsorption isotherms	$r_X = \alpha_1[X]\left(1 - \sqrt{1 + \frac{\alpha_2 \int_\lambda e_\lambda^a d\lambda}{a_V[X]}}\right)$	(67)	58–60 41–43 with $\bar{\Phi}_\lambda = 1$
	High irradiation level	$r_x = -\alpha_1 \sqrt{\dfrac{\alpha_2 \int_\lambda e_\lambda^a d\lambda[X]}{a_V}}$	(68)	60
	Low irradiation level	$r_X = -\dfrac{\alpha_1 \alpha_2}{2a_V}\int_\lambda e_\lambda^a d\lambda$	(69)	60 57 for intermediate generation rate

This journal is © The Royal Society of Chemistry 2019

● High irradiation level. When the LVRPA gets high levels in the reacting system, then $\frac{\alpha_2}{a_V}\int_\lambda e_\lambda^a d\lambda \gg 1$ and $\sqrt{\frac{\alpha_2}{a_V}\int_\lambda e_\lambda^a d\lambda} \gg 1$. In this case, eqn (44) can be transformed into eqn (53) of Table 5,[54] and eqn (51) for low contaminant concentration can be written as eqn (54) of the same table. The square root dependence on the LVRPA is obtained, as was predicted in Turchi and Ollis[47] and Alfano et al.[40] for high irradiation levels.

● Low irradiation level. For low LVRPA and performing a Taylor's series expansion of the square root in eqn (44) or in eqn (51) for low X concentration, eqn (55) and (56) are obtained in Table 5, respectively. Thus, the linear dependence of the reaction rate on the LVRPA is obtained.

● Linear adsorption isotherms. This is also a common hypothesis taken when the contaminant concentration is low and no water competition for the active sites exists. Assuming linear adsorption equilibrium (eqn (17)–(20)), the same kinetic equations for the pollutant and intermediate degradation rate (eqn (44) and (45)) are obtained, but the definition of the kinetic parameters α_3 and α_i is simplified containing only the first term in the numerator (see eqn (57)–(60) of Table 5).

2.3.4.1.2. Others approaches. Several works have assumed linear equilibrium adsorption for the species involved.[40,54–57] However, it should be noticed that Alfano et al.[40] have followed the reaction mechanism and methodology proposed by Turchi and Ollis[47] where the hole trapping by water was considered as a reversible reaction. Therefore, the dependence on the pollutant concentration in the non-simplified reaction rate differs from eqn (44). On the other hand, Alfano et al.[40] and Tolosana-Moranchel et al.[56] during the derivation of their kinetic expressions have proposed four possible oxidation pathways of the pollutant by the hydroxyl radical[47] and they have assumed the hypothesis that the electrons and holes have equal concentrations. Despite that, the same functionality of eqn (44) for the reaction rate of phenol photodegradation was obtained by Tolosana Moranchel et al.,[56] but with other kinetic parameter definitions.

Cassado et al.[57] working with methanol as a contaminant have considered for the intermediate (formaldehyde) reaction rate that further oxidation can be neglected and no radical termination step was taken into account. So, when the original pollutant (methanol) concentration is much higher than the formaldehyde concentration, the superficial reaction rate for intermediate appearance (eqn (45)) becomes:

$$r_{Y_i} = -\beta_1\left(1 - \sqrt{1 + \frac{\alpha_2}{a_V}\int_\lambda e_\lambda^a d\lambda}\right) \quad (61)$$

with

$$\beta_1 = \frac{k_1 k_2 [H_2O_{ads}][O_{2,ads}]}{2k_3} \quad (62)$$

In this last case the reaction rate follows zero order kinetics with respect to the contaminant concentration.

Additionally, for the experimental conditions of Cassado et al.,[57] a low irradiation rate can be assumed, then:

$$r_{Y_i} = \frac{\beta_1 \alpha_2 \int_\lambda e_\lambda^a d\lambda}{2a_V} \quad (63)$$

Therefore, first order kinetics with the LVRPA and zero order kinetics for the contaminant concentration are obtained, equivalent to eqn (69) in Table 5 but for the intermediate generation rate. The same reaction rate dependence was derived by Alfano et al.[40] when low irradiance was considered.

2.3.4.2. Hole attack. There are some kinetic studies in the liquid phase that have included a direct attack by the semiconductor holes as the main photocatalytic oxidation mechanism.[43,58–60] Some of them have worked with dichloroacetic acid that does not present stable organic intermediates during its photocatalytic oxidation. Replacing the initiation step rate (eqn (12)) and the Langmuir adsorption isotherm for liquid systems (eqn (42)) but without any competition among intermediates in eqn (32), and grouping some constant parameters, eqn (64) in Table 5 is obtained.

2.3.4.2.1. Limiting cases

● Linear adsorption equilibrium. Ballari et al.[60] have considered linear adsorption equilibrium since the employed contaminant concentration was low. A superficial reaction rate with pseudo square root dependence on the contaminant concentration was obtained (eqn (67), Table 5).

Zalazar et al.[58,59] also have considered linear adsorption for dichloroacetic acid photocatalytic oxidation and an equivalent mathematical expression of eqn (67) can be derived after some algebraic steps. However, they have posed a volumetric elemental step reaction rate and the oxygen concentration was varied during the study. Despite the same dependence on the pollutant concentration and on the LVRPA as eqn (67) was obtained, the catalyst concentration dependence (through the a_V parameter) is different and the oxygen concentration was not included in the grouping parameters since it was variable.

On the other hand, Minero and Vione,[43] proposing also the phenol photocatalytic oxidation through the hole direct attack, have derived an equivalent expression to eqn (67) for the phenol reaction rate (shown previously in eqn (9) as a simple kinetic expression). However, after making the hypothesis that the charge carrier recombination rate in the bulk is low for wide band gap semiconductors such as TiO_2, they have obtained a reaction rate expression equivalent to considering $\bar{\Phi}_\lambda = 1$ in eqn (67). So, the rate equation is based on a single kinetic parameter, α_1, for the treatment employed here since $\alpha_2 = \frac{2\bar{\Phi}_\lambda}{\alpha_1}$. A similar kinetic expression was also employed by Camera Roda et al.,[41,42] but without performing a derivation from the photocatalytic mechanism of the contaminant oxidation.

● High irradiation level. When the LVRPA gets high levels in the reacting system, then eqn (67) can be simplified to eqn (68) in Table 5. The square root dependence on the contaminant

This journal is © The Royal Society of Chemistry 2019

Chem. Soc. Rev., 2019, **48**, 637–682 | **645**

concentration and the LVRPA is obtained for the superficial reaction rate.

● Low irradiation level. When the LVRPA is low enough, eqn (67) tends to eqn (69) in Table 5. For this irradiance condition, the reaction rate is first order with respect to LVRPA and zero order with the concentration, in the same way as eqn (63).[57]

2.3.5. Photocatalytic kinetic models in gas phase systems. The general assumptions made during photocatalytic kinetic studies in the gas phase are: (i) constant oxygen concentration, (ii) variable water concentration, and (iii) adsorption competition between water and other species.

Considering that the most frequent mechanism in photocatalytic oxidation kinetics studies in the gas phase is the hydroxyl radical attack,[24] after replacing water, X and Y_i adsorption equilibrium equations (eqn (13)–(15)), and the initiation step rate as a function of the LSRPA (eqn (11)), eqn (39) can be written as eqn (70) in Table 6.

2.3.5.1. Limiting cases. ● Low contaminant and intermediate concentration. Taking into account that the main compound X and intermediates Y_i have always much lower concentration than water vapor in the gas phase,[61] the superficial reaction rate is simplified to eqn (75) in Table 6.

● High irradiation level. When the LSRPA takes high values on the photocatalytic surface, then the reaction rate in the gas phase can be approximated to eqn (76) of Table 6.

● Low irradiation level. For this irradiation condition, eqn (66) can be written as eqn (77) in Table 6.

● Linear adsorption equilibrium. Assuming linear adsorption isotherms for water and compounds X and Y_i (eqn (17)–(19)), the superficial reaction rate results as eqn (78) in Table 6. Yu et al.[62] have derived the last type of expression for the nitrogen oxide oxidation rate, but without consideration of termination reactions ($k_{10}[M] = 0$).

2.3.5.2. Other approaches. Some contributions[63,64] have considered that the hole trapping reaction occurs with OH⁻ instead of water and assumed that this species remains with a constant concentration. So, water only intervenes during the adsorption competition for the active sites with the contaminant. Therefore, an equivalent expression to the liquid phase reaction rate (eqn (44)) is obtained for the contaminant reaction rate in the gas phase, but including water in the adsorption model.

In Imoberdorf et al.[48] the reaction mechanism of tetrachloroethylene photodegradation includes a chloride radical attack as a part of the chain reaction mechanism having the prevalent oxidation rate. However, after assuming that also the contaminant

Table 6 Photocatalytic oxidation rates for gas phase reactions

Pathway	Case	Photocatalytic reaction rate	Eqn	Ref.
Hydroxyl radical attack	Complete expression	$$r_X = \dfrac{\alpha_1[X][H_2O]\left(1 - \sqrt{1 + \dfrac{\alpha_2\int_\lambda e_\lambda^{a,s}d\lambda\left(1 + K_1[X] + \sum_i K_{2i}[Y_i] + K_3[H_2O]\right)}{[H_2O]}}\right)}{\left(1 + \alpha_3[X] + \sum_i \alpha_i[Y_i] + K_3[H_2O]\right)\left(1 + K_1[X] + \sum_i K_{2i}[Y_i] + K_3[H_2O]\right)}$$	(70)	61
		$\alpha_1 = \dfrac{k_5 k_1 k_2 [O_{2,ads}] K_1 K_3 [Sites_T]^2}{2 k_3 k_{10}[M]}$	(71)	
		$\alpha_2 = \dfrac{4 k_3 \bar{\Phi}_\lambda}{k_1 k_2 [O_{2,ads}] K_3 [Sites_T]}$	(72)	
		$\alpha_3 = \dfrac{k_5 K_1 [Sites_T] + k_{10}[M] K_1}{k_{10}[M]}$	(73)	
		$\alpha_i = \dfrac{k_{8i} K_{2i} [Sites_T] + k_{10}[M] K_{2i}}{k_{10}[M]}$	(74)	
	Low concentration	$$r_X = \dfrac{\alpha_1[X][H_2O]\left(1 - \sqrt{1 + \dfrac{\alpha_2\int_\lambda e_\lambda^{a,s}d\lambda(1 + K_3[H_2O])}{[H_2O]}}\right)}{(1 + K_3[H_2O])^2}$$	(75)	48, 61 and 65
	High irradiation level	$$r_X = -\dfrac{\alpha_1[X]\sqrt{\alpha_2[H_2O]\int_\lambda e_\lambda^{a,s}d\lambda}}{(1 + K_3[H_2O])^{3/2}}$$	(76)	
	Low irradiation level	$$r_X = -\dfrac{\alpha_1[X]\alpha_2\int_\lambda e_\lambda^{a,s}d\lambda}{2(1 + K_3[H_2O])}$$	(77)	48 and 65
	Linear adsorption isotherms	$$r_X = \dfrac{\alpha_1[X][H_2O]\left(1 - \sqrt{1 + \dfrac{\alpha_2\int_\lambda e_\lambda^{a,s}d\lambda}{[H_2O]}}\right)}{\left(1 + \alpha_3'[X] + \sum_i \alpha_i'[Y_i]\right)}$$	(78)	62 with $k_{10}[M] = 0$
		$\alpha_3' = \dfrac{k_5 K_1 [Sites_T]}{k_{10}[M]}$	(79)	
		$\alpha_i' = \dfrac{k_{8i} K_{2i} [Sites_T]}{k_{10}[M]}$	(80)	

concentration is lower than the water vapor concentration, identical expression to eqn (75) was obtained. For their experimental conditions of low irradiance level, an equivalent expression to eqn (77) was finally applied to explain the results.

Another accepted hypothesis in photocatalytic systems is that the concentrations of holes and electrons are equal ($[e^-] = [h^+]$) and their recombination in semiconductors can be expected to be much faster than any other charge transfer step. So, eqn (25) can be written as:[66,67]

$$[h^+] = \sqrt{\frac{r_g}{k_3}} \qquad (81)$$

Then, and assuming $K_1[X] \ll 1$:

$$r_X = -\frac{\beta_1[X][H_2O]\sqrt{\int_\lambda e_\lambda^{a,s}d\lambda}}{(1 + \beta_2[X] + K_3[H_2O])(1 + K_3[H_2O])} \qquad (82)$$

with

$$\beta_1 = \frac{k_5 k_2 K_1 K_3 [Sites_T]^2}{k_{10}[M]}\sqrt{\frac{\bar{\Phi}_\lambda}{k_3}} \qquad (83)$$

$$\beta_2 = \frac{k_5 K_1 [Sites_T]}{k_{10}[M]} \qquad (84)$$

A similar treatment was adopted by Yu et al.[68] but without the approximation $K_1[X] \ll 1$ in eqn (82).

2.3.6. Identification of simple kinetics from mechanistically derived expressions. From the above derived reaction rate expressions based on the reaction mechanism, simple kinetics cases previously cited in Section 2.1 can be recognized. The following reaction rate functionalities with the pollutant concentration can be identified (Fig. 1a):

• A competitive Langmuir–Hinshelwood kinetics with the reaction intermediates: eqn (44), (53), (55), (57) and (78).

• A basic Langmuir–Hinshelwood kinetics: eqn (28) and (37).

• A first order kinetics: eqn (51), (54), (56), (75), (76) and (77).

• A zero order kinetics: eqn (63) and (69).

On the other hand, the following reaction rate dependences on the photon absorption rate are also frequent (Fig. 1b):

• Quadratic type model with LVRPA or LSRPA: eqn (44), (51), (57), (64), (67), (70), (75) and (78).

• First order with the LVRPA or LSRPA: eqn (55), (56), (69) and (77).

• Square root with the LVRPA or LSRPA: eqn (53), (54), (68) and (76).

3. Photon absorption rate

As explained in the previous section, the reaction rates for reactants or intermediates are required to solve the mass balances of a photocatalytic reactor. For at least one of the steps of the reaction mechanism, specifically the radiation-initiated step, it is necessary to know the photon absorption rate. The evaluation of this radiation property requires input from the light source as well as specific tools concerning the reactor medium (liquid or gas phase).
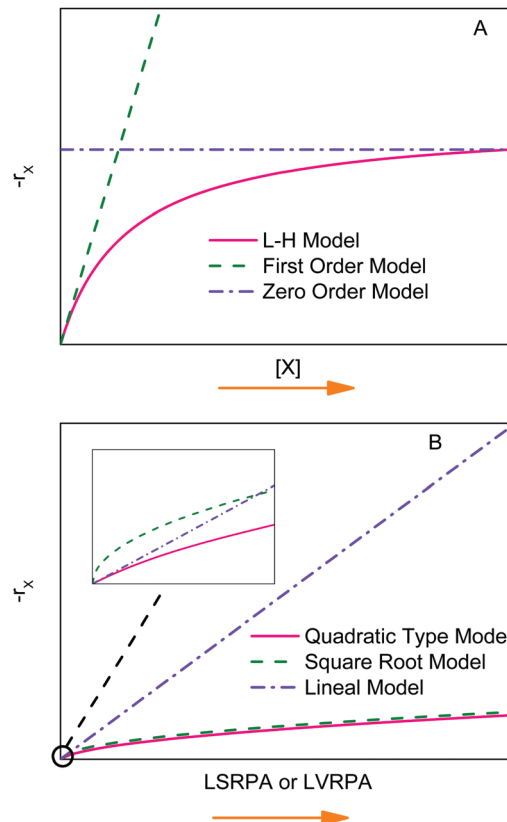

Fig. 1 Reaction rate dependence on: (A) the pollutant X concentration and (B) local superficial or volumetric rate of photon absorption.

3.1. System boundary conditions

To evaluate the photon absorption rate inside photocatalytic reactors it is first necessary to determine the radiation boundary conditions of the reacting system: (i) the radiation intensity for photocatalytic slurry reactors or (ii) the net radiation flux incident on the reactor window for photocatalytic wall and fixed bed reactors. These boundary conditions can be provided by means of emission models for tubular lamps or by experimental measurements. The mentioned emission models are (Fig. 2): the lamp model with voluminal emission and the lamp model
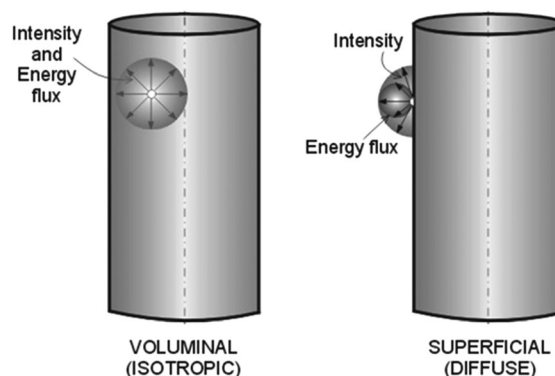

Fig. 2 Lamp models with voluminal and superficial emission. Adapted with permission from ref. 70. Copyright 1995, American Chemical Society.

This journal is © The Royal Society of Chemistry 2019

Chem. Soc. Rev., 2019, 48, 637–682 | 647

with superficial emission.[69,70] The experimental determination of the boundary conditions can be performed by chemical actinometry[58,71–73] or radiometer measurement. The use of radiometers is a simple and faster way to measure experimentally the radiation flux on the wall of laboratory photocatalytic reactors; this method can also be utilized to quickly test for any decrease in the lamp energy output over time.

3.2. Pseudo homogeneous systems (photocatalytic slurry reactor)

Photocatalytic reactions carried out in a slurry reactor require the evaluation of the Local Volumetric Rate of Photon Absorption (LVRPA). The Radiative Transfer Equation (RTE) and its optical parameters, the radiation absorption and scattering coefficients and the phase function are required to compute the LVRPA.[74]

3.2.1. Radiative transfer equation (RTE). Firstly, the spectral radiation intensity[75] or the spectral radiance[76] should be defined. This fundamental variable can be defined as the amount of radiative energy per unit wavelength interval, per unit solid angle, per unit normal area, and per unit time (Fig. 3). Thus,

$$I_\lambda(\mathbf{x}, \Omega, t) = \frac{\mathrm{d}E_\lambda}{\mathrm{d}A \cos\theta \mathrm{d}\Omega \mathrm{d}\lambda \mathrm{d}t} \qquad (85)$$

It is worth noting that for a given wavelength (λ), the radiation intensity is a function of the spatial position ($\boldsymbol{x}$), direction ($\boldsymbol{\Omega}$) and time (t). In photochemical reactors the typical units of I_λ are Einstein per second, per steradian, per square meter and per nm.

Posing a photon balance in an elemental volume V in space having an absorbing, emitting, and scattering medium, and using the concept of spectral radiation intensity, the final expression of the RTE is obtained:[70]

$$\frac{\mathrm{d}I_\lambda(s, \Omega, t)}{\mathrm{d}s} = [\kappa_\lambda(s, t) + \sigma_\lambda(s, t)]I_\lambda(s, \Omega, t)$$
$$+ \frac{\sigma_\lambda(s, t)}{4\pi} \int_{4\pi} p_\lambda(\Omega' \to \Omega)I_\lambda(s, \Omega', t)\mathrm{d}\Omega' \qquad (86)$$
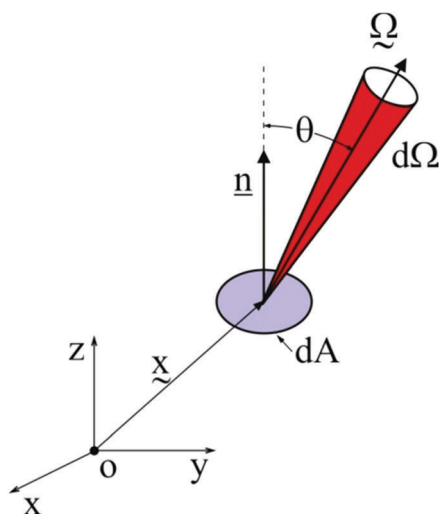
where s is a directional coordinate along the ray path, κ_λ the spectral volumetric absorption coefficient, σ_λ the spectral volumetric scattering coefficient, and $p_\lambda(\Omega' \to \Omega)$ the phase function.

Here κ_λ represents the fraction of the incident radiation that is absorbed by the matter per unit length along the path of the beam and σ_λ the fraction of the incident radiation that is scattered by the matter in all directions per unit length along the path of the beam (Fig. 4). Both κ_λ and σ_λ coefficients have units of length^{-1}. On the other hand p_λ is a normalized phase function, which gives information concerning the directional distribution of the scattered radiation.

3.2.2. Evaluation of the optical properties. In this section, an experimental method to evaluate the optical properties (κ_λ, σ_λ and p_λ) of aqueous TiO$_2$ suspensions is described. This method is based on the following measurements of TiO$_2$ suspensions in a spectrophotometer sample cell: (i) absorbance under specially constructed conditions to minimize the collection of the scattered rays by the spectrophotometer detector, (ii) diffuse transmittance, and (iii) diffuse reflectance.

Firstly, the extinction coefficient $\beta_\lambda = \kappa_\lambda + \sigma_\lambda$ is measured. This coefficient can be obtained from spectrophotometric absorbance readings of a catalyst suspension using the expression:

$$\beta_\lambda = \frac{2.303A_\lambda}{L} \qquad (87)$$

where A_λ is the absorbance of the TiO$_2$ suspension and L the cell path length. The specific extinction coefficient β_λ^*, defined as the extinction coefficient per unit catalyst mass concentration, is then calculated from the slope of a linear regression of the plot: extinction coefficient *versus* the catalyst mass concentration.
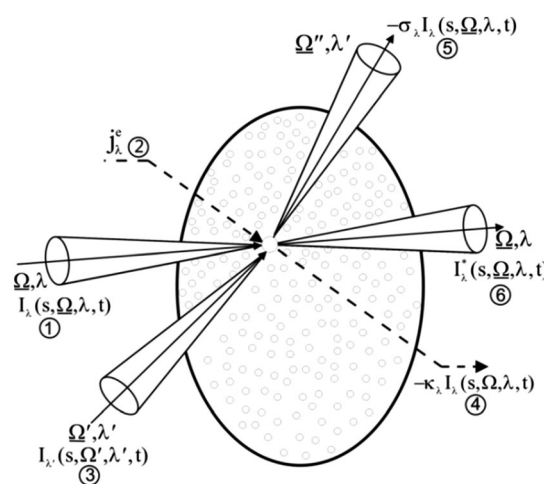

Fig. 4 Representation of intervening phenomena in radiation transport. (1) Incident intensity along s with direction $\underline{\Omega}$ and wavelength λ, (2) emission of radiation in the direction $\underline{\Omega}$ and wavelength λ, (3) intensity in a representative, arbitrary direction $\underline{\Omega}'$ and wavelength λ' to be scattered in the direction $\underline{\Omega}$ and wavelength λ, (4) absorbed intensity, (5) scattered intensity in a representative, arbitrary direction $\underline{\Omega}''$ and wavelength λ' out of the direction $\underline{\Omega}$ and wavelength λ, and (6) emerging intensity along s in the direction $\underline{\Omega}$ and wavelength λ. Adapted with permission from ref. 70. Copyright 1995, American Chemical Society.

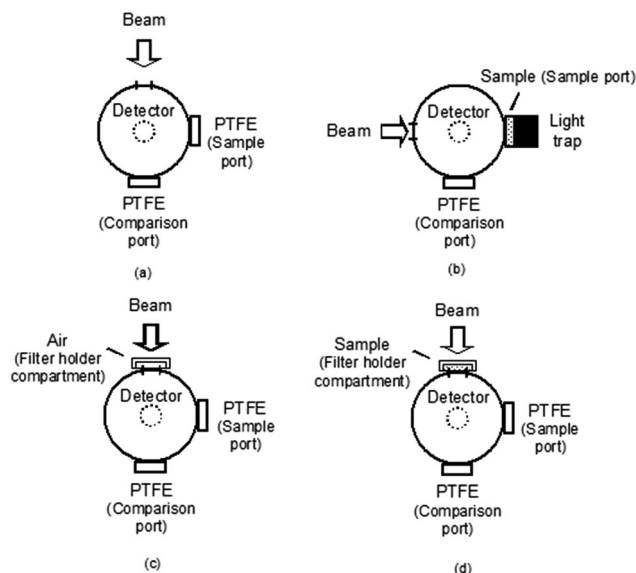**Fig. 3** Spectral radiation intensity.

Fig. 5 (a and b) Integrating sphere configuration for reflectance measurements. (c and d) Integrating sphere configuration for transmittance measurements. Reprinted with permission from ref. 77. Copyright 2005, American Chemical Society.

Secondly, measurements of the spectral diffuse reflectance (R_λ) and transmittance (T_λ) of a catalyst suspension are performed in a spectroradiometer equipped with an integrating sphere attachment. Fig. 5(a and b) shows the configuration used to carry out the reflectance measurements and Fig. 5(c and d) displays the configuration to perform the transmittance measurements.

After these experimental measurements, the RTE should be posed and numerically solved in the spectrophotometer cell and a nonlinear optimization program is applied to adjust RTE predictions to experimental data. More details on the spectrophotometric measurements of diffuse reflectance and diffuse transmittance and the evaluation of the optical properties of aqueous catalyst suspensions can be found elsewhere.[77]

3.2.3. Local volumetric rate of photon absorption. The spectral LVRPA (e_λ^a) in an elementary volume of a photocatalytic slurry reactor can be defined by means of the spectral radiation intensity I_λ defined in eqn (85). Therefore, e_λ^a can be calculated from the expression:

$$e_\lambda^a(\mathbf{x}, t) = \int_{\varphi_1}^{\varphi_2} \int_{\theta_1}^{\theta_2} \kappa_\lambda(\mathbf{x}, t) I_\lambda(\mathbf{x}, \theta, \varphi, t) \sin\theta \, \mathrm{d}\theta \, \mathrm{d}\varphi \qquad (88)$$

where θ and φ are the spherical coordinates which define the solid angle Ω. Besides, when a polychromatic radiation source is employed, an integral over the entire useful wavelength interval (from $\lambda_{\min} = \lambda_1$ to $\lambda_{\max} = \lambda_2$) is performed. Thus, the total (or polychromatic) LVRPA is calculated by:

$$e^a(\mathbf{x}, t) = \int_{\lambda_1}^{\lambda_2} \int_{\varphi_1}^{\varphi_2} \int_{\theta_1}^{\theta_2} \kappa_\lambda(\mathbf{x}, t) I_\lambda(\mathbf{x}, \theta, \varphi, t) \sin\theta \, \mathrm{d}\theta \, \mathrm{d}\varphi \, \mathrm{d}\lambda \qquad (89)$$

3.2.4. Solution methods of the RTE. A revision on rigorous and approximate methods for solving the RTE in heterogeneous media has been presented in ref. 75 and 78 among others.

Different simplified approaches for the numerical simulation of the RTE have been presented: the Two Flux Methods (Eddington and Schuster–Schwarzschild Approximations), the Exponential Kernel Approximation and the Spherical Harmonics Method. Other approximate methods, suitable for design and scale-up of photocatalytic reactors, are represented by the Two-Flux Models for the cases of zero reflectance and reflectance greater than zero,[79,80] the Six Flux Model[81–83] and the Probabilistic Approach for dense particulate systems.[84]

Although detailing the rigorous numerical methods to solve the RTE is out of the scope of this review, it can be mentioned that most used numerical techniques in photocatalytic systems are the Discrete Ordinate Method (DOM), the Finite Volume Method (FVM) and the Monte Carlo (MC) simulation.

The DOM is a very powerful approach that can provide accurate results of the heterogeneous radiation field. It has been applied in one- and multi-dimensional rectangular and cylindrical geometries and in systems with different degrees of anisotropy.[78] This method transforms the RTE into a system of algebraic equations that can be solved by machine computation.

The FVM has some similarities with respect to DOM. In the FVM the RTE is integrated over both the volume control and the angle control.[85,86] Some applications of the FVM for estimating the radiation field in photocatalytic slurry reactors have been presented by ref. 87 and 88 among others. Briefly, the numerical procedure of the FVM is as follows: the computational domain is divided into a number of control volumes, the solid angle is discretized into a number of finite solid angles, and the RTE is integrated over all control volumes and angles. Finally, the boundary conditions of the system provide the linear algebraic equations to solve the problem by an iterative method.[88]

The MC method is a statistical approach that can be applied to calculate the absorbed radiation by the catalyst existing inside suspended[89,90] or fluidized reactors.[91] This technique comprises the tracking of a large number of photons to determine the trajectories and fates of the photons emitted by the lamp and/or entering through the reactor window. To do this, randomly generated numbers (R_i) in the range 0 to 1 should be generated by a special subroutine. Then, the following steps are considered: direction of photon entering the reactor window, length of the photon flight, and fate (absorption or scattering) of the photon.[52] If the photon is absorbed, it is stored in the corresponding spatial cell of the reactor and the trajectory ends. If not (due to radiation scattering), the previous sequence of steps is repeated until the photon is either absorbed or escaped from the reactor.

Fig. 6 shows computational results of LVRPA as a function of spatial coordinates for various catalyst mass concentrations, in different configurations of photocatalytic slurry reactors.

3.3. Immobilized systems (wall and fixed bed reactors)

For the case of wall and fixed bed photocatalytic reactors, in which the catalyst is immobilized on an inert support, a different approach should be used. Firstly, the optical

This journal is © The Royal Society of Chemistry 2019
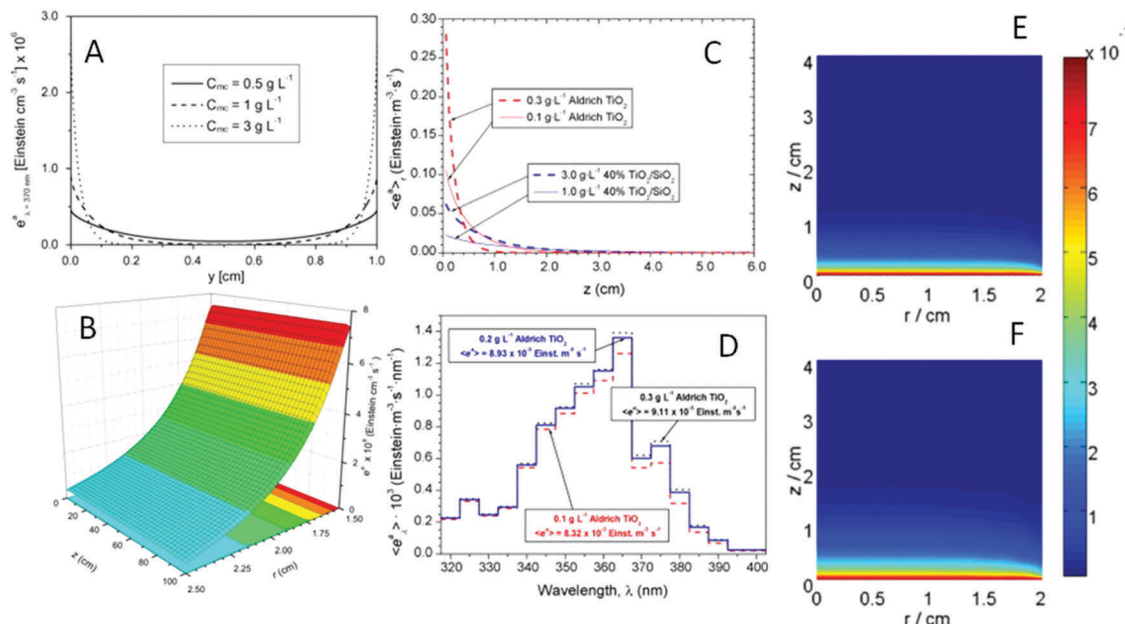
Chem. Soc. Rev., 2019, 48, 637–682 | 649

Fig. 6 Local volumetric rate of photon absorption profiles. (A) LVRPA distribution in the reactor space as a function of the reactor thickness. Reprinted from ref. 92. Copyright 2008, with permission from Elsevier. (B) LVRPA as a function of the spatial coordinates with a catalyst mass concentration of 0.1 g L^{-1}. Reprinted from ref. 93. Copyright 2013, with permission from Elsevier. (C) r-Averaged LVRPA axial profiles and dependence of the average LVRPA on the titanium dioxide concentration. Reprinted from ref. 94. Copyright 2007, with permission from Elsevier. (D) Spectral distribution of the LVRPA for different concentrations of Aldrich TiO_2. Reprinted from ref. 94. Copyright 2007, with permission from Elsevier. 2D (bidimensional) maps of LVRPA under UV (E) and visible (F) illumination conditions for anatase TiO_2 powders. Adapted with permission from ref. 95. Copyright 2017, Elsevier.

properties of the catalyst–support system should be measured and then the Local Surface Rate of Photon Absorption (LSRPA) evaluated.

3.3.1. Optical properties. To calculate the photon absorption of the catalytic film, four optical parameters of the catalyst–support system are required: (i) the diffuse transmittance of the coated (film + support) plate (T_{fg}), (ii) the diffuse reflectance of the coated (film + support) plate (R_{fg}), (iii) the diffuse transmittance of the bare support plate (T_g), and (iv) the diffuse reflectance of the bare support plate (R_g). As was shown in Fig. 5, values of diffuse R and T can be obtained from experimental measurements as a function of wavelength in a spectroradiometer equipped with an integrating sphere reflectance attachment.[77,96]

According to the net-radiation or the ray-tracing method,[85] the mathematical expressions to represent the fraction of incident energy reflected (R_f), transmitted (T_f) and absorbed (A_f) by the catalytic film are as follows:

$$R_f = \frac{R_{fg} T_g^2 - T_{fg}^2 R_g}{T_g^2 - R_g^2 T_{fg}^2} \quad (90)$$

$$T_f = \frac{T_{fg}}{T_g}\left(1 - R_f R_g\right) \quad (91)$$

$$A_f = 1 - T_f - R_f \quad (92)$$

3.3.2. Local surface rate of photon absorption (LSRPA). The spectral net radiation flux q_λ is defined by the dot product

between the unit direction vector $\boldsymbol{n}$ and the spectral radiation flux vector $q_\lambda(\mathbf{x},t)$:[75]

$$q_\lambda(\mathbf{x}, t) = \boldsymbol{n} \cdot q_\lambda(\mathbf{x}, t) = \int_\Omega I_\lambda(\mathbf{x}, \Omega, t)\Omega \cdot \boldsymbol{n}\, d\Omega \quad (93)$$

The radiation variable q_λ represents the net flux of monochromatic radiative energy through a surface normal to a given direction per unit time, unit area and unit wavelength, due to radiation from all directions of space.

Afterwards, the LSRPA can be determined from a local radiative energy balance utilizing the spectral net radiation flux defined above:[97,98]

$$e_\lambda^{a,s}(\mathbf{x},t) = q_{\lambda,\text{in}}(\mathbf{x},t) - q_{\lambda,\text{tr}}(\mathbf{x},t) - q_{\lambda,\text{rf}}(\mathbf{x},t) \quad (94)$$

Here $q_{\lambda,\text{in}}(\mathbf{x},t)$ is the spectral radiative flux incident on the catalytic film, $q_{\lambda,\text{tr}}(\mathbf{x},t)$ the spectral radiative flux transmitted through the catalytic film, and $q_{\lambda,\text{rf}}(\mathbf{x},t)$ the spectral radiative flux reflected by the catalytic film.
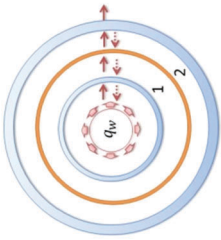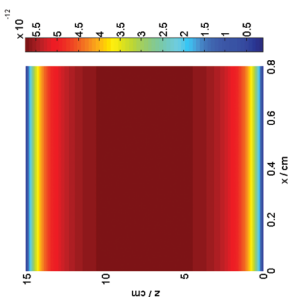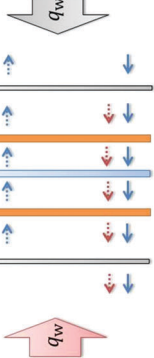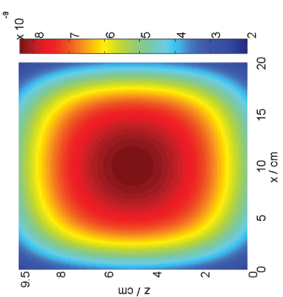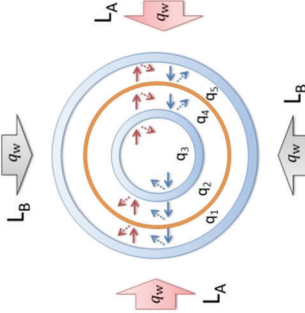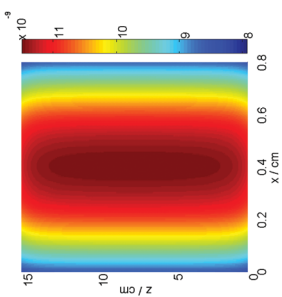
3.3.3. Radiation flux balance (wall reactor). Defining q_n^+ and q_n^- as the forward and the backward radiation fluxes with regard to the nth layer of any reactor, we can write:[61,85,99,100]

$$q_n^+ = R_n q_n^- + T_n q_{n-1}^+ \quad (95)$$

$$q_{n-1}^- = T_n q_n^- + R_n q_{n-1}^+ \quad (96)$$

where T_n and R_n are the diffuse transmittance and reflectance of the nth layer, respectively. Layer in this case considers the glass walls or the catalyst as described in Table 7 and concerning

650 | *Chem. Soc. Rev.*, 2019, **48**, 637–682

This journal is © The Royal Society of Chemistry 2019

Table 7 Schematic representation of reactor geometries and equations for local net radiation flux on the catalytic film. Profile of LVRPA using the transmittance and reflectance model.[a] Adapted from ref. 99. Copyright 2015, with permission from Elsevier

Reactor scheme	Transmittance model		Transmittance and reflectance model		LSRPA (Einstein cm^{-2} s^{-1})
	$q_{in}^{T} = q_w T_g$	(97)	$q_{in}^{TR} = q_w(T_g + T_g T_f R_g)$	(100)	
	$q_{in}^{T} = q_w(T_g + T_g^2 T_f)$	(98)	$q_{in}^{TR} = q_w T_a \times \left(1 + \dfrac{R_g T_f - R_g^2 R_f T_f + T_g T_f + T_g^2 R_f T_f}{1 - 2R_g R_f + R_g^2 R_f^2 - T_g^2 R_f^2}\right)$	(101)	
	$q_{in}^{T} = q_w(T_g + T_g^3 T_f)$	(99)	$q_{in}^{TR} = \sqrt{{}^x q^2 + {}^y q^2}$ $\quad$ (102)		
			${}^x q = {}^x_{L_A} q_1^{\uparrow} + {}^x_{L_B} q_1^{\uparrow} + {}^x_{L_A} q_2^{\downarrow} + {}^x_{L_B} q_2^{\downarrow}$ $\quad$ (103)		
			${}^y q = {}^y_{L_A} q_1^{+} + {}^y_{L_B} q_1^{+} + {}^y_{L_A} q_2^{-} + {}^y_{L_B} q_2^{-}$ $\quad$ (104)		
			${}^x_{L_A} q_1^{\uparrow}, {}^x_{L_B} q_1^{\uparrow}, {}^x_{L_A} q_2^{\downarrow}, {}^x_{L_B} q_2^{\downarrow}, {}^x_{L_A} q_1^{+}, \ldots$		
			${}^y_{L_B} q_1^{+}, {}^y_{L_A} q_2^{-}, {}^y_{L_B} q_2^{-} = f(q_w, T_f, T_g, R_f, R_g)^b$		

[a] From top to bottom: annular, plate and annular multilamp reactors. In the figures glass shells (g subindex) are presented in blue and the sample-catalyst film (f subindex) in orange. Arrows indicate the fraction of light transmitted and reflected at each interface. Full formula and more details are in the supporting information of ref. 99.

This journal is © The Royal Society of Chemistry 2019

Chem. Soc. Rev., 2019, **48**, 637–682 | 651

each element in the light path. This table also provides the equations to obtain the radiation flux at the catalyst surface considering models using transmission and transmission and reflection effects for each scheme using the transmittance and reflectance model (eqn (97)–(104)).[67,99]

Finally, the LSRPA can be computed by integration over all useful wavelengths (see figures of the last column of Table 7):

$$e^{a,s}(\mathbf{x}) = \sum_\lambda q_{\lambda,in}^{T,TR}(\mathbf{x})A_{\lambda,f} = q_{in}^{T,TR}(\mathbf{x})\sum_\lambda F_\lambda A_{\lambda,f} \qquad (105)$$

where F_λ is the normalized spectral distribution of the radiation emitted by the lamp.

3.3.4. Radiation flux by Monte Carlo simulation (fixed bed).
The MC method is a statistical approach that can also be applied to compute the absorbed radiation by the photocatalyst in fixed bed[101] or catalytic wall[102] reactors. For these systems, a thin layer of the sample is deposited on the surface of an inert support and, normally, it is more appropriate to calculate the photon absorption rate per unit area of the irradiated catalyst-coated surface (LSRPA).

For example, the Monte Carlo simulation was applied to evaluate the LSRPA in a fixed-bed photocatalytic reactor to study the water disinfection of *Escherichia coli*.[103] The experimental work was carried out in an annular, fixed-bed reactor filled with Raschig rings coated with a thin film of TiO_2 and operated in a recirculation batch mode. Firstly, random numbers between 0 and 1 are generated by a special subroutine and then it was assumed that photons follow a linear trajectory inside the reactor until they reach a TiO_2-coated ring or the reactor walls. Photons that reach the coated rings can be reflected, absorbed or transmitted by the TiO_2 film. The transmission of the TiO_2 film is calculated from the volumetric absorption coefficient (κ_λ) of the photocatalyst determined in a previous section and the average thickness of the film. The absorbed photons are stored in the corresponding cell of the annular space and then the trajectories and fates of a new photon bundle are considered. At the end of the simulation procedure, the LSRPA in each cell of the annular reactor can be computed from

$$e^{a,s}(x,z) = \sum_\lambda \frac{n_{ph\lambda,abs}(x,z)}{n_{ph\lambda,T}} \frac{F_\lambda P_L}{2\pi r \Delta x \Delta z} \frac{V_R}{A_{cat}} \qquad (106)$$

where $n_{ph\lambda,abs}(x,z)$ is the number of λ-photons absorbed in the spatial cell (x,z), $n_{ph\lambda,T}$ the total number of λ-photons generated in the simulation, P_L the emission power of the lamp, r the distance between the spatial cell and the center of the reactor, A_{cat} the catalytic area of the reactor, and Δx and Δz are the cell dimensions.

Fig. 7 shows a 3-D plot of computed results of the LSRPA as a function of the reactor radius and length, for the case when rings have two TiO_2 coatings.

4. Spectroscopy: *in situ* analysis of photo-active species

Within the landscape presented in the introduction section, here we describe the main aspects resulting from spectroscopic
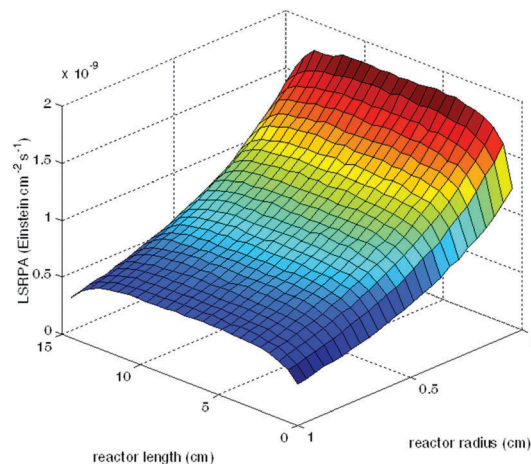

Fig. 7 LSRPA in an annular, fixed-bed photocatalytic reactor. Reprinted from ref. 103. Copyright 2015, with permission from Elsevier.

studies carried out in the photocatalysis field and specifically those related to modern, *in situ* mechanistic and kinetic studies reported in the literature.[104] We will address this objective first with the analysis of works concerning the generation and capture of initial electron and hole charge carrier species created after light absorption and second, considering the chemical species originating from the attack of such charge carriers on target, mostly pollutant, molecules and that are involved in relevant kinetic steps of photocatalytic processes.

4.1. Electron and hole radical species: generation and capture

As described in Table 2 ("activation" step), electron–hole pairs are generated after light absorption in semiconductor materials. They can be captured by several defects (including surface atoms) associated with localized electronic states and/or can be mobile at the corresponding electronic bands within the particle size or across particle interfaces of the semiconductor. Those charge species reaching the surface would be able to generate chemistry but to do it they must compete with the charge combination step(s), also included in Table 2 ("recombination" step).[1,105]

Here we will not describe the physico-chemical properties and behavior of all these charge generation, capture and recombination processes but just extract their most relevant features of significance for photo-catalytic kinetic and mechanistic studies. As detailed in Section 2 of this contribution, mostly three steps determine the kinetics of photocatalytic processes. These are: (i) direct attack of the semiconductor hole formed during the irradiation step, (ii) oxidation by hydroxyl radicals formed during the hole trapping by water or hydroxyl surface ions (step "hole trap" of Table 2), and (iii) reaction with the superoxide radical formed during the electron trapping by oxygen (step "electron capture" of Table 2).

We may also consider four additional steps: (iv) excitation of oxygen forming a singlet state ($O_2 + \text{energy}^- \rightarrow {}^1O_2$); (v) formation of hydrogen peroxide ($O_2 + 2e^- + 2H^+ \rightarrow H_2O_2$). These two processes are in principle considered of importance in a limited number of photo-catalytic systems, mostly concerning

652 | *Chem. Soc. Rev.*, 2019, **48**, 637–682

This journal is © The Royal Society of Chemistry 2019

the degradation of a few dyes or visible light actived molecules which can exchange energy with the oxygen molecule (leading to the singlet state), as well as the inactivation of microorganisms as the two chemical species (singlet oxygen and hydrogen peroxide) are generated at low frequency as metabolites during respiration. Their role under UV illumination is thus limited in the vast majority of the reactions analyzed but they can be of significance in visible light triggered chemical reactions.[1,105,106] The last couple of steps concerns (vi) the multiple captures of electrons by the oxygen molecule leading to the peroxide radical ($O_2 + 2e^- \rightarrow O_2^{\bullet 2-}$) and (vii) the formation of the O_3^- radical by reaction of holes captured at lattice oxygen and molecular oxygen. As detailed below, these two reaction steps are considered of relatively minor significance in subsequent chemical steps as they require the interaction of several charge carrier species with molecular oxygen and/or generate relatively unstable species with respect to other oxygen-related charged species.[1,105]

The direct attack by holes takes into account mobile hole species within the valence band. As previously demonstrated using static and dynamic (transient) photoluminescence and infrared studies (thus preferentially scanning UV, visible and near IR regions), free holes are in thermal equilibrium with those in shallow traps. This fact has consequences on the lifetime of the species which experimentally goes from a fraction of a picosecond to a few nanoseconds in the most typical oxide photocatalysts such as titania and zinc oxide polymorphs.[1,105] So, considering that turnover frequencies at catalysis are always above a single cycle time per a few microseconds, the bare hole creation does not dominate the kinetics of the catalysis although they can be a relevant species from both mechanistic and kinetic points of view when the so-called direct hole mechanism takes place. A typical example corresponds to some reactions where alcohols or amines are considered, as they have a rather facile hole capture step and are considered to be triggered by free hole species.[1,21,105]

Trapping of holes (at so-called deep traps, with lifetime above a nanosecond) may play a role in the formation of hydroxyl radicals as explained below. Irrespective of the formation mechanism of hydroxyl radicals (there is an intense discussion concerning the exact mechanism and corresponding thermodynamic/kinetic issues), they are detected after light excitation and their relevant kinetic role in many photocatalytic processes is fully demonstrated (as we will discuss in Section 5).[1,105] Many investigations use EPR (Electron Paramagnetic Resonance) to study trapping of holes. EPR spectroscopy is extremely sensitive, and the minimum detectable concentration can be of 10^{11} spins g^{-1}, 10^{13} spins mL^{-1}, or 10^{-8} mol L^{-1} under favorable conditions.[107] Focussing at titania, many investigations analyzed hole-related species. The EPR signals obtained in titania are schematically summarized in Fig. 8.[108]

Concerning holes, in a seminal work, Howe and Gratzel[109] observed a signal with an asymmetric g-factor: $g_1 = 2.002$, $g_2 = 2.012$, and $g_3 = 2.016$, assigned to a hole in a $Ti^{4+}O^{\bullet-}Ti^{4+}OH^-$ structure. The work concluded that the signal was related to
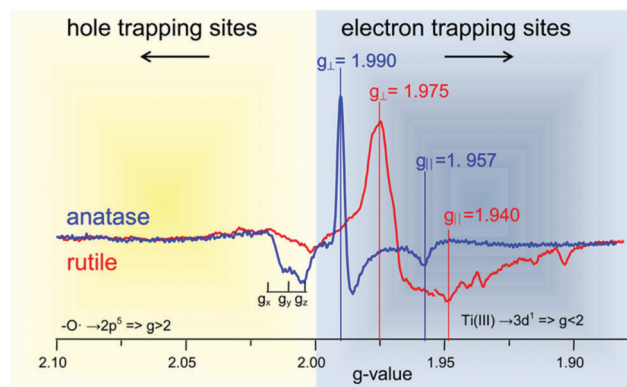

Fig. 8 EPR spectra of anatase and rutile nanoparticles recorded under illumination at 4.5 K. Electrons are trapped at lattice sites as Ti^{3+} (showing axially symmetric signal), while holes are trapped at the surface of nanoparticles as oxygen-centered radicals (showing the asymmetric signal). Due to the different symmetry of titanium cation in anatase (D_{2d}) and rutile (D_{2h}), the EPR spectra of these nanoparticles can be clearly differentiated. Reproduced with permission from ref. 108. Copyright 2014, American Chemical Society.

sub-surface oxygen radicals linked to surface hydroxyls. Subsequently, other types of species, such as surface oxygen radicals ($Ti-O-Ti-O^\bullet$)[110–112] and lattice $O^{\bullet-}$ radicals were postulated.[113,114] Detailed studies to identify the photogenerated surface centers were carried out with TiO_2 catalysts prepared using isotopically exchanged water, D_2O, and/or ^{17}O enriched water $H_2^{17}O$.[110,111] Such studies allowed a more definitive assignment of the trapped holes in anatase and rutile materials. The oxygen isotope experiments proved that the trapped holes should be assigned to an oxygen surface anion radical covalently bound to titanium atoms in the form of $Ti^{4+}O^{2-}Ti^{4+}O^{\bullet-}$. The EPR signal intensity for the trapped holes was very sensitive to the total surface area and hydration. The signal obtained for trapped holes at 6–240 K was not the same as that of surface bound or free $HO^\bullet$ radicals due to the fact that there was no change in the EPR line width observed if D_2O, instead of H_2O, was used for preparation of colloids. In a recent EPR study by Berger et al.,[114] trapped holes in dehydrated TiO_2 nanocrystals were detected as a lattice $O^{\bullet-}$ radical ($g_\perp = 2.0121$, $g_\parallel = 2.0046$) generated from lattice O^{2-} in the valence band. This low field signal cannot be observed if a large amount of O_2 was present due to the exchange effect between the gas phase molecular oxygen and the $O^{\bullet-}$ radical. The situation is even more complex when titania samples are doped with anion or cation atoms but the specific role of the doping ions in creating hole (and electron) capturing centres has been summarized in a few reviews.[107,115]

In any case, the above summarized controversy on trapped hole assignment(s) mainly results from the fact that holes are localized in the TiO_2 surface (or near surface) region, which are greatly susceptible to surface treatment and modification.[107,116] Therefore, the structural interpretation of the observed EPR signals of photo-produced holes is under intense debate. Nevertheless, (i) the broadly defined species described as lattice $O^{\bullet-}$ and the strong effect of surface characteristics and particularly hydration on the behavior of such species; (ii) the rather limited

This journal is © The Royal Society of Chemistry 2019

Chem. Soc. Rev., 2019, 48, 637–682 | 653

intensity of hole-related species with respect to electron related species detected in anatase and (its almost absence in) rutile strongly suggest the reaction of the majority of trapped holes with surface (OH or water related) species to form EPR silent radicals.[117] Possibly, the hole species visible by EPR are those with lower rates of transformation and may thus have a chance to react directly with the target molecules of the photo-chemical reactions as previously mentioned for mobile holes. In any case, the general landscape to interpret the significance of hole capture in photo-chemistry can be deduced from the studies carried out using photoluminescence techniques.[118,119] Although the significance of radiative *vs.* non-radiative de-excitation pathways depends on primary particle size (full description is presented in ref. 1), for sizes *ca.* 10 nm the importance of radiative pathway grows and appears to be dominated by two channels considering annihilation of spatially separated deep trapped holes and electrons with the corresponding free charge carriers. Thus, being deep trapped holes present at the surface or near surface sites, their chances to be involved in chemistry are significant under a reactive environment.

HO[•] type radicals, which would thus be the major hole-related species, are frequently detected with EPR or Total Internal Reflection Fluorescence Microscopy (TIRFM) with the help of probe molecules. The use of photoluminescence and probe molecules (7-hydroxy coumarin) is also reported although less frequently used in the context of spectro-kinetic studies.[120] The TIRFM technique provides illuminating information and in a review article Tachikawa and Majima[20] showed that the production of such radical-type species occurs with a spatially inhomogenous distribution as a direct consequence of the similar distribution of active catalytic sites and that they are affected by the same surface properties (surface area, primary particle size, particle–particle contact, defects, water presence, *etc.*) affecting hole behavior (Fig. 9).
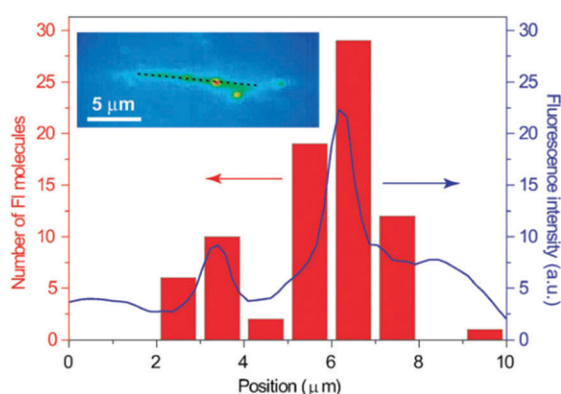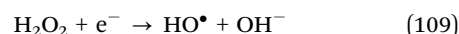

Fig. 9 Histogram of the number of fluorescein molecules generated at a position, which is determined from the peak of the Gaussian distribution (red), and line profile of the integrated fluorescence intensity along the long axis of the particle shown by the dotted line in the inset (blue). The fluorescence intensity should be directly correlated with the photocatalytically active sites. The inset shows the integrated fluorescence intensity of the TiO_2 nanotube over 120 s during the photocatalytic reaction. Reproduced with permission from ref. 20. Copyright 2010, Royal Society of Chemistry.

The existence of these radicals at the gas or liquid–oxide surface area rather than exclusively at the oxide surface is also pointed out by the technique. This indicates that the vibrational analysis of hydroxyl entities would need to consider two points: (i) the ones excited by light would present a Stark effect; and (ii) only the ones strictly at the surface of the solid can be measured by vibrational techniques.

EPR also showed that OH[•] type radicals are mostly related to the gas or liquid–solid interface. The technique uses commonly nitrone and nitroso spin traps, DMPO (5,5-dimethyl-1-pyrroline *N*-oxide) being the most frequently used. Low concentration of the probe is required to make negligible light absorption (by the probe itself). Quantification of the signal as a function of time is customarily utilized to measure the initial slope of the HO[•] type radical production as a function of time to limit effects of multiple additions to the EPR active adduct (DMPO–HO[•]) and subsequent formation of EPR silent species. The adduct renders a $1:2:2:1$ intensity pattern with a signal centered at *ca.* $g = 2.005 \pm 0.001$.[107,115,121] The signal is however discussed as to the point of whether it measures exclusively hydroxyl radicals or also surface trapped holes, as both species are likely in equilibrium or are closely connected in reactive atmospheres having water.[27,122,123]

Hole capture and behavior at the surface to form hydroxyl type radicals have also been studied in other photocatalytic semiconductors such as ZnO or g-C_3N_4. Oxygen defects play a key role in the case of the zinc oxide producing deep trapped electronic states capturing holes. The main difference with titania is the surface to bulk distribution of such hole traps and their effects in photoactivity.[119] The case of the carbon nitride material differs however significantly from the bare ZnO and TiO_2 oxide photocatalysts already discussed. The band structure of the carbon nitride material does not allow the direct production of holes.[123,124] However, studies by EPR showed the presence of OH[•] type radicals which may initially be formed from electron related radicals *via* the following steps:[125,126]

$$O_2 + e^- \rightarrow O_2^{•-} \tag{107}$$

$$O_2^{•-} + e^- + 2H^+ \rightarrow H_2O_2 \tag{108}$$

$$H_2O_2 + e^- \rightarrow HO^• + OH^- \tag{109}$$

A fine analysis supporting such a pathway for the formation of the OH[•] type radical using different radical scavengers has been presented recently.[127] A similar case in the absence of hydroxyl radical formation is mentioned in review articles for anion-doped (N, S, C, B) titania samples;[1,107] however, a single report showed the production of hydroxyl radicals in the presence of interstitial boron.[107]

Similarly to holes, electrons generated after light excitation can suffer capture by shallow or deep traps and/or be transported to the surface to generate chemistry. All such processes compete with the recombination. We can extend the parallelism to the existence of the so-called free electrons and deep trap ones. Free electrons (in thermal equilibrium with shallow trap ones) usually present larger average lifetimes (by a factor of 2 to 5) than their hole counterpart.[1,21,105,108] Trapped electrons

are detected in titania samples using EPR, providing signals summarized in Fig. 8 for anatase and rutile polymorphs. In titania, electron trapping centers are formally described as Ti(III) centers. After the seminal work of Howe and Gratzel,[128] a significant number of papers were devoted to this issue and are summarized in ref. 115, 117 and 129. In both anatase and rutile phases, surface sites with a disordered environment are observed with g averaging around 1.91–1.93 but showing significant dispersity among the different studies. This is at least justified in terms of the degree of hydration of the sample subjected to study. Bulk Ti species are observed with $g_\perp$ = 1.99 ± 0.002, $g_\parallel$ = 1.962 ± 0.004 in anatase and $g_\perp$ = 1.97 ± 0.002, $g_\parallel$ = 1.946 ± 0.004 in rutile, although better resolved, orthorhombic signals for rutile (1.966/1.961/1.948)[130] are also frequently reported. Interstitial Ti species were also observed in both phases with signals around 1.988/1.958 for anatase and 1.978/1.975/1.942 for rutile. Interstitial sites are always in the bulk of the materials and are considered the deepest traps (the first populated in the EPR experiments). The lifetime of the deep trapped electrons indicates that the de-excitation pathway concerning trapped electrons[118,119] takes into account multi-trapped species with Ti(III) nature. Due to their surface/bulk and energetic/lifetime characteristics, interstitial Ti seems thus an essential recombination center while the other two Ti(III) traps could be involved in chemistry. Of course, those at the surface would have the maximum likelihood to generate chemistry. This issue has been exploited to a maximum in the case of the so-called black titania, although the complex influence of all defects present in such solid(s) is still under debate.[131,132] The procedure of controlling surface vacancies to enhance photo-activity has been extended on the other hand to other oxides such as ZnO or In_2O_3.[133]

In the case of composite anatase–rutile samples, EPR studies of P25 showed electron transfer from rutile to anatase as well as Ti centers with local tetrahedral-like symmetry sited at the interface between particles of the two polymorphs.[134,135] In other anatase–brookite composites, hole instead of electron transfer from anatase to brookite is postulated.[136]

In the presence of oxygen, as occurs in the vast majority of photo-catalytic reactions, electrons react with molecular oxygen. Oxygen usually follows a sequential transformation at illuminated oxide surfaces forming superoxide ($O_2 + e^- \rightarrow O_2^{\bullet-}$) and peroxide ($O_2^{\bullet-} + e^- \rightarrow O_2^{\bullet 2-}$) entities, and both species can be dissociated and exchanged with lattice oxygen.[137–139] The initial interaction of oxygen with titania is relatively difficult to be analyzed although a vibrational band near $ca.$ 1000 or 800 cm^{-1} (depending on whether they are measured in the liquid or gas phase and the effect of water) could be observed.[140,141] As mentioned previously, the superoxide species is supposed to be the most significant oxygen related radical species in photo-catalytic reactions. Although peroxide species would be thermodynamically favored on titania surfaces, an important kinetic barrier limits the transformation at room temperature and indicates the relative weakness of oxygen as an electron scavenger.[142] Importantly, from the single-molecule kinetic analysis of a TIRFM signal, it was found that the quenching

reaction of trapped electrons by molecular oxygen follows a Langmuir–Hinshelwood mechanism, providing physico-chemical basis to a widespread assumption in photocatalytic mechanistic and kinetic studies.[20] We previously mentioned the kinetic importance of this oxygen-containing radical in specific reactions related mostly to dye degradation under visible light as well as reactions carried out using anion-doped titania or carbon nitride photocatalysts.[1,107,123,124]

In titania, considering gas phase reactions, superoxide radicals can be detected by EPR and IR spectroscopies. The peroxide can be only detected with IR (as mentioned previously, a band at 800 cm^{-1} may be associated with this species), being an EPR silent species. The EPR signal for the superoxide radical has been used in combination with ^{17}O in order to render maximum information: the exchange of the solid with such an oxide isotope and/or the use of ^{17}O marked molecular oxygen have been utilized.[143] The superoxide radical spectra of anatase and rutile samples are characterized by several g_{zz} values going from 2.025 to $ca.$ 2.019, indicating the presence of multiple (typically more than 2) species at the surface likely related to oxygen vacancies (which become populated by superoxide radicals roughly in 5–10%) as well as low coordinated (e.g. surface) Ti(III) centers.[144,145] Interestingly, a few molecules limit the production of the superoxide radical, particularly carbon dioxide blocks undercoordinated Ti(III) centers, indicating that the formation of radical species can be competitive with reactant and product molecules of the photocatalytic processes.[146]

The superoxide radical is easily protonated in liquid (water) medium, rendering HO$_2^\bullet$ species in modestly acidic solutions. This is customarily detected with the DMPO probe in methanolic medium as in water the radical easily disproportionates.[107,125,147] The adduct renders a 1:1:1:1:1:1 signal centered at g = 2.005 ± 0.001. As occurs with the DMPO adduct produced with hydroxyl radicals, the initial slope of the signal intensity $vs.$ time is frequently used to measure the radical formation potential of a sample to carry out quantitative studies. Note that the adduct formed with the 5-(diethoxyphosphoryl)-5-methyl-1-pyrroline N-oxide (DEPMPO) probe molecule has also been utilized for the selective detection of the superoxide radical.[148] Other probe molecules are clearly less selective. Alternative methods for superoxide radical detection use chemiluminescence with luminol or 6-(4-methoxyphenyl)-2-methyl-3,7-dihydroimidazo-[1,2-a]pyrazin-3-one hydrochloride.[149]

Electron trapping is also of particular importance in metal–semiconductor systems. Metal-like components can capture electrons under UV and, in the case of plasmonic systems, can undergo a light excitation process and donate electrons typically under visible (but also IR) illumination. Apart from the techniques above mentioned for the bare oxide systems and profusely used in this composite system to render the general picture summarized in the previous phrase,[1,21,105,107,108,150,151] we can mention here the usefulness of X-ray absorption spectroscopy (XAS) by highlighting a few examples of utilization. In the case of CuO$_x$–TiO$_2$ systems, the reduction of a relatively minor (14%) Cu(II) fraction to Cu(I) under reaction conditions (oxidation of 2-propanol) has been measured under UV illumination.

The process is reversible, leading to a full Cu(II) chemical state in the absence of the organic.[152] A similar reduction process is also shown to occur for (a small fraction of the) Cu supported on titania tested for CO_2 reduction with water under UV illumination.[153] Contrarily to the Cu redox behavior, noble metals such as Pt and Ir on TiO_2 were reported to modify their interaction with the support under UV illumination when they are in the metallic state.[154] Pt (in oxidized state) supported titania was also tested in water splitting and changes were visible in Pt–O bond distance and coordination number.[155] A more elaborate study used X-ray absorption and emission to substantiate the electron transfer between gold and titania. The study points out the key role of surface Ti centers sited in the vicinity of the metal as long-lived charge centers allowing the transfer process after light excitation of the metal.[156] The outcome of the study can be completed with the EPR view of the electron transfer.[150] Similarly, the XAS study of titania-based AuCu bimetallic catalysts utilized in alcohol photo-reforming indicates the significance of the optical properties of the metallic phase, formed by contact with the alcohol and/or light interaction, in maximizing hydrogen production upon visible light illumination.[157] Very recently a contribution highlighted the critical issue of matching the catalyst volume sampled with XAS and the one illuminated for a gas-phase photocatalytic reaction.[158] This requires the use of a X-ray microbeam due to the limited path of light through a solid catalyst. Applying micro-XAS for Cu and CuNi titania catalysts used for hydrogen production from bio-alcohols, the study was able to show the different physico-chemical properties of the non-noble metal(s) as a function of the analysis position from the surface. The (Cu rich) non-noble metal phases are oxidized in the initial stage (bottom part of the Fig. 10), fully reduced in (exclusive) contact with the reductive atmosphere (middle part of Fig. 10), and partially reduced (or partially oxidized) under the combined influence of light and the gas atmosphere (upper part of Fig. 10). So, fundamental aspects of the active phase depend on both the reactive mixture and the light influence. The study was also able to elucidate the synergistic effect of the Cu–Ni interaction with respect to the monometallic counterparts. This lies in the specific way metallic and reduced phase contact takes place.[158]

As mentioned at the beginning of this subsection other radical species not frequently considered to explain photocatalytic kinetic behavior and mechanisms are singlet oxygen, hydrogen peroxide, and the ozone-based radicals. Apart from the two most widely studied, previously discussed formation processes of $^1O_2$ (energy exchange with dyes as well as their presence in biological environments), Nosaka *et al.* suggest an additional path generated by oxidation of superoxide radicals by holes.[159] This radical species is commonly detected using EPR and 2,2,6,6-tetramethylpiperidine (TEMP), although in the
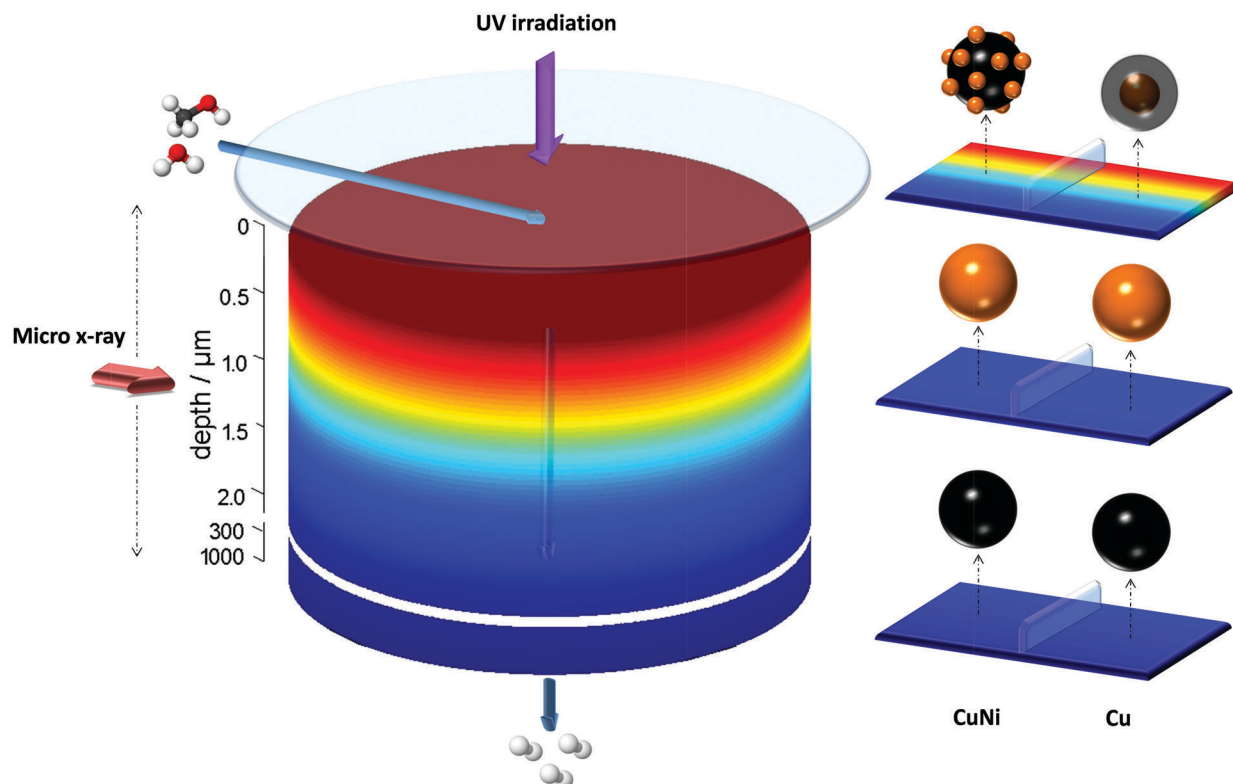
Fig. 10 Schematic view of the sample and experimental conditions. The sample is confined in a cell which allows simultaneous gas phase treatment and illumination from the top side. Arrows show the direction of the gas flow, illumination and incident X-ray micro-beam. The X-ray micro-beam probes non-noble metal chemical states and structure as a function of the depth from the surface. Panels on the right hand side depict the most relevant metal-containing phases (Cu(0) brown color; Cu(II) black color) for different depths described by the light intensity received. Cu and CuNi samples are considered. Reproduced with permission from ref. 158. Copyright 2018, Wiley-VCH.
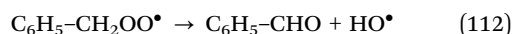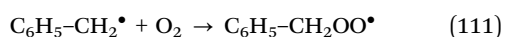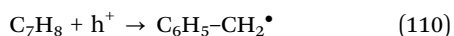
656 | *Chem. Soc. Rev.*, 2019, **48**, 637–682

This journal is © The Royal Society of Chemistry 2019

co-presence of superoxide radicals its detection would not be specific.[160,161] H_2O_2 is a relatively stable radical species photo-catalytic fate of which is commonly associated with the superoxide radical due to its formation path previously described ($O_2 + e^- \rightarrow O_2^{\bullet-}$; $O_2^{\bullet-} + e^- + 2H^+ \rightarrow H_2O_2$). Jointly with superoxide radicals, H_2O_2 is studied using chemiluminescence photometry,[162] although several optical tests based on absorption or luminescence spectroscopies are possible. Finally, the O_3^- radical is generated by the reaction of holes captured at lattice oxygen and molecular oxygen and is detected using EPR.[163]

4.2. Radical and/or intermediate species from organic and inorganic molecules

As stated in the initial paragraph of this section, Section 4, we will concentrate on the spectroscopic description of the initial species and key or kinetically relevant species of photocatalytic mechanisms. Selected examples are summarized in the following concerning typical families of organic (less frequently inorganic) molecules in relation to the photo-catalytic elimination of pollutants as well as the photo-production of hydrogen or photo-reduction of carbon dioxide.

4.2.1. Aromatic hydrocarbons. Among volatile organic compounds, aromatic hydrocarbons have been extensively studied within the field of photodegradation processes.[164] One of the model pollutants extensively studied by Diffuse Reflectance Infrared Fourier Transform Spectroscopy (DRIFTS) is toluene, as it is a typical atmospheric pollutant in urban areas. The initial process of adsorption of toluene on titania, parallel to the modification of the signals associated with the OH/water groups, shows several vibrational bands at 3074, 3035, 2940, and 2877 cm^{-1}.[165-167] The above mentioned bands located in the 3100–2850 cm^{-1} range have been assigned to νC–H stretching modes of the aromatic ring, detected together with asymmetric and symmetric νC–H of the methyl group (2927 and 2872 cm^{-1}, respectively).[168] The bands at 1603 and 1495 cm^{-1} have been assigned to the in-plane skeletal vibrations of aromatic rings, and the bands at 1460 and 1380 cm^{-1} have been associated with the asymmetric and symmetric CH_3 bending vibrations, respectively.[165,168] Studies focusing on the pretreatment of TiO_2 with H_2S and NH_3 indicate that the modification of the surface with H_2S satisfies the co-ordination of the surface Ti^{4+} sites and that the subsequent formation of sulfhydryl groups is favorable for toluene adsorption by the interaction of the aromatic ring with sulfhydryl groups.[169] In contrast, the presence of NH_3 leads to a decrease of the toluene adsorption.[169]

Once adsorbed, EPR analysis under illumination indicates the initial hole attack on the methyl group with the formation of a benzyl radical species (eqn (110)) which further reacts with oxygen to generate oxybenzyl radicals (eqn (111)) which likely evolve generating benzaldehyde (eqn (112)),[170] the most common intermediate detected in the literature for toluene photo-oxidation.

$$C_7H_8 + h^+ \rightarrow C_6H_5-CH_2^{\bullet} \qquad (110)$$

$$C_6H_5-CH_2^{\bullet} + O_2 \rightarrow C_6H_5-CH_2OO^{\bullet} \qquad (111)$$

$$C_6H_5-CH_2OO^{\bullet} \rightarrow C_6H_5-CHO + HO^{\bullet} \qquad (112)$$

Upon illumination and in consonance with EPR studies, in addition to the decrease in the intensity of several vibrational bands associated with the toluene molecule, new bands are commonly detected at (i) 1684 cm^{-1} attributed to the carbonyl vibration of the aldehyde group, and (ii) 1560 and 1358 cm^{-1} which may arise from the asymmetric and symmetric vibrations of the COO-group, respectively.[165,171] Other small (shoulder) bands around 1415–1650 cm^{-1} can be attributed to various vibrations of the aromatic ring, and methyl and carboxyl groups.[169] As commonly reported, catalyst deactivation is produced by surface adsorbed entities which would block the active sites.[166,171]

The case of benzene is less studied within the context of this review. In a mechanism with significant parallelism to toluene, the formation of an organic radical by hole and/or hydroxyl radical attack on the molecule, followed for the first case by formation of a peroxide radical with the help of oxygen, ends up in phenol, the most stable intermediate.[26,172,173]

Summarizing, the initial radical attack on the aromatic molecule occurs through the methyl group and the reaction proceeds yielding benzaldehyde (toluene) or phenol (benzene) as the primary product and carbon dioxide as the mineralization product.[26,66,99,172-177] Mechanistic studies suggest the presence (traces or minor products in the majority of cases) of benzyl alcohol, benzoic acid, hydroquinone, and/or cresols.[164,177,178] No obvious spectroscopic detection of products concerning the opening of the aromatic ring although the formation of (low weight) carboxylate and/or carbonate type species is frequently observed.[179]

4.2.2. Other hydrocarbons. Mechanistic studies of cyclohexane photodegradation processes have also been reported in titania samples.[180-184] EPR showed strong similarity to the benzene mechanism, with the formation of an organic radical by hole attack ($C_6H_{11}^{\bullet}$) and subsequent oxidation to form the peroxo species ($C_6H_{11}OO^{\bullet}$).[184] During the adsorption of the molecule, it is possible to detect bands corresponding to vibrations of liquid phase cyclohexane located at 1162 and 1128 cm^{-1}.[181] Following the initial stage of the (illuminated) reaction, in addition to several negative peaks typically located between 1120–1450 cm^{-1} due to disappearance of cyclohexane, signals appear at 1692 (first band to appear under illumination) and 1713 cm^{-1} corresponding to the C=O stretching vibration of adsorbed and desorbed (liquid phase) cyclohexanone, respectively.[180,181] Some authors also observed carboxylates and carbonates species, giving rise to the intense peaks at 1592 and 1390 cm^{-1} (carboxylate group symmetric/asymmetric stretching vibrations). The appearance of bidentate and monodentate carbonates (peaks at 1230 and 1048 cm^{-1}) was also reported from early times of the reaction.[181]

An interesting study has been carried out by Österlund et al.[185] concerning propane oxidation on mixed-phase anatase–rutile TiO_2 nanoparticles. The work focuses on the role of surface intermediates. Fig. 11 shows selected DRIFTS spectra acquired under illumination. Focusing on the most relevant issues of
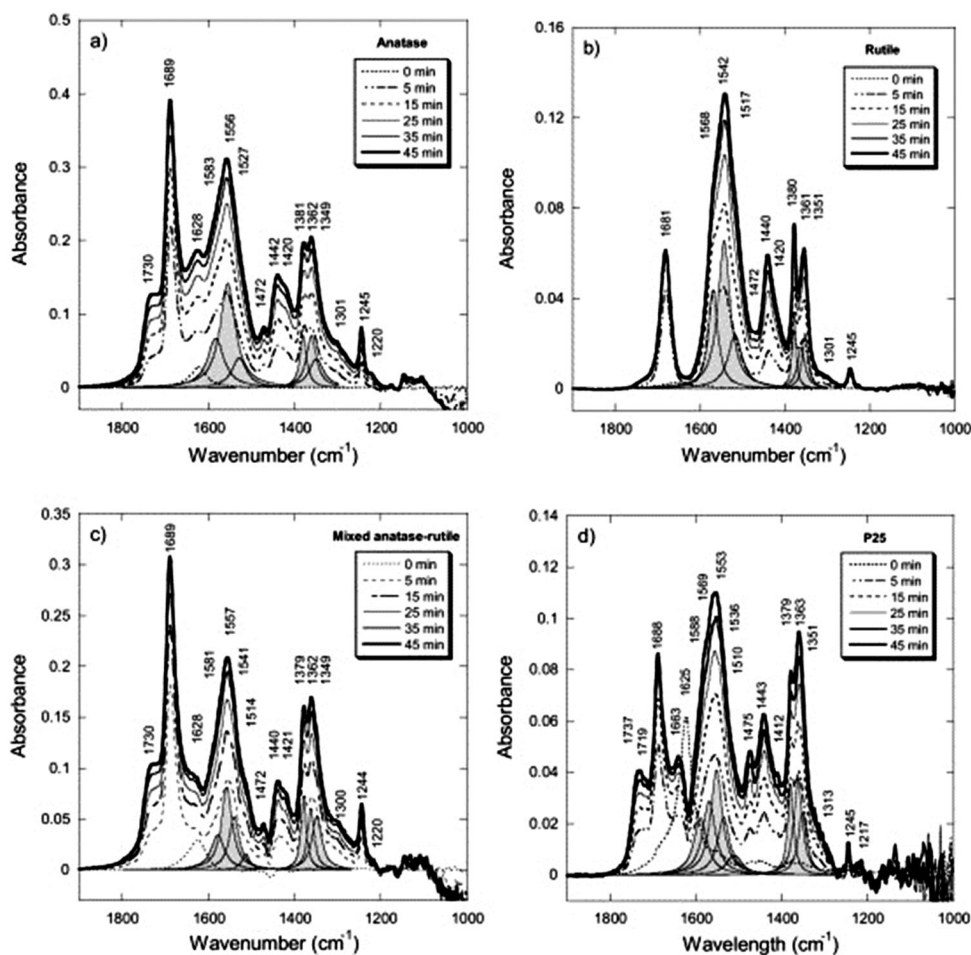
This journal is © The Royal Society of Chemistry 2019

Chem. Soc. Rev., 2019, **48**, 637–682 | **657**

Fig. 11 Diffuse reflectance infrared spectra at different times during photo-oxidation of propane for (a) anatase, (b) rutile, (c) mixed anatase–rutile, and (d) P25 commercial samples, respectively. The grey areas show the deconvoluted Lorentzian peaks in the ν_{as}(OCO) and ν_s(OCO) regions due to adsorbed formate, and aqueous formate. Reproduced with permission from ref. 185. Copyright 2007, with permission from Elsevier Ltd.
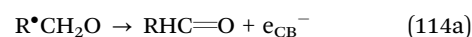
the study, the figures show there are some common bands for the different titania samples.
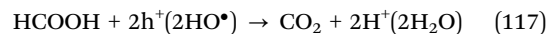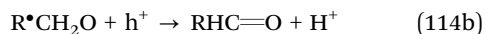
These common bands peak at 1689, 1555, 1440, 1380, 1360, and 1245 cm^{-1}. Besides, the spectra showed peaks around 2983 cm^{-1} (strong for the anatase sample), 2952 cm^{-1} (strong for all samples), 2870 cm^{-1} (strong), and 2744 cm^{-1} (medium).

Peaks that exist mainly for anatase occur at *ca.* 1735, 1472, 1420, 1150, and 1106 cm^{-1}, whereas the peak at 1568 cm^{-1} can be seen (as a shoulder to the 1541 cm^{-1} peak) mainly for the sample with pure rutile crystal structure. In addition, the P25 sample exhibits clearly distinguishable peaks at 1719 and 1663 cm^{-1}.[185] All these contributions, according to the results of the authors and references can be assigned to acetone and formate species.[28,185–187] TiO$_2$ modified by Pt has also been studied during photocatalytic oxidation of propane.[187] The results show that the presence of Pt modified the behavior of the bare titania support under irradiation conditions, leading to an infrared spectrum dominated by carbonyl vibrations, representing formic or acetic acid (ν(C=O) at 1712 cm^{-1}) and acetone (ν(C=O) at 1692 cm^{-1}) but not the previously observed carboxylate and/or carbonate bands, present in Pt-free samples.[187]

4.2.3. Alcohols. Among the oxygenated organic compounds, alcohol (mainly methanol, ethanol and aromatic alcohols) adsorption and photo-catalytic mechanism (in the presence or absence of oxygen) have been extensively studied.[188–198] For all alcohols, the results indicate that molecular and dissociative adsorption take place simultaneously.[164]

Using EPR the radical attack on alcohols taking place under illumination in the absence of oxygen would proceed in two steps. The alcohol firstly reacts with the photogenerated hole to form a carbon centered radical (eqn (113)), followed immediately by the transformation of the radical species, through injection of an electron to the conduction band of TiO$_2$ to form the corresponding aldehyde (or ketone). Alternatively a radical attack by hole species may also yield the stable molecule (eqn (114)). Since the second step is a thermally activated process, it occurs only at temperatures near room temperature and would display a higher activation energy.[107,199]

$$RCH_2OH + h^+ \rightarrow R^{\bullet}CH_2O + H^+ \quad (113)$$

$$R^{\bullet}CH_2O \rightarrow RHC{=}O + e_{CB}^- \quad (114a)$$

658 | *Chem. Soc. Rev.*, 2019, **48**, 637–682

This journal is © The Royal Society of Chemistry 2019

$$R^\bullet CH_2O + h^+ \rightarrow RHC\!\!=\!\!O + H^+ \quad (114b)$$

Focusing on methanol as a characteristic example, Fig. 12 shows the *in situ* DRIFTS analysis during methanol adsorption and photo-reforming reaction (so the absence of oxygen is noticed) for a platinized P25 sample.[190]

As can be seen in Fig. 12, the C–H region indicates the co-existence of methanol (2947/2838 cm^{-1}) and methoxy (2922/2814 cm^{-1}) species, as reported by many authors.[197,200,201] In addition, the works report the presence of carboxylates, specifically formate groups (peaks at 1550–1510, and 1360–1350 cm^{-1}) and maybe other carboxylate species (broad peaks presented in the range 1440–1410 cm^{-1}).[190,196,202–204] During the photoreaction, the authors detect a progressive consumption of methanol/methoxy species and CO$_2$ generation (signal around 2350 cm^{-1}), as well as additional carboxylate moieties at the surface of titania with peaks at 1530–1520 or 1400–1460 cm^{-1} depending on the sample studied.[190] Broadly speaking, the spectroscopic works support or can be rationalized considering a stepwise transformation of methanol:

$$CH_3OH + 2h^+(2HO^\bullet) \rightarrow CH_2O + 2H^+(2H_2O) \quad (115)$$

$$CH_2O + H_2O + 2h^+(2HO^\bullet) \rightarrow HCOOH + 2H^+(2H_2O) \quad (116)$$

$$HCOOH + 2h^+(2HO^\bullet) \rightarrow CO_2 + 2H^+(2H_2O) \quad (117)$$

$$2H^+ + 2e^- \rightarrow H_2 \quad (118)$$
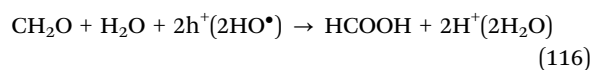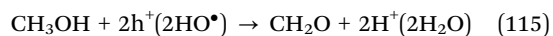
generating hydrogen (or the corresponding precursor species) in each one of the stages. Depending on the work, the key surface intermediates are at specific places of the stepwise transformation but the presence of formates is clearly observed in all cases. For example, depending on the alcohol chemical formula the balance between carbonates and carboxylates could favor the first (higher alcohols) or the second (lower alcohols and particularly methanol) species.[188,201] Also, the quantity of water present at the surface can play a critical role in the formate interaction with the titania surface and its subsequent evolution to CO$_2$.[205] Eqn (115)–(117) thus consider a relatively general mechanism triggered by holes or hydroxyl-type radicals. However, there are alternatives such as the so-called "current-doubling effect" which considers that after a first hole attack on methanol (or other molecules) the generated radical species can donate an electron to the semiconductor (eqn (114a)) evolving at the same time into formaldehyde.[107,200,206]

Particularly interesting are the results presented in Fig. 12 and associated with the CO formation, giving IR signals located around 2065–2060 and 1997 cm^{-1}, under *in situ* experiments.[196] The signals are associated with carbonyl species absorbed in
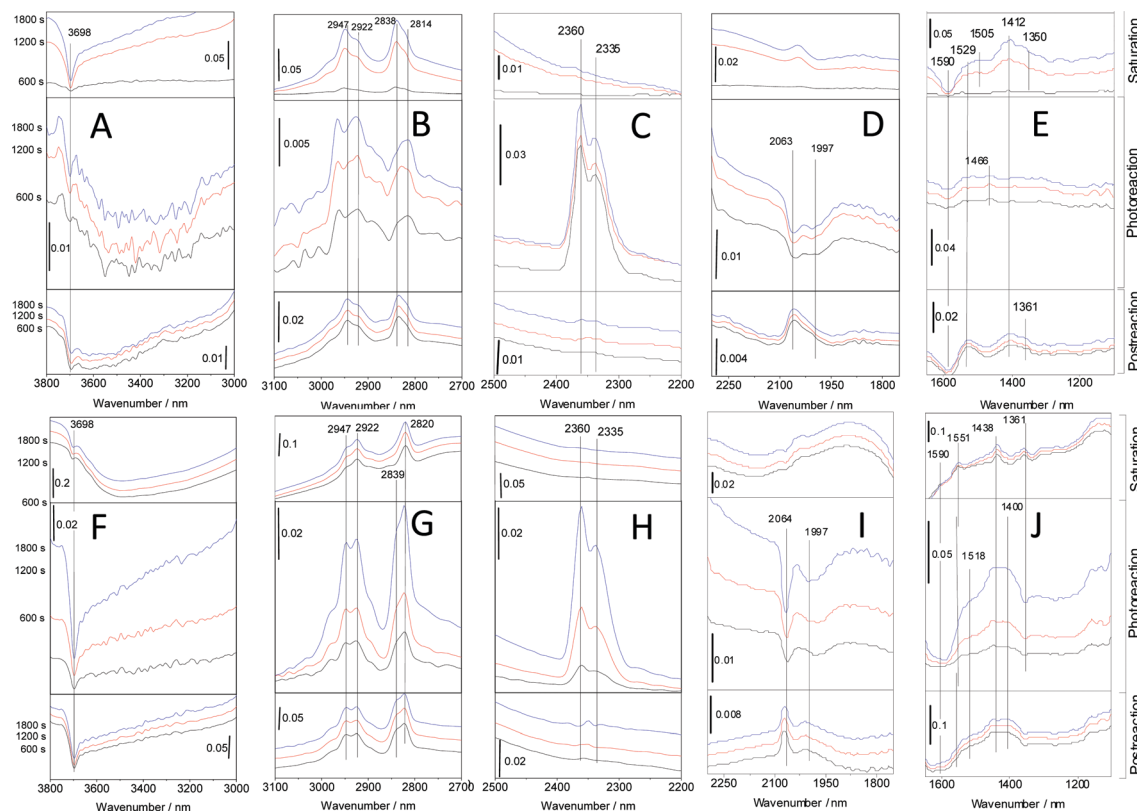

Fig. 12 *In situ* DRIFTS spectra for methanol photo-reforming under reaction conditions. Upper panel, P25-5Pt (0.5 wt% Pt onto P25 prepared by chemical deposition with a metal/reductant ratio of 5); lower panel, P25-10Pt (0.5 wt% Pt onto P25 prepared by chemical deposition with a metal/reductant ratio of 10) samples. Difference spectra obtained during saturation with an alcohol:water mixture (upper zone of each panel), under reaction-illumination conditions (middle part) and subsequently under dark conditions (bottom part) are presented. Reproduced with permission from ref. 190. Copyright 2017, Elsevier Ltd.

This journal is © The Royal Society of Chemistry 2019

Chem. Soc. Rev., 2019, **48**, 637–682 | **659**

metallic Pt sites. Based on the intensity behavior of CO and other surface species, the authors suggest that, despite the similar mechanism for producing carbon oxides from the activated alcohol moieties present in Pt-promoted systems, the most efficient the conversion of CO to CO_2 is the most active the catalyst is. This appears correlated with the transformation of carboxylate-type species into CO_2 through first the photocatalytic dehydration of the carboxylate to produce CO (eqn (119)) and then the conversion of the generated carbon monoxide molecule by a water gas shift type reaction (eqn (120)), with maximization of the hydrogen yield of the photo-reforming process.[196] The study thus suggests that eqn (115)–(117) are simplifications of the surface processes taking place under reaction conditions.

$$HCOO^- \rightarrow CO + OH^- \quad (119)$$

$$CO + H_2O(HO^{\bullet}) \rightarrow H_2(1/2H_2) + CO_2 \quad (120)$$
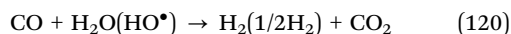
The overall reaction (sum of eqn (119) and (120)) can be interpreted as a dehydrogenation of formic acid. Depending on the CO production pathway and quantity its role can be positive or negative. Its absence in the gas-phase is usually considered positive for the production of hydrogen and its presence would have typically a negative role in photo-activity. The positive or negative role depends on (i) its degree of interaction with the metal as strong adsorption leads to surface poisoning of Pt, (ii) the handling of CO by the metal–support interface and thus its elimination from the metal surface; (iii) the nature of the formate species as mono or bi-dentate formates or methyl-formate evolve more or less easily (partially as an effect of neighboring water) following eqn (119).[190,207] Note on the other hand that other pathways of carbon monoxide formation typical of noble metal catalysts such as decarbonylation of formaldehyde currently lack experimental support in the context of hydrogen photoproduction.

Even more complex mechanisms than the one summarized in eqn (115)–(118) would need to be considered if other carbon-containing co-products are detected in the production of hydrogen from alcohols. In several works the presence of methane or other short chain hydrocarbons can be mentioned. Methane can be generated, for example, from acetic acid by hole attack, by electron attack on methanol, carbon dioxide and other molecules, or from thermally driven carbon dioxide hydrogenation.[1,117]

Photo-oxidation (in presence of oxygen) of alcohols has also been studied.[191,193,195,196,208] Infrared spectroscopy showed similar intermediates to those presented previously in the absence of oxygen although a few exceptions or details not discussed previously here can be mentioned. El-Roz and coworkers[191] studied the mechanism of methanol photo-oxidation to methylformate and carbon dioxide on TiO_2. Besides the analysis of the reaction behavior of methanol, the first step of the reaction (dissociation of methanol) was studied using CD_3OH, as well as the role of oxygen by analyzing labeled ^{18}O-methanol ($CH_3^{18}OH$) in the presence of an excess of $^{16}O_2$. The authors identified bands at 1209 and 1754 cm^{-1} confirming the generation of methylformate from methanol (decrease of the band

at 1033 cm^{-1}). The results indicate however that the main pathway for methanol photo-oxidation goes through the chemi-sorption of methanol as surface methoxy species, then their oxidation to formates and, finally, into CO_2. Presumably, the methyl formate is generated by the coupling of methoxy and formates (formyl species) and thus can be produced in the presence or absence of oxygen. The selectivity for methylformate vs. carbon dioxide would thus depend on the surface coverage of methoxy species and the fate to be further attacked by charge carriers or react with other adsorbed species.[191]

A recent study using gold promoted titania samples suggests that ethanol photo-oxidation goes through an activation step going from acetaldehyde species and leading to oxalate species (eqn (121)), the latter detected by the presence of a band at 1320 cm^{-1}. This chemical step would be a previous, thermo-photo-activated step to the formation of formates (as summarized in eqn (121) and (122)) and carried out at the metal–support interface.[208]

$$CH_3CO^{2-} + 3O_2 + 3e^- \rightarrow C_2O_4^{2-} + 3OH^- \quad (121)$$

$$C_2O_4^{2-} + H^+ \rightarrow HCOO^- + CO_2 \quad (122)$$
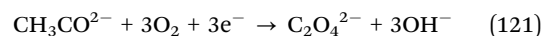
In a quantum efficiency study of 2-propanol photo-degradation in the gas phase,[209] the adsorption of the molecule generates bands at 2970, 2932, 2863 (νCH_3), 1458 ($\delta_{as}(CH_3)$), 1380 ($\delta_s(CH_3)$), 1301, 1249 ($\delta(OH)$), 1162 ($\delta(C–C)$), and 1126 ($\nu(C–O)$) cm^{-1}. After illumination of the sample, authors observe the appearance of new bands at 2952, ∼2889, 1661 cm^{-1} indicative of acetone formation (most characteristic peak at ca. 1660 cm^{-1}; $\delta(C–O)$), as well as peaks at 1577 ($\nu_{as}(OCO)$) and 1347 ($\nu_s(OCO)$) cm^{-1} strongly indicative of the presence of formate species. In addition, other intermediates leading to a band at ca. 2830 cm^{-1} were also identified, suggesting the presence of formaldehyde or similar species.[209]

In a detailed study of the photo-oxidation of 2-propanol using TiO_2,[210,211] the authors identified bands at 1131 cm^{-1} (νC–O) of isopropoxy species formed by a dissociative adsorption according to the CH_3–CHOH–CH_3 + sites + sites' $\rightarrow$ CH_3–CHO_{ad}–CH_3 + sites'–H_{ad} reaction, where sites and sites' are two surface sites of the TiO_2 surface.[210] Other contributions typically detected and assigned to pure 2-propanol are ca. 2972, 2938, and 2872 cm^{-1} ($\nu(CH)$), 1468, 1458 cm^{-1} ($\delta_{as}(CH_3)$), 1385 and 1367 cm^{-1} ($\delta_s(CH_3)$) and $\delta(CH)$ mode at 1343 cm^{-1}.[212] Upon UV irradiation, bands associated with acetone (e.g. 1696 cm^{-1}) increase during the first 40 min and then decrease progressively. Bands at 1640 cm^{-1} (undissociated H_2O formed in part during the adsorption of isopropyl alcohol); 1557 cm^{-1} concerning the asymmetric stretching of COO groups present in adsorbed species such as formate and carbonate species (uni- and bidentate carbonates and carboxylates); and 1420–1350 cm^{-1} for the symmetric stretching of COO groups were also detected.[210] In addition, at 1380 cm^{-1} the authors detect a C–H bending, ascribed to adsorbed formate. The manuscript highlights that, during the photoreaction, the 1696 cm^{-1} band due to the (dominant) final product decreases whereas that at 1557 cm^{-1} remains unchanged proving that the adsorbed species characterized by the IR band

660 | Chem. Soc. Rev., 2019, 48, 637–682

This journal is © The Royal Society of Chemistry 2019

at 1557 cm^{-1} is likely formed by the transformation of the acetone species. They also note that the coverages of the intermediate species of the transformation of 2-propanol into acetone are very small and in some cases barely detectable.[210]

Among the aromatic alcohols, benzyl alcohol photo-transformation has been analyzed in a significant number of studies. Fig. 13 depicts the results using TiO$_2$ prepared by the authors during ATR (Attenuated Total Reflection)-FTIR (Fourier Transform Infrared) photo-oxidation of benzyl alcohol.[213]

In this case, it is common to detect the following signals during the adsorption process: 1497, 1455 (skeletal vibrations of the aromatic ring), 1369 (O–H in-plane deformation mode of the alcohol), 1208 (C–C stretching vibration), 1079, 1035, 1018 and 1006 (benzoate formation) cm^{-1}.[213] Regarding also the benzyl alcohol molecule, signals around 3066 and 3033 cm^{-1} were ascribed to the C–H stretching vibrations of the aromatic ring of the alcohol (see Fig. 13A and B).[213,214] Using P25 as catalysts, besides the water bending band at 1645 cm^{-1}, the most prominent bands detected during photo-oxidation peak at 1711 (C=O stretching vibration of the carbonyl group of benz-aldehyde),[215] 1686, 1603, 1530, 1496, 1451, 1415 1403 (benzoic acid as benzoate),[216] 1274 and 1246 cm^{-1} (oxalate species).[213] Other authors detect bands at 1535 and 1505 cm^{-1} that were assigned to the ν_{as}(COO) mode and bands at 1418 and 1405 cm^{-1}, ascribed to the ν_{as}(COO) vibration of carboxylate-type moieties.[213,217]

So, from the joint use of the information coming from spectroscopic studies, the presence or absence of oxygen has a differential effect in the initial (e.g. before carboxylate or carbonate formation) organo-radical species formed with oxygen to activate the alcohols as detected by EPR and IR, as well as the last steps of the reaction in the absence of oxygen where the involvement of specific OH groups in a water gas shift type step has been postulated. Organo-radicals would be responsible for the production of oxygen-rich intermediates such as oxalate. In both cases, the role of the metal–support interface in metal-promoted catalysts has been highlighted as critical to produce specific intermediates presumably generated with lower activation energies than in the bare oxide.[190,208,209]

4.2.4. Aldehydes and ketones. Formaldehyde and acetaldehyde are two of the most studied molecules in photocatalytic degradation processes. During the adsorption of formaldehyde on TiO$_2$, typical bands are observed at 1502 cm^{-1} δ(CH$_2$) of H-bonded formaldehyde, δ(CH$_2$) = 1485 cm^{-1} of dioxymethylene species, νCO = 1429 cm^{-1} of bidentate bonded formaldehyde and ν_{as}(COO) = 1550 cm^{-1} of bidentate formate.[218] Bands at 2956, 2913, 2863 and 2759 cm^{-1} assigned to the C–H stretching mode can also be observed.[219–221] Under UV irradiation, formate species associated with bands at 1572 and 1361 cm^{-1} can be detected, while the characteristic bands of formaldehyde decrease. The analysis of dry and humid condition DRIFT experiments suggests that upon UV irradiation the characteristic band of formaldehyde decreases more quickly, while that of formate species increases more quickly when water vapor is introduced. A similar result was observed during the conversion of formaldehyde to CO$_2$, so the conversion of adsorbed formaldehyde to formate species could be determinant to mineralize efficiently the formaldehyde to CO$_2$ and water.[219] A recent study however indicates that formate oxidation to carbonate could be the rate determining step in the oxidation mechanism of formaldehyde and considering Au/TiO$_2$ catalysts.[222]

Fig. 14 shows a survey plot summarizing *in situ* DRIFT spectra on TiO$_2$ samples utilized in acetaldehyde photo-oxidation
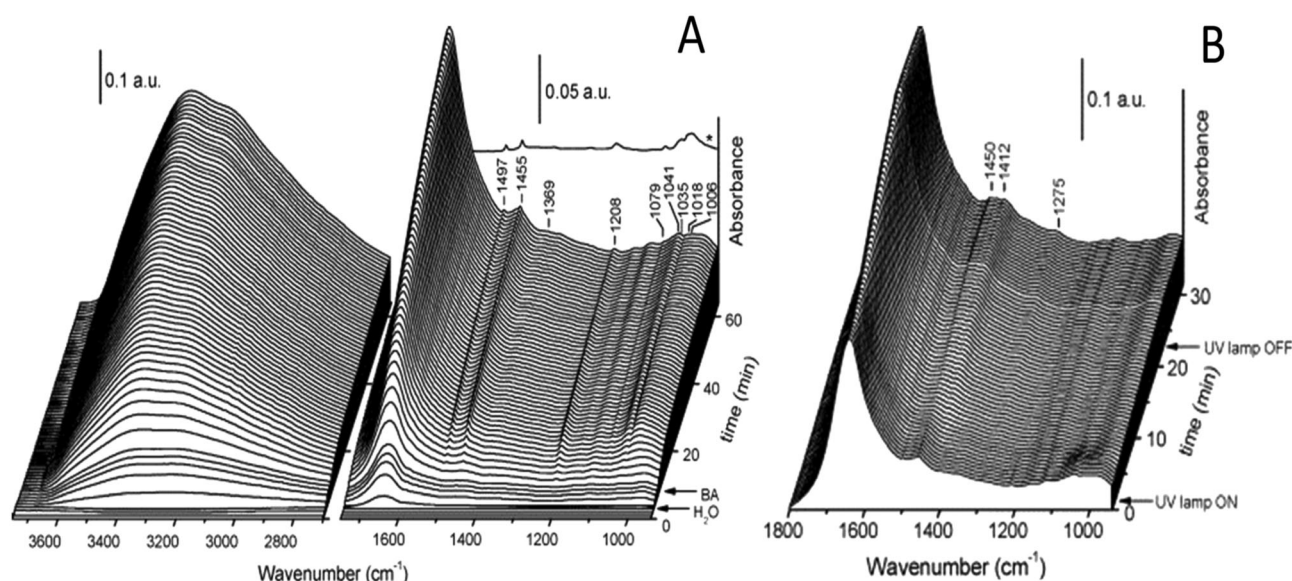
Fig. 13 (A) Time-resolved ATR-FTIR spectra of TiO$_2$ (sample synthesized by boiling aqueous solutions of titanium tetrachloride) thin film recorded during adsorption of water and benzyl alcohol vapours at room temperature. The arrows indicate the time when each adsorbate was introduced into the cell. The spectrum of neat benzyl alcohol has been included for comparison. (B) Time-resolved ATR-FTIR spectra recorded during irradiation of TiO$_2$ thin film in an atmosphere of synthetic air saturated with water and benzyl alcohol. The arrows indicate the time when the UV lamp was switched on and off. Adapted with permission from ref. 213. Copyright 2008, Elsevier Ltd.
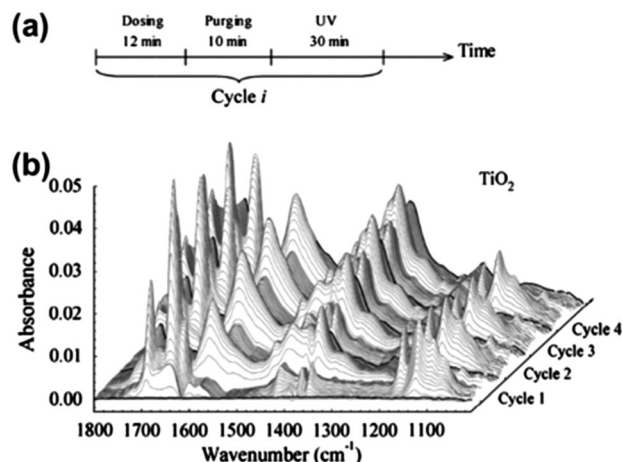
This journal is © The Royal Society of Chemistry 2019

Chem. Soc. Rev., 2019, **48**, 637–682 | **661**

Fig. 14 (a) Schematic representation of the experimental procedure used in the *in situ* FTIR experiments following acetaldehyde photo-oxidation. (b) Absorbance spectra acquired as a function of time and consecutive cycle number on films of TiO_2. Adapted with permission from ref. 223. Copyright 2013, with permission from Elsevier Ltd.

during a cycling experiment schematically described in part (a) of the figure.

The identification of the most important contribution is in agreement with the characteristic of the acetaldehyde $\nu(C\!=\!O)$ vibration at 1693 cm^{-1}, and weaker bands of $\nu(C\!=\!O)$ Ti–O$=$CH(CH)$_2$CH$_3$ at 1653 cm^{-1}, δ(CH$_3$) d-deformation Ti–O$=$CHCH$_3$ at 1421 cm^{-1}, δ(CH) bending Ti–O$=$CHCH$_3$, δ(C–H) HCOO$^-$ at 1376 cm^{-1}, δ(CH$_3$) s-deformation; Ti–O = CHCH$_3$ ν_s(C–O); symmetric O–C–O stretching in HCOO$^-$ at 1355 cm^{-1}, m(C–C); Ti–O$=$CH(CH)$_2$CH$_3$ at 1168 cm^{-1}, ν(C–C); Ti–O$=$CHCH$_3$ at 1129 cm^{-1}, and ρ(CH$_3$) Ti–O$=$CH(CH)$_2$CH$_3$ at 1099 cm^{-1}.[223] When the sample is irradiated, a broad peak at 1580 cm^{-1} and associated with ν_{as}(C–O); asymmetric O–C–O stretching in surface absorbed HCOO$^-$ was detected. The work also reported peaks at 1376 cm^{-1} (δ(CH) bending; Ti–O$=$CHCH$_3$ and/or δ(C–H); HCOO$^-$) and 1355 cm^{-1} (δ(CH$_3$) s-deformation; Ti–O$=$CHCH$_3$ and/or ν_s(C–O); symmetric O–C–O stretching in HCOO$^-$).[223]

As an example for acetone, Coronado and co-workers carry out an operando FTIR spectroscopy study during photocatalytic oxidation of acetone vapors over semiconductor films containing TiO_2 and ZrO_2.[224] The authors detect different vibration modes according to the following identification; acetone: ν(C–H) 2975–80 cm^{-1}, 2927–29 cm^{-1}, $\nu(C\!=\!O)$ 1701–1685 cm^{-1}, δ_{as}(CH$_3$) 1425–23 cm^{-1}, δ_s(CH$_3$) 1370–68 cm^{-1}, ν(C–C); formate: ν(CH) 2870 cm^{-1}, ν_{as}(COO) 1571 cm^{-1}, ν_s(COO) 1358 cm^{-1}; acetate: ν_{as}(COO) 1584 cm^{-1}, ν_s(COO) 1420 cm^{-1}; formaldehyde; $\nu(C\!=\!O)$ 1744–42 and bicarbonate: ν_{as}(COO) 1447 cm^{-1}. The comparison of the samples SS (Ti$_{0.90}$Zr$_{0.10}$O$_2$ mixed oxide) and Z/T (10% ZrO$_2$/TiO$_2$ metal oxides) of the integrated intensity of adsorbed acetone (integrated between 1720 and 1660 cm^{-1}), along with the changes in the background intensity at 1020 cm^{-1} (integrated between 1000 and 1060 cm^{-1}), is displayed in Fig. 15.[224]

The figure also shows the evolution of formate (integrated between 1635 and 1500 cm^{-1}) and CO_2. Both photoactive
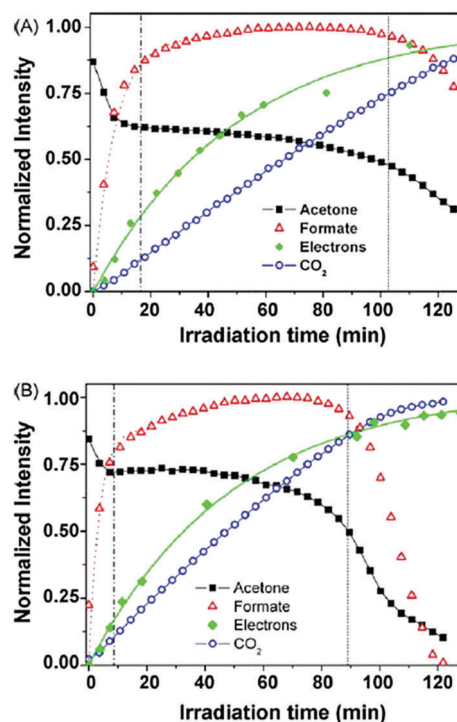

Fig. 15 Variation of the normalized intensities of adsorbed acetone (squares) and formate (up-triangles) and aldehydes (down-triangles) detected during UV-irradiation of (A) SS (Ti$_{0.90}$Zr$_{0.10}$O$_2$ mixed oxide) and (B) Z/T (10% ZrO$_2$/TiO$_2$ metal oxides). Vertical lines mark the different stages of the photocatalytic processes. Adapted with permission from ref. 224. Copyright 2009, Elsevier Ltd.

materials show comparable trends, which define three different stages (dotted vertical lines) according to the coverage of intermediate species. According to the analysis of the authors, in the first and shortest period, a rapid decrease of the amount of adsorbed acetone takes place in parallel to the rise of a formate species for the Zr-containing samples. EPR studies by other authors indicate the formation of organoperoxy species as the initial step of the reaction for acetone but also other molecules such as 2-butanone, 4-heptanone, cyclopentanone and cyclohexanone. The specific radicals (more than one suggested) formed for each molecule depend on a significant number of experimental variables but particularly on oxygen partial pressure.[225] These species would evolve in the carboxylate-type (frequently formate in the case of acetone) species detected by infrared.

As previously described, during the second step presented in Fig. 15 the formate adsorbed species can be considered roughly constant. Finally, in the last period the concentration of all adsorbed species began to decrease (formate decrease is sample dependent), while CO_2 concentration reaches its maximum value. The overall conclusion using a simple kinetic analysis indicates that formate species gain stability near Zr sites for several reasons (adsorption but also decrease of active radicals able to further oxidize the molecule) and cannot evolve into carbon dioxide in the samples not having free anatase surface sites. This indicates that not only the handling of charge carrier

species is of significance but also surface characteristics of the solids drive the final catalytic outcome.[224]

4.2.5. Acids. During the adsorption process, it is accepted that formic acid dissociates on TiO_2 surfaces. Using rutile, specifically a (111) single-crystal plane, formate is shown to bind as monodentate (η1-formate) and chelating (η2-formate) species.[226] P25 TiO_2 shows bands at ~1553 cm^{-1} ($\nu_{as}(OCO)$), 1363–1379 cm^{-1} ($\nu_s(OCO)$) and ~1385 cm^{-1} δ(C–H) likely produced by bidentate formate and ~1682 cm^{-1} ($\nu_s(C{=}O)$), 1250–1227 cm^{-1} (n(CO)) and ~1325 δ(C–H) coming from the adsorbed, mostly unperturbed acid.[227,228] Similar bands have been detected using anatase powders. Apart from the formate and formic acid peaks, some contributions associated with (quasi-free, liquid phase) $HCOO^-$ ions are usually detected at ~1582 cm^{-1} ($\nu_{as}(OCO)$), ~1351 cm^{-1} ($\nu_s(OCO)$) and ~1391 cm^{-1} (δ(C–H)).[185,229]

From EPR measurements the photo-evolution of acids has been shown to proceed through the formation of methyl-type radicals in the case of the photo-Kolbe reaction (eqn (123) and (124)),[230] or the formation of carboxyl (formyl) radicals generated by electron attack (Ti^{3+} species) on the reactant molecule in reductive pathways (eqn (125)).[231] However, the analysis in typical photo-degradation reactions is mostly carried out using infrared spectroscopy.

$$R–CH_3–COOH + Ti^{4+}–O^{2-} \rightarrow R–CH_3–CO_2^- + Ti^{4+}–OH \tag{123}$$

$$R–CH_3–CO_2^- + h^+ \rightarrow R–CH_3 + CO_2 \tag{124}$$

$$R–CH_3–COOH + Ti^{3+} \rightarrow R–CH_3–CO + Ti^{4+}–OH \tag{125}$$
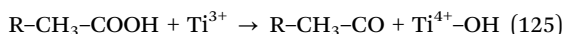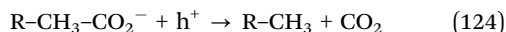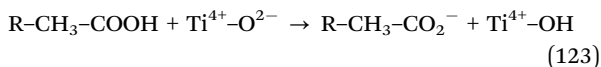
Under reaction conditions, and for example using Fe-doped TiO_2 samples,[232] a decrease of the formic acid bands at 1730 cm^{-1} (νC$=$O) and 1200 cm^{-1} (νCO–OH) is observed concomitantly to the growth of formate vibration bands. The latter concerns the $\nu_{as}(OCO)$ and $\nu_s(OCO)$ modes, detected between 1600–1560 and 1370–1306 cm^{-1}, respectively.[232,233] The studies report a band at 1396 cm^{-1} attributed to δ(CH) vibration for doped and titania reference samples; however, for bare TiO_2, the $\nu_s(OCO)$ vibration band appears at 1356 cm^{-1} while it appears at higher wavenumbers, about 1362 and 1370 cm^{-1} for doped materials. Interestingly, doped catalysts show a progressive shift of the $\nu_{as}(OCO)$ vibration to higher wavenumbers (from 1542 to 1615 cm^{-1}) and a $\nu_s(OCO)$ shift to lower wavenumbers (from 1360 to 1350 cm^{-1}) as the Fe content of the catalysts is increased. This is attributed to the formation of formate species simultaneously adsorbed on Ti and Fe atoms.[232]

Similar to formic acid, acetic acid follows the same trends previously described, that is, molecularly adsorbed acetic acid and surface-coordinated acetate are commonly observed under dark conditions.[234,235] On the surface of different titania samples, typical acetic acid ν(C–O), δ(CH), and ν(C–O) vibrational bands around 1711, 1675, 1380, and 1300 cm^{-1}, respectively are usually detected.[202] Other peaks associated with $\nu_{as}(COO)$ in the 1516–1544 cm^{-1} region (surface-coordinated acetate) and the 1550–1560 cm^{-1} region (aqueous acetate ions), and the $\nu_s(COO)$ bands in the 1447–1452 cm^{-1} region (surface-coordinated acetate)

and the 1418–1423 cm^{-1} region (aqueous acetate ions) can also be detected. Differences between anatase, rutile and brookite during the absorption process are detailed in ref. 202. During the photodegradation process the initial steps were analyzed with the help of EPR. Methyl radicals ($^\bullet$CH$_3$) were formed both by direct and indirect hydroxyl-radical pathways. Contrarily carboxymethyl ($^\bullet$CH$_2$COOH) radicals were produced through an indirect, hydroxyl-mediated mechanism.[236] In both anatase and rutile samples, IR testing under light was shown to produce bands at ~1550 and ~1350 cm^{-1} produced by $\nu_{as}(COO)$ and $\nu_s(COO)$ vibrations of carboxylate species. Anatase generates also a band at ~1590 cm^{-1} (formate) while for rutile, where acetic acid is more prone to dissociation upon adsorption, the acetate species does not show significant variation from dark conditions.[202]

Fig. 16 presents a graphical scheme of the acetic acid photodecomposition pathways for the different TiO_2 samples as elucidated from FTIR results. In anatase and brookite, formate (νCH band) contributions at 2850 and 2877 cm^{-1} were identified, and at 2877 cm^{-1} for brookite one. The last signal remains after extended illumination times, indicating the stability of such surface species. Finally, for anatase samples, according to the analysis of the authors, bands at 1740 and 1720 cm^{-1} may be related to an asymmetrically coordinated end-on Ti–O–C$=$O species rendering the –C$=$O moiety having carbonyl vibrational character.[28,202] The different carboxylate species present at the different titania polymorphs render CO_2 or carbonate species at the surface (Fig. 16). The presence of carbonate species is pointed out as the main source of photo-activity deterioration with time.

Another interesting group of molecules corresponds to the (di)carboxylic acids. Glycolic acid liquid phase photo-oxidation
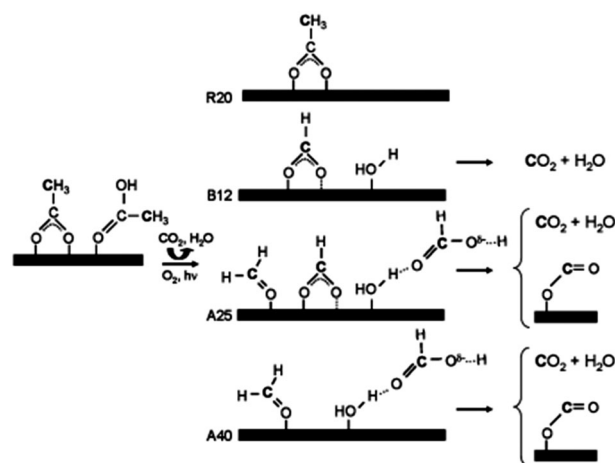
Fig. 16 Schematic drawing of the reaction pathways for photoinduced decomposition of acetic acid on anatase, brookite, and rutile. Acetic acid and acetate coexist on the surface prior to illumination. The bidentate coordination of formate is tentative and is drawn as a weakly, bridging bonded species (dashed lines). Bold and normal font styles for carbon denote β-carbon (C) and α-carbon (C), respectively. Samples are named A25 and A40 (anatase), B12 (brookite) and R20 (rutile). Number code is associated with particle size (25, 40, 21 and 20 nm, respectively). Reproduced with permission from ref. 202. Copyright 2010, American Chemical Society.

was subjected to an *in situ* FTIR study on P25 titania showing an intense band at 1668 cm^{-1} together with a weaker 1353 cm^{-1} band from the antisymmetric and symmetric carboxylate stretch modes, respectively. C=O and C–O stretch modes corresponding to the glyoxylate ion in solution were also detected, respectively, at 1598 and 1382 cm^{-1}.[237] Also, bands appearing at 1718, 1412, and 1254 cm^{-1} can be associated with adsorbed oxalate on TiO_2.[237,238] Malonic and succinic acid photo-oxidation processes over P25 TiO_2 have been study by Igor Dolamic and Thomas Bürgi using an *in situ* ATR-IR approach.[239] For the malonate acid case, the study of the air-saturated aqueous adsorption process renders (most intense or characteristic) bands at $\nu_{as}(COO)$ at 1625 and 1575 cm^{-1} and $\nu_s(COO)$ at 1436 and 1353 cm^{-1}.[239,240] The $\delta(CH_2)$ mode at 1259 cm^{-1} was also detected. After illumination oxalate-related bands appeared, and the corresponding spectrum showed bands at 1689 and 1669 cm^{-1} which correspond to the Fermi resonance splitting of the C=O group(s) stretching vibrations and bands at 1401 and 1272 cm^{-1}, associated with $\nu(C–O) + \nu(C–C)$ combination modes.[239] Additionally, a band at 1249 cm^{-1} was observed and assigned as the $\delta(O–C=O)$ vibrational mode.[239] Unlike for malonate acid, the analysis of succinic acid showed only one band for the symmetric COO$^-$ stretching vibration and one for the antisymmetric COO$^-$ stretching vibration.[239] Upon illumination, bands at 1708 and 1690 cm^{-1} can be assigned to oxalate species. The broad band centered at around 1600 cm^{-1}, which becomes weaker during the experiment, likely belongs to both malonate and oxalate species. A kinetic analysis of their appearance and disappearance suggests that succinate is transformed into malonate and then to oxalate.[239] Generally, the photo-degradation of aliphatic dicarboxylic acids would proceed through the consecutive shortening of the hydrocarbon chain. Each of the consecutive steps may occur within a photo-Kolbe reaction eliminating CO_2 and generating a carbon-centered radical, which in subsequent steps evolves into a carboxylate moiety.

4.2.6. Dyes. The initial steps of dye excitation were followed commonly using EPR. For example, Alizarin red showed a strong single peak at $g = 2.0067$ after 532 nm light excitation, attributed to the radical formed from the molecule after transferring an electron to titania.[241] This corresponds to the excitation of the molecule occurring under visible light as previously discussed.

Methylene blue, which is one of the most studied contaminated dyes was subjected to analysis by Chuang and coworkers using P25 titania.[242] According to the authors' results, the adsorption of methylene blue on TiO_2 shows bands at 2926 cm^{-1} $\nu_{as}(CH_3)$, and at 2858 and 2815 cm^{-1} corresponding to the C–H symmetric stretching of the CH_3 group ($\nu_s(CH_3)$); those corresponding to the $\nu(C=N)$ central ring at 1600 cm^{-1}; $\nu(C=C)$ side ring at 1488 cm^{-1}, the multiple ring stretchings at 1388 cm^{-1}, and the νC_{Ar}–N situated at 1333 cm^{-1}. Finally, bands at 1243, 1247, 1178, 1143 cm^{-1} associated with interactions between CH_3 and the nitrogen atom $\nu(N–CH_3)$ were also detected. Under UV irradiation, the total oxidation of the molecule takes place, rendering CO_2 (2362 cm^{-1}), H_2O, NH_4^+ (3163 cm^{-1}) and SO_4^{2-} (1228 cm^{-1}).

In addition, the following bands are usually accepted as transient intermediates in the way to complete mineralization; $\nu C=O$ at 1721 cm^{-1} from the carbonyl bond of an aldehyde, R–NH_3^+ at 1648 cm^{-1}, carboxylate (RCOO$^-$) at 1566 cm^{-1}, and C_{Ar}–O of phenol at 1265 cm^{-1}.[242] In the case of Acid Blue 9, similarly to the previous case, bands at 1580 and 1618 cm^{-1} were identified, respectively, as cyclic conjugated C=N stretching and C=C stretching coming from the conjugated aryl moieties. Regarding the CH_3 entities, the authors detect asymmetric (2978 cm^{-1}) and symmetric (2872 cm^{-1}) stretching vibrations, as well as the band at 2933 cm^{-1} which came from the CH_2 asymmetric stretching vibration.[243] The authors also detected the 3063 cm^{-1} band and bands at 1407 and 1390 cm^{-1} which can be assigned to C–H bending vibrational modes.[243] A remarkable decrease of bands at 1580, 1407 and 1390 cm^{-1} was detected under irradiation and was ascribed to the degradation of cyclic conjugated C=N stretching and C–H bending from the ethyl group. This leads to color removal of Acid Blue-9 dye produced by C=N and C=C bond breakage through the photoredox process.[243]

4.2.7. Other compounds. A recent work analyzes the mechanism for photocatalytic CO_2 reduction by water using (Au, Cu)/TiO_2 catalysts and FTIR spectroscopy.[244] During the adsorption process of 185 mbar CO_2 and 190 mbar of water, two bands located at 2350 and 2342 cm^{-1} were identified as a consequence of the presence of CO_2 in the gas phase. Several contributions at 1620, 1434, 1221 and 3610 cm^{-1} were observed, which are associated with bicarbonate HCO_3^- species.[244–246] The authors also assigned bands at 1589 and 1674 cm^{-1} to carboxylate $CO_2^{\bullet-}$ and carbonate CO_3^{2-} species, respectively. Under UV illumination, the single band that clearly decreased was the one at 1589 cm^{-1}, confirming $CO_2^{\bullet-}$ as the intermediate species leading to CO formation.[244]

Photocatalytic oxidation of NO under illumination has been subjected to study. Yu-Ting Cheng and coworkers analyzed the mechanism of this reaction using Cu–, V– and Cr–TiO_2 samples synthesized by a sol–gel procedure.[247] Several absorption bands were formed upon bringing TiO_2 into contact with gaseous NO. The most intense bands were identified at 1620 cm^{-1} corresponding to undissociated water ($\delta(H_2O)$)[246,248] and 1192 cm^{-1} ascribable to bidentate nitrite, $\nu(NO_2)$.[249] Other small bands in the 1540–1506 cm^{-1} region can also be detected and assigned to monodentate nitrate $\nu(NO_3)$.[250,251] Light excitation of the sample resulted in a rapid decrease in bidentate nitrite (1192 cm^{-1}) and an increase in monodentate and bidentate nitrates.[247] Although several authors suggest that surface superoxo species can be photogenerated,[140,252] and this species would lead to oxidation of nitrites to nitrates, no superoxo IR bands were detected due, possibility, to the corresponding short lifetime and/or difficult detection.[247] For Au–TiO_2 samples, the effect of several pretreatment variables on the reaction of nitric oxide was studied by *in situ* infrared spectroscopy.[253] On oxidized Au–TiO_2 the adsorption spectra are dominated by bridging NO adsorbates (bands at 1665 and 1641 cm^{-1}). For this catalyst, nitrogen–oxo species associated with TiO_2 were visible in the spectra. On the other hand, for the reduced Au–TiO_2 specimen, the NO adsorption is predominately molecular, dominated initially by $Au(NO)_2$

664 | *Chem. Soc. Rev.*, 2019, **48**, 637–682

This journal is © The Royal Society of Chemistry 2019

species.[252] The presence of surface nitrites and nitrates in the photo-oxidation of NO was also detected using infrared in other catalytic systems, such as BiOBr and Bi/graphene.[254,255] Concerning the NO molecule, the selective photo-reduction with ammonia was also followed by EPR using complex clay–zeolite–graphene systems. In this case $NH_2^{\bullet}$ type radicals were detected and assumed to be responsible for the attack on the NO molecule. The intermediate formed will evolve generating N_2 (and water) by interaction with hydroxyl-type species.[256]

Very few mechanistic studies of nitrate photo-elimination can be found in the literature. In a work of Anderson's group,[257] concerning the simultaneous photocatalytic degradation of nitrate and oxalic acid over gold promoted titania, the authors infer that the reduction of nitrate in the presence of oxalate ions proceeds separately. The oxalate oxidation ($C_2O_4^{2-} + h^+ \rightarrow CO_2 + CO_2^{\bullet-}$) takes place on the oxide component while the nitrate reduction would be primarily occurring at the metallic component.[258] The latter leads, as well known, to a number of products such as nitrites, ammonia and nitrogen gas in dependence of the noble metal nature and physico-chemical properties.[258]

5. Spectro-kinetic studies of photocatalytic samples

In this section we will review the most salient applications concerning spectro-kinetic studies which attempt to provide quantitative insights into the mechanistic and/or kinetic aspects of photocatalytic systems. As quantitative studies are relatively scarce and typically only consider a single spectroscopic technique together with kinetic or mechanistic analyses, we will group the corresponding works by spectroscopic techniques.

As a brief mention (as no spectroscopy is involved in the corresponding works), we would consider the use of deuterated water or organic compounds and the exploitation of deuterium *vs.* hydrogen isotopic effects in the reaction rate as a robust method to investigate photocatalytic mechanisms. Some works use ^{18}O labelled solid oxides such as titania to show the significance of the Mars–van Krevelen type mechanism in photocatalytic reactions such as the partial oxidation of cyclohexanone,[256] or the oxidation of benzene.[259] The significance of bridge oxygen atoms at the surface in such Mars–van Krevelen mechanism has been recently analyzed.[256] Also, differences in oxygen behavior at different anatase surfaces in photocatalytic (selective) oxidation of aromatic compounds such as terephthalic acid were analyzed using gas phase $^{18}O_2$. Concerning studies related to the key role of charge carrier species, the role of hydroxyl type radicals can be elucidated as the isotope effect would arise from the higher energy requirement for the formation of radicals ($HO^{\bullet}$ *vs.* $DO^{\bullet}$) because the O–D bond has a lower ground energy than the O–H bond.[260] A negligible isotopic effect is considered for reaction rate ratios of *ca.* 1.0–1.2, while values above 2 are considered significant. An early work showed a significant kinetic isotope effect in the oxidation of alcohols by hydroxyl radicals, reporting a k_H/k_D ratio of 2.1 for

$CH_3OH(CD_3OH)$ and a k_H/k_D ratio of 2.0 for $(CH_3)_2CHOH$ and $(CH_3)_2CDOH$ oxidation. A larger k_H/k_D of 2.35 was measured for the photodegradation of RodamineB with anatase powders.[261] Significant values for k_H/k_D of 1.9 and 2.3 for the photocatalytic CCl_4 dechlorination with, respectively, $CH_3OH(CD_3OH)$ and $(CH_3)_2CHOH((CD_3)_2CDOD)$ as hole scavengers at pH 11 when the rate-limiting contribution from the hole scavenging by methanol or isopropanol is analyzed.[262] Similarly, the H_2O/D_2O isotopic effect for isopropanol photo-oxidation was neatly observed with a k_H/k_D ratio of 2.78.[263] In the case of the reduction of CO_2 with water, the C–O bond breaking appears involved in the kinetically significant step.[264] Finally, we can mention a qualitative study of the photo-reforming of methanol in gas phase medium with $Pt:TiO_2$ indicating through the labelled water molecules resulting from the reaction that a hydroxyl radical mediated mechanism operates for low methanol content of the reactive mixture while the direct hole radical mechanism may dominate for high methanol content. An additional water assisted pathway operating far from the metal–support interface works through a bare hole attack. The different mechanisms can have an impact on the production of the different carbon containing products of the reaction and thus in the hydrogen yield.[265]

Focusing on spectroscopy and starting with EPR, we have reviewed in Section 4 the studies analyzing the radical species with significance in mechanistic and kinetic studies. By far, quantitative studies have considered hydroxyl type radicals as the principal radical species involved in key step(s) of photocatalytic processes. An early work analyzed the photodegradation of 2-chlorophenol by a single phase anatase material.[266] It provides a kinetic analysis assuming Langmuir–Hinshelwood competitive adsorption of the pollutant and water (but not of oxygen, as usual) and assumes equal concentration of holes and electrons but did not include explicitly the light effect in any of the sides (spectroscopy or kinetics) of the study. Spectroscopy was mostly used to support that hydroxyl radicals are the key species involved in the degradation. A similar approach from the point of view of spectroscopy but using a more complex kinetic scheme was utilized to elucidate the partial oxidation of benzyl alcohol with ferric ions in water as a photocatalyst.[267] The measurement of the hydroxyl-type radical rate generated by oxide (Cu, Zn) or metal (Ag) promoted anatase samples under reaction was also able to point out the involvement of such radical species in the inactivation of microorganisms such as *Escherichia coli* and *Streptococcus aureus*.[29] Another EPR of interest analyzed the photodegradation mechanism of *N,N*-diethyl-*m*-toluamide in aqueous TiO_2 suspensions under simulated solar light, indicating again the importance of hydroxyl-type radicals in the initial steps of the degradation pathway.[268]

A more quantitative approach using EPR was utilized to studying the photo-degradation of acetaldehyde in the liquid phase using visible light illumination (Fig. 17A).[120] The highest photocatalytic activity in the suspension system was obtained for a Fe(III)-deposited Ru-doped TiO_2 (Fe(III)/Ru:TiO_2) catalyst, whose main steps of the reaction mechanism are schematically
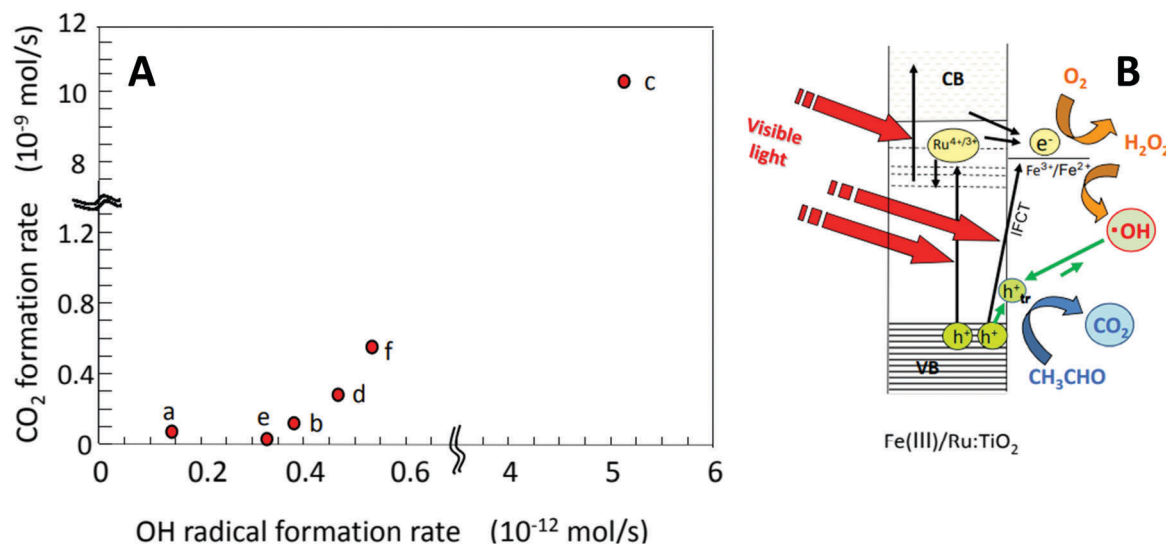
This journal is © The Royal Society of Chemistry 2019

Chem. Soc. Rev., 2019, **48**, 637–682 | **665**

Fig. 17   (A) Relationship between the formation rates of CO_2 and $^\bullet OH$ under the irradiation of a 470 nm LED. The CO_2 formation rate is a measure of the photocatalytic reaction rate in the acetaldehyde decomposition in an aqueous suspension system; (B) schematic illustration of the reaction mechanism of a Fe(III)-grafted Ru-doped TiO_2 photocatalyst based on the detection of $^\bullet OH$ and CO_2. Key: IFCT, interfacial charge transfer; h + tr, surface trapped hole. Adapted with permission from ref. 120. Copyright 2013, American Chemical Society.

shown in Fig. 17B. On the basis of the EPR and chemiluminescence experiments, the conduction band electrons were considered to be involved in a two-step excitation by visible light irradiation where O_2 is reduced to H_2O_2 as the first step. The grafted Fe(III) is reduced by Ru(III) or by interfacial charge transfer (IFCT) and then the formed Fe(II) species produce, as the second step of the mechanism, $HO^\bullet$ from H_2O_2. The $HO^\bullet$ produced in solution is adsorbed on the TiO_2 surface to form trapped holes which would oxidize organic compounds, such as acetaldehyde, leading to CO_2. According to Fig. 17 a linear relationship is observed between these two physical magnitudes; the carbon dioxide formation rate and the formation of hydroxyl radicals. The hole chain of radical species $O_2^{\bullet-}$, H_2O_2, $HO^\bullet$ was thus pointed out as kinetically relevant for a complex Fe(III)/Ru:TiO_2 catalyst as well as the corresponding single and binary parent systems.

Another study where a quantitative use of the EPR spectroscopy allowed obtaining significant mechanistic information concerns the photocatalytic reforming of biomass to generate hydrogen using Sn-grafted Ru:TiO_2 catalysts (Fig. 18).[269] Although the study also uses infrared spectroscopy, the most important conclusions related to this article are based on EPR data. Under UV illumination, the study was able to follow the generation of hydroxyl, superoxide, and hydroxymethyl ($^\bullet CH_2OH$) radical species. Fig. 18 shows the corresponding EPR signals for these three radical species (panels A and B) as well as the measurement of the EPR intensity of the $^\bullet CH_2OH$ radical species for several samples together with the corresponding hydrogen generation rates (panel C). From such data, panel D shows the linear, somewhat scattered relationship between the two observables presented in panel C. This demonstrates that the hydroxyl attack on the methanol molecule, which can be generalized to other alcohol and biomass derived molecules, renders a radical species kinetically relevant in the photo-reforming of biomass. This strongly indicates that the mechanism is a hole radical mediated

one in water rich biomass:water mixtures. This agrees with the conclusions of the mechanism extracted from isotopic effects using deuterated water for a gas phase process using methanol as a sacrificial agent.[265]

Although the previous studies make an effort in quantifying spectroscopic and/or kinetic observables, they nevertheless did not consider explicitly the inclusion of light either in the spectroscopic results and/or the kinetic analyses carried out. In Section 3 we presented the main guidelines to do it in kinetic observables and Table 4 summarizes the main kinetic equations to account explicitly for the light effect in reaction rates, allowing thus the corresponding kinetic analyses as a function of typical experimental variables, i.e. light intensity, oxygen and organic molecule content of the reaction mixture, and absorption thickness (typically catalyst concentration in liquid phase or catalyst film thickness in liquid or gas phase, respectively).

To work out the corresponding theoretical framework for EPR we concentrate on the evaluation of the radical species, carried out in the literature for hydroxyl-type radicals. As for the main radical species this is carried out in a EPR liquid cell with the help of probe molecules, we carried out the formalism for the liquid phase. In particular, the rate of hydroxyl-radical formation in an experiment (here an EPR experiment) is calculated according to the "hole trap" step presented in Table 2.

$$r_{OH^\bullet} = k_2[H_2O]_{ads}[h^+] \tag{126}$$

where the hole concentration can be approximated by eqn (81), leading to:

$$\alpha_{EPR} = \frac{r_{OH^\bullet}}{\sqrt{e_\lambda^{a,v}}} = \sqrt{\frac{\bar{\phi}}{k_3}} k_2[H_2O]_{ads} \tag{127}$$

Using $r_g = \bar{\phi} \sum_\lambda e_\lambda^{a,v}$ (for catalyst suspension in liquid phase) or $r_g = \bar{\phi} \sum_\lambda e_\lambda^{a,s}$ (for catalyst film in liquid or gas phase).
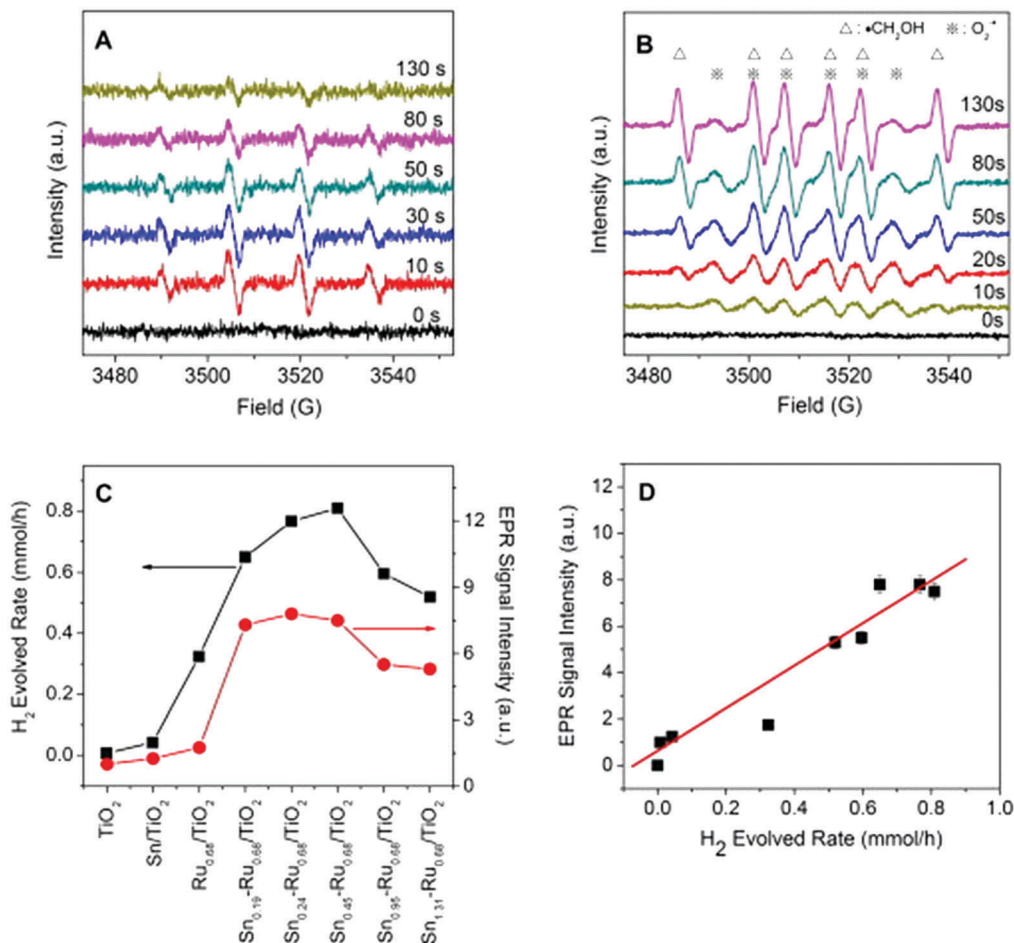
Fig. 18 (A) The changes in EPR signal of the DMPO–•OH spin adducts in the suspension of $Sn_{0.24}$–$Ru_{0.68}$/TiO_2 with different irradiation times. (B) The EPR spectra of $Sn_{0.24}$–$Ru_{0.68}$/TiO_2 dispersed in DMPO/methanol with 365 nm light irradiation. (C) The intensity of the DMPO–•CH_2OH signals and H_2 evolution rate from methanol/water solution over different photocatalysts. (D) The relationship between the intensity of the DMPO–•CH_2OH signals and photocatalytic activities of H_2 production from methanol/water solutions over different samples. The abscissa and ordinate values represent the H_2 evolution rates from methanol/water solution and intensity of the DMPO–•CH_2OH signal over a sample, respectively. Reproduced with permission from ref. 269. Copyright 2013, with permission from Elsevier Ltd.

The last equation indicates that the normalized rate of hydroxyl-radical production measured a combination of two kinetics constants $k_2/(k_3)^{1/2}$ multiplied by a factor. The first kinetic constant governs the creation of a hydroxyl-type radical while the second commands its annihilation process (Table 2). Thus its ratio renders information about the availability of hydroxyl radical species during the reaction. Note that the spectroscopic experimental signal must be normalized considering the optical properties of the catalyst suspension or film used in the reaction. Otherwise the results comparing different reaction media (as catalyst concentration in liquid phase or film thickness in gas phase) or different catalysts may lack consistency.

To prove the constancy of the factor excluding kinetic constants in eqn (127), a kinetic analysis of the photocatalytic reaction can be carried out in parallel to the EPR analysis. Using the approach summarized in eqn (83) and (84) we can measure:

$$\alpha_k = \frac{\beta_1}{\beta_2 K_3} = \sqrt{\frac{\bar{\phi}}{k_3}} k_2 [\text{Sites}] \qquad (128)$$

where K_3 is the adsorption constant of water. Eqn (128) presents the same analytic dependence of the two kinetic constants already discussed, but now multiplied by another factor. Note that the primary quantum yield is present in both eqn (127) and (128) but can be a constant for a number of cases as for example the analysis of catalysts obtained from an initially crystalline material subjected to further thermal/chemical treatment or composite catalysts where the main absorber of radiation is the same, typically titania-based composite materials in contact with other oxide(s), metal(s), sulphide(s), *etc.* In such cases, it can be eliminated from the analysis.

Confronting thus the α_{EPR} (eqn (127)) and α_k (eqn (128)) factors, valuable information about the kinetically relevant species can be obtained, contrasting at the same time the results using two experimentally independent procedures. The graphical analysis is similar to those previously reported in this Section 5, Fig. 17 and 18, plotting in this particular case the α_{EPR} and α_k factors *versus* the reaction rate.

Fig. 19 illustrates the main outcomes expected from the analysis for four possible situations. This is carried out in the

This journal is © The Royal Society of Chemistry 2019

Chem. Soc. Rev., 2019, **48**, 637–682 | **667**
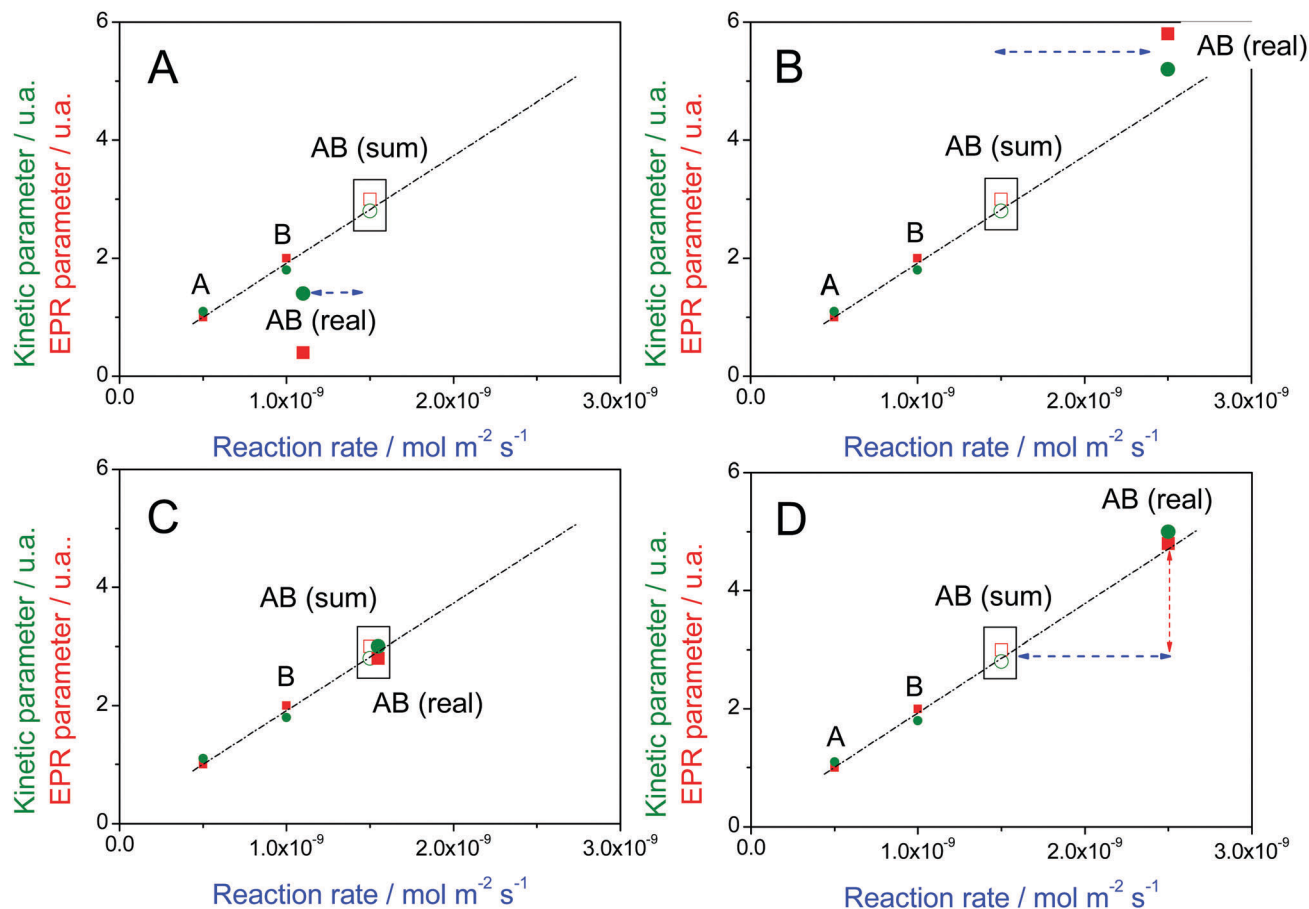
Fig. 19 Potential results from the spectro-kinetic approach using EPR as the main tool. The figure plots the EPR and kinetic parameters described in eqn (127) and (128) *vs.* the (gas phase) reaction rate of the catalysts corresponding to the two components (A or B) of the composite AB catalyst as well as the theoretical value corresponding to arithmetic, simple addition of the parent components (described in the figure as AB(sum)). The latter is marked with a square box. Red color: EPR observables; green color: kinetic observables.

example presented considering a composite AB system with chemically different components A and B, typically a titania-based composite with a second component which can have any chemical nature, such as oxides, metals, sulphides, nitrides, phosphates, *etc.*

In Fig. 19 a straight line connecting A and B parent systems describes the expected results if the mechanism has a kinetically relevant step with participation of hydroxyl-type radical species. If the AB system experimental observables are out of such a straight line, the premise of the hydroxyl radical as a kinetically relevant species does not hold. Panel A of Fig. 19 would thus indicate the nonphysical background of the hydroxyl-mediated mechanism as well as a detrimental interaction between the parent components in relation to the net production (relationship between the two kinetic constants) of the mentioned radical. The activity of the AB systems compared with the sum of those of the parent A and B systems (measured by the blue line in the figure panels) can be superior (positive) or inferior (negative) but such a point does not affect the conclusions concerning the reaction mechanism. Panel B would indicate a positive enhancement in radical formation but with unknown or non-predicted kinetic consequences. Again the

position of the blue line above or below the additive AB (theoretical) result does not affect the conclusions about the mechanism.

Two solutions confirming the model of a hydroxyl mediated mechanism are possible. The first, panel C of Fig. 19, indicates an additive effect in both the observables measuring the net hydroxyl radical formation and the reaction rate. Contrarily, in panel D of Fig. 19 we can observe that the hydroxyl-type radical increment is directly associated with the increment of the reaction rate, confirming the model for a synergistic interaction between components A and B in the AB material. According to panel D of Fig. 19, a detrimental interaction between the A and B parent systems would be possible and must be reflected in the corresponding decrease of the rate of the hydroxyl-type radical formation. Note that the interaction of components is quantitatively analyzed in Fig. 19 (and is graphically illustrated in the specific case of panel D with blue and red lines) providing further input for the kinetic analysis.

The application of this methodology is illustrated in Fig. 20 for binary titania–ceria and quaternary MnO$_x$–carbon nitride/titania–ceria composites in the photo-oxidation of toluene and acetaldehyde. With the binary titania–ceria composite the
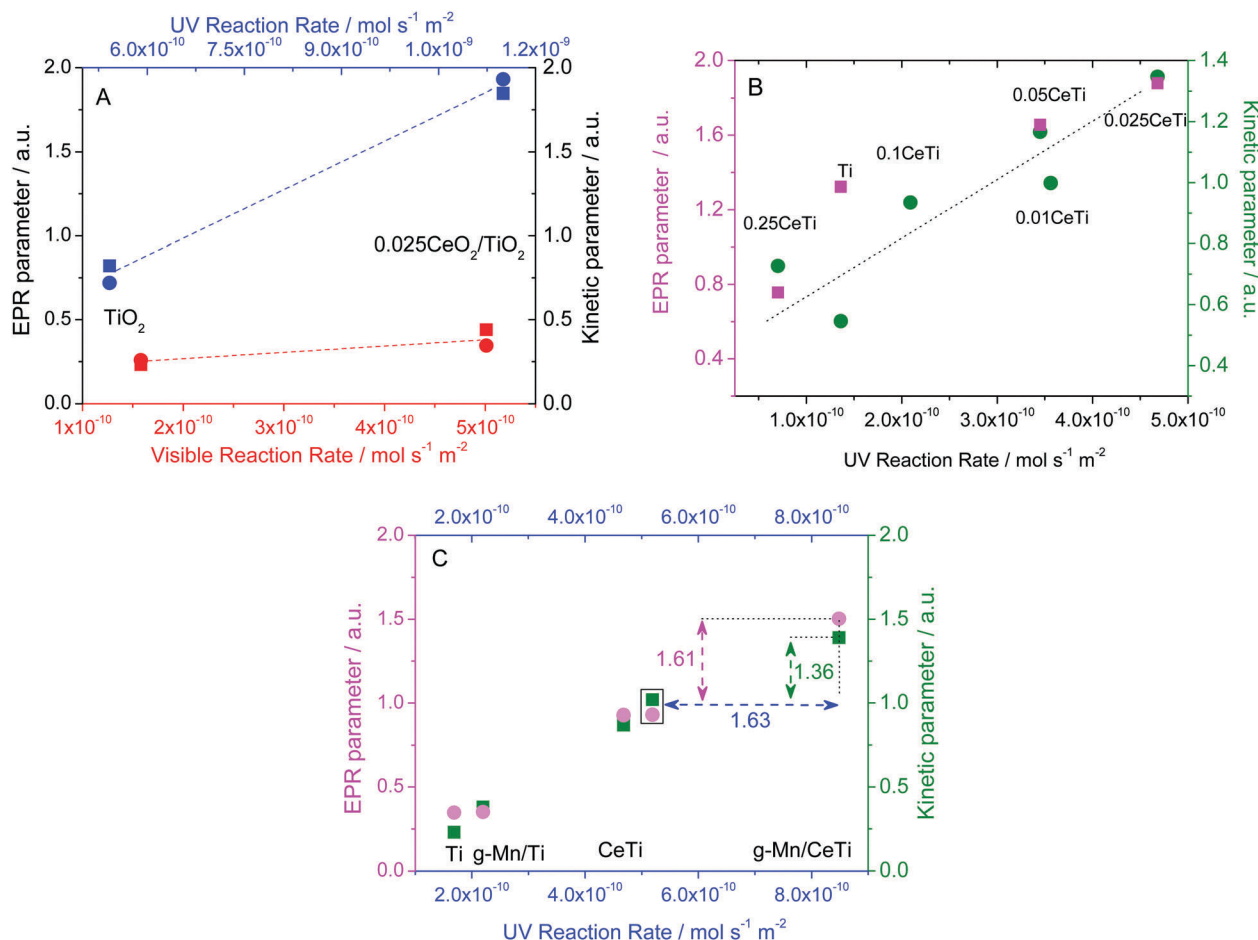
Fig. 20 (A) Correlation plot of the normalized kinetic parameter ratio (squares) and the EPR normalized rate of hydroxyl-type radical formation (circles) *vs.* the reaction rate for acetaldehyde degradation using a pure anatase (Ti) sample and a titania–ceria composite (0.025 mol% ceria; 0.025CeTi) sample. Blue: UV irradiation. Red: visible irradiation. Reproduced with permission from ref. 67. Copyright 2014, Royal Society of Chemistry. (B) Correlation plot of the normalized kinetic parameter ratio (squares; olive color) and the EPR normalized rate of hydroxyl-type radical formation (circles; magenta color) *vs.* the reaction rate for toluene degradation using a pure anatase (Ti) sample and a titania–ceria composite (xCeTi) sample. Reproduced with permission from ref. 270. Copyright 2013, American Chemical Society. (C) Correlation plot of the normalized kinetic parameter ratio (squares; olive color) and the EPR normalized rate of hydroxyl-type radical formation (circles; magenta color) *vs.* the reaction rate for toluene degradation using a pure anatase (Ti) sample, titania–ceria (CeTi), Mn:carbon nitride–titania (g-Mn/Ti), and Mn:carbon nitride–ceria–titania (g-Mn/CeTi) composite samples. Reproduced with permission from ref. 271. Copyright 2013, American Chemical Society.

analysis was used to investigate the photo-oxidation of acetaldehyde[67] and toluene.[270] In both cases, panels A and B of Fig. 20 provide strong evidence of the kinetic relevance of the hydroxyl-type radical species. Interestingly, this occurs under UV but also visible illumination, indicating the general validity of a hydroxyl-mediated mechanism for such photo-oxidation reactions with sunlight illumination. The method has been applied to more complex, quaternary systems.[271] In this case, two components of the quaternary system have their own surface "promoter" and, in fact, are composite, binary systems. Titania was promoted by ceria and carbon nitride with manganese oxide. The contact between the two binary systems leads to the quaternary one. Measuring the additive effect in a quaternary system requires the measurement of the observables in the single component catalyst(s). Once this is carried out, panel C in Fig. 20 again demonstrates the kinetic significance of the hydroxyl-radical. As mentioned previously,

the enhancement of the reaction rate is quantitatively accounted for by the corresponding enhancement of the normalized net production of hydroxyl-radicals. Note that, as explained in the contribution, the numerical error in some of the calculations makes the EPR parameter more predictive than the kinetic one. Interestingly, although spectro-kinetic studies using EPR (and optical techniques) are vastly focused on hole-related mechanisms, both hole and electron mechanisms can be analyzed with the technique.

Similarly to Table 2, Table 8 collects the elemental steps for hydroxyl and superoxide radical (with and without stable intermediates) mechanisms, those for a mechanism having the two radical species as kinetically relevant, or for a mechanism based on hydroxyl radicals obtained using exclusively electrons as charge carrier species. These mechanisms cover a number of radical mediated mechanisms of significance in oxides such as titania or zinc oxide but also for other systems

Table 8 Compilation of different radical mediated photocatalytic mechanisms

	Reaction step	Const.
Common steps	Activation	
	Photocatalyst + $h\nu \rightarrow h^+ + e^-$	
	Adsorption	
	Site + X $\leftrightarrow$ X_{ads}	K_1
	Site + Y_i $\leftrightarrow$ $Y_{i,ads}$	$K_{2,i}$
	Site + H_2O $\leftrightarrow$ H_2O_{ads}	K_3
	$Site_{O_2}$ + O_2 $\leftrightarrow$ $O_{2,ads}$	K_4
	Site + H_2O_2 $\leftrightarrow$ $H_2O_{2,ads}$	K_5
	Electron capture	
	$O_{2,ads}$ + e^- $\rightarrow$ $O_2^{\bullet-}$	k_1
	Hole trap	
	h^+ + H_2O_{ads} $\rightarrow$ $OH^\bullet$ + H^+	k_2
	Recombination	
	h^+ + e^- $\rightarrow$ heat	k_3
	Oxidation	
Hydroxyl radical attack	X_{ads} + $OH^\bullet$ $\rightarrow$ Y_{ads}	k_4
Hydroxyl radical attack Stable intermediates	X_{ads} + $OH^\bullet$ $\rightarrow$ Y_{ads}	k_4
	$Y_{i,ads}$ + $OH^\bullet$ $\rightarrow$ $Z_{i,ads}$	k_5
Superoxide radical attack	X_{ads} + $O_2^{\bullet-}$ $\rightarrow$ Y_{ads}	k_6
Superoxide radical attack Stable intermediates	X_{ads} + $O_2^{\bullet-}$ $\rightarrow$ Y_{ads}	k_6
	$Y_{i,ads}$ + $O_2^{\bullet-}$ $\rightarrow$ $Z_{i,ads}$	k_7
Hydroxyl and superoxide radical attack (parallel radical generation)	X_{ads} + $OH^\bullet$ $\rightarrow$ Y_{ads}	k_4
	X_{ads} + $O_2^{\bullet-}$ $\rightarrow$ Y_{ads}	k_6
Hydroxyl and superoxide radical attack (generation of $OH^\bullet$ from $O_2^{\bullet-}$)	$O_2^{\bullet-}$ + e^- + $2H^+$ $\rightarrow$ H_2O_2	k_8
	H_2O_2 + e^- $\rightarrow$ $OH^\bullet$ + OH^-	k_9
	X_{ads} + $OH^\bullet$ $\rightarrow$ Y_{ads}	k_4
	X_{ads} + $O_2^{\bullet-}$ $\rightarrow$ Y_{ads}	k_6
Common steps	Termination of radicals	
	$OH^\bullet$ + M $\rightarrow$ Products	k_{10}
	$O_2^{\bullet-}$ + M $\rightarrow$ Products	k_{11}

such as carbon nitride where direct formation of hole and hydroxyl species may not be involved in several photo-catalytic reactions for energetic reasons. Electron related mechanisms are, on the other hand, of obvious importance in CO_2 and other reduction reactions.[1,105] Table 9 shows the corresponding formula or kinetic expression of the reaction rate for the disappearance of the reactant and the kinetic constants used in such a formula. This table is similar to Table 4 but using a formalism that allows a direct comparison with spectroscopic observables (described in Section 4).

Table 9 also includes the kinetic parameters summarizing the experimental information available from EPR. Note that the kinetic parameters are obtained from measurements of the formation rate of hydroxyl, superoxide or both radicals. Eqn (127) and (128) exemplify the procedure for quantifying the EPR kinetic parameters for the hydroxyl-type mechanism. Of course, any measurement (EPR or any other technique) of such formation rates would hold the same equations. The information collected in Table 9 provides evidence that all the mechanisms displayed in Table 8 allow an analysis based on a spectro-kinetic approach and, thus, the experimental elucidation of the radical species involved in kinetically relevant steps.

Focusing on the IR-based analyses of relevant kinetic data, a first point to highlight is the absence of studies considering explicit inclusion of light on the kinetic schemes applied to extract information from the experimental observables. Of course, the experimental information extracted from IR is not always related to a light effect in an explicit way as, for example, those described in Table 4 or Table 9. This will be further discussed in the next section as a requirement for future studies. Nevertheless, some studies concerning gas or liquid phase photocatalytic reactions can be highlighted. The role of adsorbed water in surface coordination, adsorption kinetics, and reaction products during gas-phase formic acid photodegradation was examined in the contribution of Grassian et al.[203] Operando infrared in combination with steady state isotopic transient kinetic analysis for air purification in the presence of methanol by photocatalysis has also been reported by Thibault-Starzyk et al.[191,192] In another IR-kinetic study, Coronado et al. analysed the photooxidation of acetone and methyl isobutyl ketone. Both molecules were kinetically modelled using the Langmuir–Hinselwood–Hougen–Watson kinetic expressions.[272]

Infrared studies using an ATR cell for liquid phase systems appear as another common set-up to study photocatalytic reactions. This approach has been used in the analysis of cyclohexane deuterated cyclohexane. The results showed no kinetic isotope effect, suggesting that the reaction is not limited by the activation of cyclohexane but rather by the activation of oxygen.[180] The sequential FTIR-ATR-kinetic analysis of the photocatalytic oxidation of oxalic acid adsorbed onto TiO_2 demonstrates that the most stable species is also the most photo-labile one, and that the surface speciation is determined by a fast surface redistribution among three (oxalic acid related) species, without equilibration with the bulk solution. In this way, zero-order kinetics is observed at high degrees of coverage during the disappearance of the least stable species.[273] Also with a ATR-FT-IR tool and using vanadia-based photocatalysts during cyclohexene photo-oxidation, it has been demonstrated that the restoration of the vanadyl environment could be kinetically correlated with the rate of formation of cyclohexanone. This fact is explained by the molecular rearrangement and dissociation occurring by the attack of peroxide species on ketone (plus water) moities.[274]

Besides methanol (relevant cases already described in Section 4 of the review), 2-propanol has been widely studied and can be considered a case study from infrared studies. In a manuscript published in 2003,[275] the kinetic behavior of 2-propanol photo-oxidation has been analyzed (Fig. 21). The figure highlights the presence of CO_2 (2400–2250 cm^{-1}), acetone and mesityl oxide (1880–1620 cm^{-1}) as principal products of the reaction, observed in addition to 2-propanol (1000–880 cm^{-1}). The kinetic plot (panel A) shows clearly that acetone and CO_2 are the main stable intermediates/products of this reaction. Apart from this obvious information, according to the author's analysis, the formation of CO_2 seems to proceed in two different stages: (1) before and (2) after the complete conversion of 2-propanol to acetone. This differs from a consecutive reaction of A to B and then to C, in which the formation

670 | Chem. Soc. Rev., 2019, 48, 637–682

This journal is © The Royal Society of Chemistry 2019

Table 9 Kinetic equation and constants and EPR measurable parameters

Mechanism type	Kinetic equation		Kinetic constants		Kinetic parameters. measurable with EPR	
Hydroxyl radical attack	$r_X = -\dfrac{\alpha_1[X][H_2O]}{(1+K_3[H_2O]+K_1[X])(1+K_3[H_2O]+K_1[X]+\alpha_2[X])}\sqrt{e^{a,s}}$	(129)	$\alpha_1 = \dfrac{k_6K_1[\text{Sites}_T]^2k_2K_3}{k_{10}M}\sqrt{\dfrac{\bar\phi}{k_3}}$	(130)	$\alpha_k = k_2K_3[\text{Site}_T]\sqrt{\dfrac{\bar\phi}{k_3}}$	(132)
			$\alpha_2 = \dfrac{k_4K_1[\text{Sites}_T]}{k_{10}M}$	(131)		
Hydroxyl radical attack	$r_X = -\dfrac{\alpha_1[X][H_2O]}{(1+K_1[X]+K_3[H_2O]+K_{2,i}[Y_i])(1+K_1[X]+K_3[H_2O]+K_{2,i}[Y_i]+\alpha_2[X])}\sqrt{e^{a,s}}$	(133)	$\alpha_1 = \dfrac{k_4K_1[\text{Sites}_T]^2k_2K_3}{k_{10}M}\sqrt{\dfrac{\bar\phi}{k_3}}$	(135)	$\alpha_{k,1} = k_2K_3[\text{Sites}_T]\sqrt{\dfrac{\bar\phi}{k_3}}$	(139)
Stable intermediates	$r_Y = \left(\dfrac{\alpha_1[X][H_2O]-\alpha_4[Y_i][H_2O]}{(1+K_1[X]+K_3[H_2O]+K_{2,i}[Y_i])(1+K_1[X]+K_3[H_2O]+K_{2,i}[Y_i]+\alpha_2[X]+\alpha_3[Y_i])}\right)\sqrt{e^{a,s}}$	(134)	$\alpha_2 = \dfrac{k_4K_1[\text{Sites}]}{k_{10}M}$	(136)	$\alpha_{k,2} = k_2K_3[\text{Sites}_T]\sqrt{\dfrac{\bar\phi}{k_3}}$	(140)
			$\alpha_3 = \dfrac{k_5K_{2,i}[\text{Sites}]}{k_{10}M}$	(137)	$(\alpha_{k,1} = \alpha_{k,2})^*$	
			$\alpha_4 = \dfrac{k_5K_{2,i}[\text{Sites}_T]^2k_2K_3}{k_{10}M}\sqrt{\dfrac{\bar\phi}{k_3}}$	(138)		
Superoxide radical attack	$r_X = -\dfrac{\alpha_1[X][O_2]}{(1+K_4[O_2])(1+K_1[X]+\alpha_2[X])}\sqrt{e^{a,s}}$	(141)	$\alpha_1 = \dfrac{k_6K_1[S_1]k_1K_4[\text{Sites}_{O_2,T}]}{k_{11}M}\sqrt{\dfrac{\bar\phi}{k_3}}$	(142)	$\alpha_k = k_1K_4[\text{Sites}_{O_2,T}]\sqrt{\dfrac{\bar\phi}{k_3}}$	(144)
			$\alpha_2 = \dfrac{k_6K_1[\text{Sites}_T]}{k_{11}M}$	(143)		
Superoxide radical attack	$r_X = -\dfrac{\alpha_1[X][O_2]}{(1+K_4[O_2])(1+K_1[X]+K_{2,i}[Y_i]+\alpha_2[X])}\sqrt{e^{a,s}}$	(145)	$\alpha_1 = \dfrac{k_5K_1[\text{Sites}]k_1K_4[\text{Sites}_{O_2,T}]}{k_{11}M}\sqrt{\dfrac{\bar\phi}{k_3}}$	(147)	$\alpha_{k,1} = k_1K_4[\text{Sites}_{O_2,T}]\sqrt{\dfrac{\bar\phi}{k_3}}$	(151)
Stable intermediates	$r_Y = \left(\dfrac{\alpha_1[X][O_2]-\alpha_4[Y_i][O_2]}{(1+K_4[O_2])(1+K_1[X]+K_{2,i}[Y_i]+\alpha_2[X]+\alpha_3[Y_i])}\right)\sqrt{e^{a,s}}$	(146)	$\alpha_2 = \dfrac{k_5K_1[\text{Sites}_T]}{k_{11}M}$	(148)	$\alpha_{k,2} = k_1K_4[\text{Sites}_{O_2,T}]\sqrt{\dfrac{\bar\phi}{k_3}}$	(152)
			$\alpha_3 = \dfrac{k_7K_{2,i}[\text{Sites}]}{k_{11}M}$	(149)	$(\alpha_{k,1} = \alpha_{k,2})^*$	
			$\alpha_4 = \dfrac{k_7K_Y[\text{Sites}_T]k_1K_4[\text{Sites}_T]}{k_{11}M}\sqrt{\dfrac{\bar\phi}{k_3}}$	(150)		
Hydroxyl and superoxide radical attack (parallel radical generation)	$r_X = -\left(\dfrac{\alpha_1C_X[H_2O]}{(1+K_3[H_2O]+K_1[X])(1+K_3[H_2O]+K_1[X]+\alpha_2[X])} + \dfrac{\alpha_1[X][O_2]}{(1+K_4[O_2])(1+K_1[X]+\alpha_2[X])}\right)\sqrt{e^{a,s}}$	(153)	$\alpha_1 = \dfrac{k_4K_1[\text{Sites}_T]^2k_2K_3}{k_{10}M}\sqrt{\dfrac{\bar\phi}{k_3}}$	(154)	$\alpha_{k,1} = k_2K_3[\text{Sites}_T]\sqrt{\dfrac{\bar\phi}{k_3}}$	(158)
			$\alpha_2 = \dfrac{k_4K_1[\text{Sites}_T]}{k_{10}M}$	(155)	$\alpha_{k,2} = k_1K_4[\text{Site}_T]\sqrt{\dfrac{\bar\phi}{k_3}}$	(159)
			$\alpha_3 = \dfrac{k_6K_1[S_1]k_1K_4[\text{Sites}]}{k_{11}M}\sqrt{\dfrac{\bar\phi}{k_3}}$	(156)		
			$\alpha_4 = \dfrac{k_6K_1[\text{Sites}_T]}{k_{11}M}$	(157)		

Table 9 (continued)

Mechanism type	Kinetic equation	Kinetic constants		Kinetic parameters. measurable with EPR	
Hydroxyl and superoxide radical attack (generation of HO$^{\bullet}$ from O$_2^{\bullet-}$)	$r_X = -\dfrac{\alpha_1[X][H_2O_2]\sqrt{e^{\mu,s}}}{(1+K_5[H_2O_2]+K_1[X])(1+K_5[H_2O_2]+K_1[X]+\alpha_2[X])}$ $+\dfrac{\alpha_3[X][O_2]\sqrt{e^{\mu,s}}}{(1+K_4[O_2])(1+K_4[O_2]+K_1[X])+\alpha_5\sqrt{e^{\mu,s}}(1+K_5[H_2O_2]+K_1[X])+(1+K_5[H_2O_2]+K_1[X])}$ (160)	$\alpha_1 = \dfrac{k_4 K_1[\text{Sites}_T]^2 k_9 K_5}{k_{10}M}\sqrt{\dfrac{\bar{\Phi}}{k_3}}$ (161) $\alpha_2 = \dfrac{k_4 K_1[\text{Sites}_T]}{k_{10}M}$ (162) $\alpha_3 = \dfrac{k_6 K_1[\text{Sites}_T]k_1 K_4[\text{Sites}_T]}{k_{11}M}\sqrt{\dfrac{\bar{\Phi}}{k_3}}$ (163) $\alpha_4 = \dfrac{k_6 K_1[\text{Sites}_T]}{k_{11}M}$ (164) $\alpha_5 = \dfrac{k_8}{k_{11}M}\sqrt{\dfrac{\bar{\Phi}}{k_3}}$ (165)		$\alpha_{k,1} = k_9 K_5[\text{Sites}_T]\sqrt{\dfrac{\bar{\Phi}}{k_3}}$ (166) $\alpha_{k,2} = k_1 K_4[\text{Sites}_T]\sqrt{\dfrac{\bar{\Phi}}{k_3}}$ (167) $\alpha_{k,3} = \dfrac{k_8}{k_{11}M}\sqrt{\dfrac{\bar{\Phi}}{k_3}}$ (168)	

of final product C should be almost linear as a function of time during the whole process (Fig. 21). In addition, the authors conclude that 2-propanol photo oxidation proceeds along two routes; one is through a chemisorbed species, *e.g.* a 2-propoxide species, and the other through the so-called H-bonded 2-propanol (undissociated molecule). The route through 2-propoxide leads to a faster and direct oxidation to CO_2, while the route involving H-bonded 2-propanol proceeds through a conversion to acetone, formate species, and finally CO_2. The oxidation rates of 2-propanol and acetone both increase as the oxygen concentration increases. The acetone decay rate during acetone photo-oxidation is much faster than that of acetone formed as an intermediate during 2-propanol photodegradation. The study also analyzes the kinetics of the acetone photo-oxidation showing a decay of acetone and mesityl oxide, formation of CO_2, and evolution of formate species as an intermediate.[276]

Another IR work proposes a microkinetic analysis with the objective to simulate the experimental data of 2-propanol photodegradation.[211] Fig. 22, selected from this work, shows the comparison between experimental and theoretical curves derived from the microkinetic study. According to the author's description, curves b1 and b2 give the evolution of the coverage of the acetone on readsorption (site s1) and diffusion process (site s2) sites, respectively, whereas curve b obtained from the sum (curve b1 + curve b2) gives the evolution of acetone coverage at the TiO_2 surface whatever the nature of the sites. Curve d provides the sum of the coverage of the adsorbed 2-propanol and acetone species. It shows that, during the photo-oxidation, the total coverage of the surface is lower than the initial coverage of the adsorbed 2-propanol species whatever the irradiation time: the progressive decrease of curve d represents the transformation of acetone into CO_2 and formate species. This spectro-kinetic study shows that photo-oxidation of 2-propanol is controlled by the strong competitive chemisorption on the active sites (s1) between the alcohol and the acetone. This competitive chemisorption limits the photodegradation process considering that acetone is the single route for the mineralization of 2-propanol.[211]

Another interesting *in situ* infrared transmission spectroscopy study in combination with kinetic analysis for acetone photodegradation was carried out by Österlund *et al.*[276] The work highlights the influence of niobium doped anatase TiO_2 made by sol–gel methods. Focusing on the kinetic analysis, the plots of $\ln(A/A_0)$ *vs.* time, t (A being the observable absorbance), are shown in Fig. 23 for different materials. The authors report an abrupt change of the curve for the TiO_2 sample above *ca.* 7 min. Additionally, the decay of the $\nu(C=O)$ and integrated $\nu(C=H)$ absorption bands for t = 10–40 min indicates the decomposition of intermediates such as μ-formate with rather similar rates. On the other hand, the Nb doped samples did not show this discernible decrease, indicating that the rate-determining step for total acetone oxidation is, for doped samples, the initial acetone decomposition step.

Acetaldehyde and azo dye photobleaching on bismuth-modified TiO_2 was analyzed by means of *in situ* FTIR spectroscopy in another study. The results show that the presence of

672 | *Chem. Soc. Rev.*, 2019, **48**, 637–682

This journal is © The Royal Society of Chemistry 2019
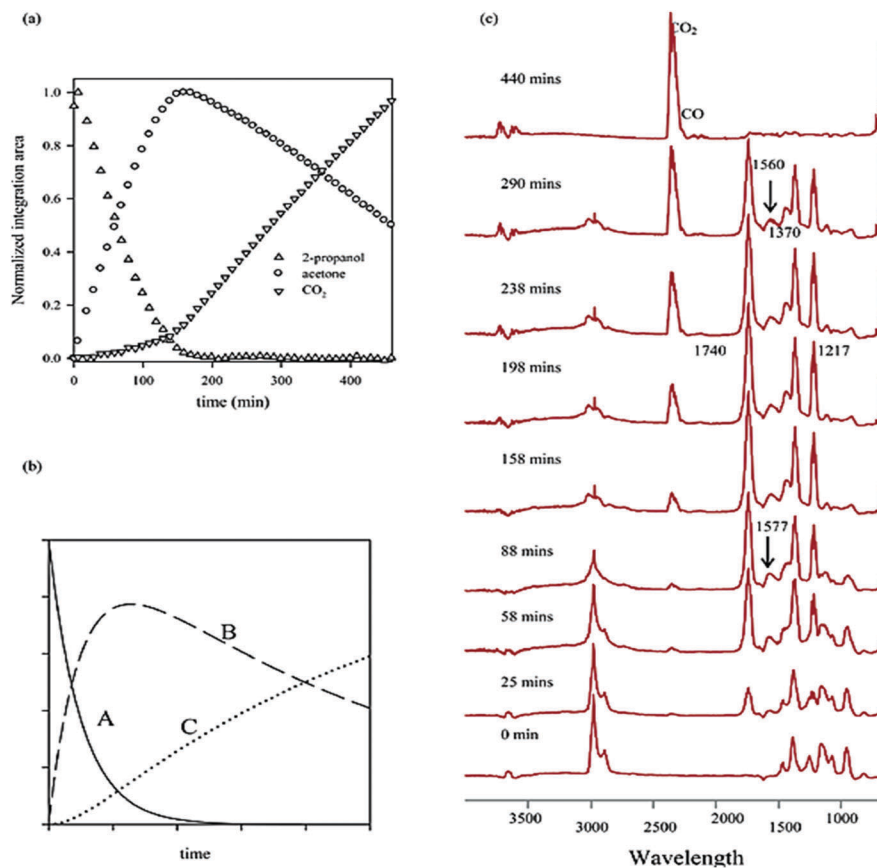
Fig. 21 Representative kinetic curve (a) for 2-propanol photo-oxidation, (b) simulated kinetic curves for the consecutive reaction $A \xrightarrow{k_1} B \xrightarrow{k_2} C$ B with $k_1/k_2 = 10$, and (c) typical spectra of 2-propanol photo-oxidation at different irradiation times using a UV lamp source. Reproduced with permission from ref. 275. Copyright 2003, with permission from the American Chemical Society.
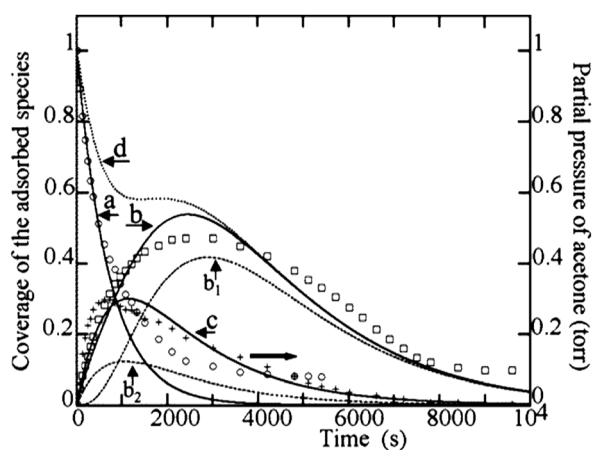
Fig. 22 Simulation of the experimental data (FTIR spectroscopy) during the static 2-propanol photodegradation considering the experimental microkinetic approach of the catalytic process. Coverages of the 2-propanol (○) and acetone (□) species; (+) partial pressure of acetone. Symbols (a) and (b) represent the modelled evolution of 2-propanol and acetone respectively; (c) modelled evolution of the partial pressure of acetone; (b1 and b2) evolution of the coverage of the s1 and s2 sites by acetone adsorbed species; (d) evolution of the coverage of the TiO_2 surface by the two adsorbed species (2-propanol and acetone). Reproduced with permission from ref. 211. Copyright 2006, American Chemical Society.
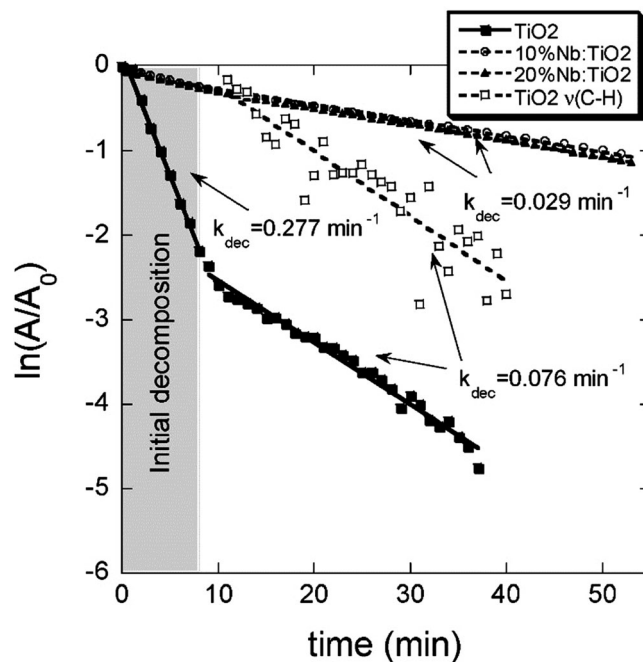
Fig. 23 Plots of the normalized logarithmic decay of the acetone $\nu(C=O)$ absorption band as a function of time. Reproduced with permission from ref. 276. Copyright 2006, with permission from the American Chemical Society.

This journal is © The Royal Society of Chemistry 2019

Chem. Soc. Rev., 2019, **48**, 637–682 | 673

bismuth alters the adsorption kinetics of acetaldehyde, resulting in different surface product(s) and a modified photocatalytic reaction pathway.[277]

Finally, we would like to underscore the spectro-kinetic analysis of the adsorption and photo-oxidation of acetaldehyde on TiO_2 and sulfate-modified TiO_2 carried out by Österlund et al.[223] The study, according to the results of the authors, supports a general reaction scheme described by eqn (169). This (simplified) scheme takes into account major reactants and intermediates (acetaldehyde, crotonaldehyde, and formate).

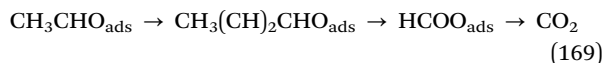$$CH_3CHO_{ads} \rightarrow CH_3(CH)_2CHO_{ads} \rightarrow HCOO_{ads} \rightarrow CO_2 \tag{169}$$

As is graphically described in panels A and B of Fig. 24, to obtain quantitative data from FTIR absorbance, a complex analysis is mandatory in this case. As the absorbance of the samples changes abruptly during UV illumination and the background level shifts with time in the FTIR spectra, the analysis procedure requires simultaneous consideration of both facts. Before the first UV illumination cycle and for certain samples, an aldol condensation decreases the intensity of several bands related to the acetaldehyde molecule and their temporal evolution was fitted considering a second order reaction. The fit was then extrapolated through the first photocatalytic cycle,

where the largest shift of the background occurs. Such an extrapolated function was subtracted from the experimental data, leaving only what the authors assume to be a rigid background shift due to the changed IR reflectivity of the sample film. Next, the up-shift related to the "rigid background" was fitted with a power-law expression. This presumes that the states generated by the initial UV excitation are sensitive to IR radiation, so that a weak and gradual drift of the background takes place throughout the IR experiment under illumination.[223]

Using the described analytical procedure and based on the reaction scheme of eqn (169), the following overall rate equations for photo-oxidation of acetaldehyde on TiO_2 (from eqn (170)–(174)) and SO_4–TiO_2 (from eqn (175)–(177)) can be obtained:

$$\frac{d\theta_A}{dt} = -k_{A \rightarrow B_1}^{UV} \theta_A^2 - k_{A \rightarrow B_2}^{UV} \theta_A^2 \tag{170}$$

$$\frac{d\theta_B}{dt} = \frac{d\theta_{B_1}}{dt} + \frac{d\theta_{B_2}}{dt} \tag{171}$$

$$\frac{d\theta_{B_1}}{dt} = \frac{1}{2} k_{A \rightarrow B_1}^{UV} \theta_A^2 (\theta_{sat} - \theta_A - \theta_B) - k_{B_1 \rightarrow C}^{UV} \theta_{B_1} - k_{B_1 \rightarrow U_1}^{UV} \theta_{B_1} \tag{172}$$
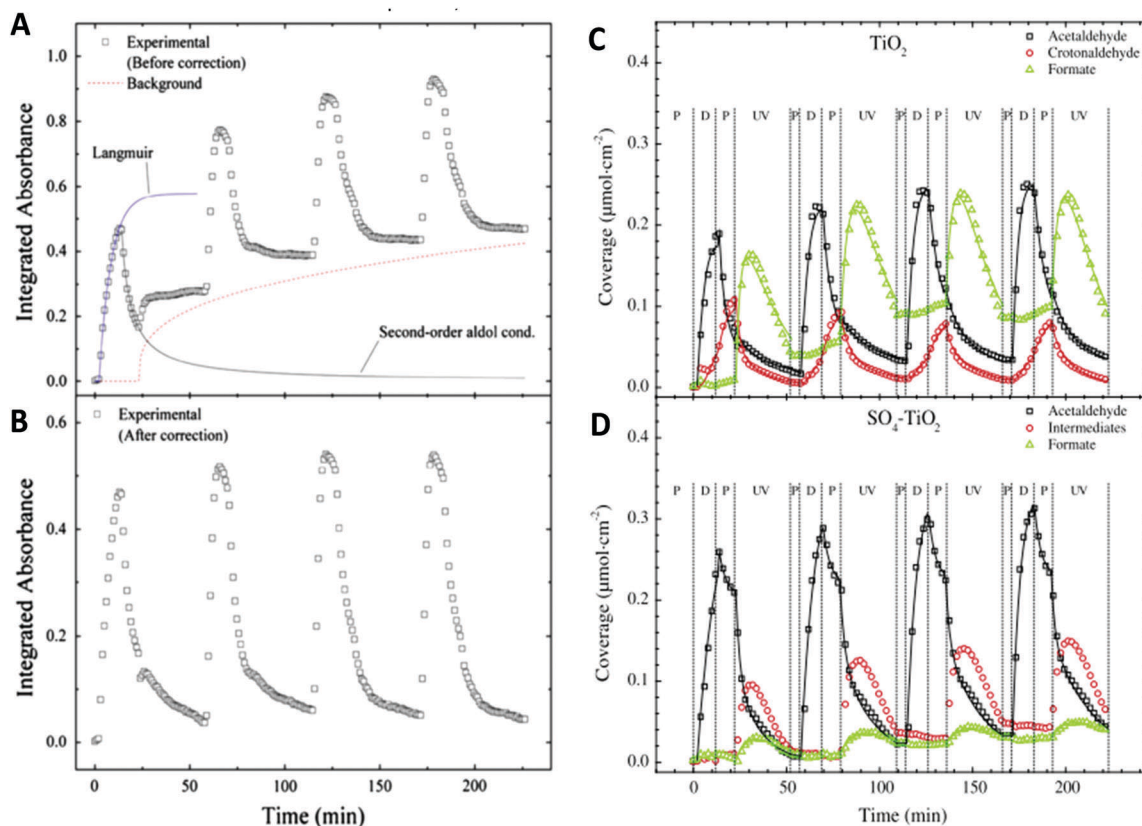
Fig. 24 Integrated FTIR absorbance bands between 1680 and 1708 cm^{-1} for acetaldehyde on a TiO_2 surface without (panel A) and with (panel B) baseline corrections. Surface coverage of adsorbed acetaldehyde, crotonaldehyde, and formate as a function of reaction time during four consecutive cycles of acetaldehyde gas dosing (D), purging in synthetic air (P), and UV irradiation (UV), respectively, on (panel C) TiO_2, and (panel D) SO_4–TiO_2 films. Solid curves represent results from the micro-kinetic modeling. Reproduced with permission from ref. 223. Copyright 2013, with permission from Elsevier Ltd.

674 | Chem. Soc. Rev., 2019, 48, 637–682

This journal is © The Royal Society of Chemistry 2019

$$\frac{d\theta_{B_2}}{dt} = \frac{1}{2}k_{A\to B_2}^{UV}\theta_A{}^2(\theta_{sat} - \theta_A - \theta_B) - k_{B_2\to C}^{UV}\theta_{B_2} - k_{B_2\to U_2}^{UV}\theta_{B_2}$$

(173)

$$\frac{d\theta_C}{dt} = 4\left(k_{B_1\to C}^{UV}\theta_{B_1} + k_{B_2\to C}^{UV}\theta_{B_2}\right) - k_C^{UV}\theta_C$$ (174)

$$\frac{d\theta_{A_1}}{dt} = -k_{A_1\to C}^{UV}\theta_{A_1} - k_{A_1}^{des}\theta_{A_1} - k_{A_1\to U}^{UV}\theta_{A_1}$$ (175)

$$\frac{d\theta_{A_2}}{dt} = k_{A_2\to C}^{UV}\theta_{A_2} - k_{A_2}^{des}\theta_{A_2} - k_{A_2\to U}^{UV}\theta_{A_2}$$ (176)

$$\frac{d\theta_C}{dt} = 2\left(k_{A_2\to C}^{UV}\theta_{A_2} + k_{A_2\to C}^{UV}\theta_{A_2}\right) - k_C^{UV}\theta_C$$ (177)

In previous equations, A represents acetaldehyde, B crotonaldehyde, and C is formate. In the modeling work, the experimental data for the crotonaldehyde decomposition are simulated with two sets, corresponding to the fast and slow reactions (eqn (172) and (173)). The $k_{X\to U}^{UV}$ (X = A, B$_1$, B$_2$) constants represent reaction pathways leading to some unknown intermediate products. For SO$_4$–TiO$_2$ equations, k_A^{des} describes the desorption rate of acetaldehyde.

Using the TiO$_2$ sample (eqn (170)–(174)), the authors describe as the first step of the general scheme (eqn (169)) the aldol condensation to obtain crotonaldehyde (eqn (170)). The kinetic modelling considers that the adsorption is limited by the number of available sites and the aldol condensation reaction displayed, as mentioned, second-order kinetics and takes place only during the purging period. Besides, under UV irradiation, the reaction scheme assumes that crotonaldehyde is first oxidized by radical attack at the C–C bond and then subsequent oxidation occurs following two parallel pathways (two active centers; eqn (172) and (173)) with different reaction rates, both *via* formate, unknown intermediates, and subsequently ending in CO$_2$ and water.

The SO$_4$–TiO$_2$ equations were obtained following a similar analysis. In this case, two reaction pathways were identified (eqn (175) and (177)). The first one described acetaldehyde adsorption and conversion to formate and the other one a parallel reaction of acetaldehyde to an unidentified surface species (1656 cm^{-1}). The work also reports, in contrast to the TiO$_2$ case, no evidence for aldol condensation before UV irradiation. The final eqn (175)–(177) were obtained considering that desorption of acetaldehyde takes place and two photoreaction rate constants corresponding to a fast and a slow reaction pathway. Using this reaction scheme, weighting factors were fitted in order to determine the extent to which each of the reactions affected the total observed rate.

Panels C and D of Fig. 24 display experimental and simulated cycling results as a function of time for both samples. D, P and UV symbols represent gas dosing, purging in synthetic air, and UV irradiation steps, respectively. From a comparison of TiO$_2$ and SO$_4$–TiO$_2$ kinetic results, the authors propose an explanation for the selectivity modification and the modification of the photoactivity (rate) occurring in the presence of sulphur-containing surface species. The modelling describes the spontaneous crotonaldehyde formation on TiO$_2$ at room temperature, which is not the case on SO$_4$–TiO$_2$ due to interactions with surface sulfate groups. In addition, bonding of aldehyde and carboxylate species is weakened on SO$_4$–TiO$_2$, and the formation rate of intermediate formate products is lowered compared to the corresponding rate for TiO$_2$. This leads to conclude that fast and slow photo-oxidation reactions can occur on both samples, the ratio between the fast and slow reaction rates being much larger for TiO$_2$ than for SO$_4$–TiO$_2$. The presence of sulphur at the titania surface would thus have a positive catalytic role mostly focusing on enhancing the adsorption of reactants and reducing poisoning effects, rather than promoting the typical intermediates of the reaction. This makes a most stable material and enhances long term activity.[223]

Finally, we can mention a single example concerning the use of *in situ* surface enhanced Raman scattering to follow the photo-degradation of *p*-aminothiophenol using titania and visible light and using a spectro-kinetic approach. The study of the appearance or disappearance rates of specific Raman signals demonstrates that the photo-degradation of the above mentioned molecule occurs with formation of azo compounds as stable intermediates.[278] There is also a single NMR contribution analyzing the photo-reforming of methanol on Pt supported on titania nanotubes. The work concludes, as was previously described here using other techniques, that methanol suffers a hole attack in a reaction where water plays an active role and that the protons generated from the hole attack form hydrogen at noble metal particle surfaces.[279]

6. Conclusions and outlook into the future

The use of light as the energy source of catalytic processes complicates the obtaining of information to clarify kinetic and mechanistic aspects of chemical processes of interest in the photo-catalysis field. Classical, thermal catalysis has a key tool to unravel the corresponding experimental information. This is what we usually called the spectro-kinetic approach. In this review we provide a basic framework for setting up or at least to progress in the setting up of this approach in a practical and useful way within the photocatalytic field.

As a first step in this task, we considered the establishment of useful kinetic expression for all types of mechanism. Such formulations are summarized in Tables 2 and 8 of the review. Compact kinetic expressions for liquid and gas phase reactions are presented in Tables 5 and 6, respectively. The information compiled in such tables analyzed most common hole and electron related mechanisms and included the formation of stable intermediates to allow a direct comparison with experimental results. Note that this mechanistic and kinetic framework would thus consider not only the measurement of charge carrier species observables by EPR, chemiluminescence and other spectroscopies but also the measurement of stable intermediates and their surface concentrations by IR, Raman or other techniques. Importantly, all these mechanisms include

This journal is © The Royal Society of Chemistry 2019

Chem. Soc. Rev., 2019, **48**, 637–682 | **675**

explicitly the effect of light in contrast to typical kinetic formulations. Dismissing this point would lead to a limitation for general application and would thus not provide results transferable to other studies. This is an important point typically dismissed in literature reports and must establish quantitative spectro-kinetic correlations. General application and validity in kinetic formalisms is therefore required to further progress in the understanding of mechanistic and kinetic aspects of photo-catalytic processes.

As a side conclusion we also provide (Section 2.3.6) a clearer view for the identification of the sustained mechanisms behind simple kinetic expressions broadly used in the literature. This section would thus unveil the grounds for the physico-chemical interpretation of the results of fitting procedures using simplified schemes. It also highlights the strengths and weaknesses of these "simple" approaches.

The common belief is that most photo-catalytic mechanisms are hole related ones. This accounts for example for the majority of the photo-oxidation of pollutants or for the hydrogen photo-production from bio-molecules. Obviously, CO_2 or reduction reactions will sustain electron related mechanisms.[1,27] In any case, the physico-chemical discussion of the active radical species in hole-related mechanisms corresponds to a hot topic. It is likely that depending on the interaction of the target molecule and the specific catalyst surface nature, bare holes, surface hydroxyls and/or gas– or liquid–solid hydroxyl-related species can have a key role. Chemisorbed species are more prone to using the so-called bare holes (those corresponding to free holes in equilibrium with weak traps) while less interacting molecules will tend to be attacked by other species. The key role of the water-rich overlayer in shaping the active hole-related species has been clearly point out here by critically analyzing results from TIRFM, EPR and other techniques and they highlight the critical, fundamental role of water in the photo-catalytic mechanisms. The equilibrium or exchange between all of the above mentioned hole-related charged species is therefore obvious and would add complexity to the analysis. Without considering the exact hole-related species and from a phenomenological point of view, we provide a number of studies of the hydroxyl formation rate that show linear correlation with kinetic parameters, indicating that the common beliefe of a hydroxyl-mediated mechanism has experimental support in many occasions concerning photo-oxidation processes. Nonetheless, we must stress that other mechanisms, mostly based on electron-related charge species and described in Tables 4 and 9, would be of practical application for catalytic systems such as carbon nitride and other systems (differing from TiO_2 or ZnO) or for the above mentioned CO_2 reduction process.

The analyses of surface species by infrared and less commonly Raman spectroscopies have also been reviewed in the context of the investigation of the photo-catalytic mechanisms and kinetics. A few and rather interesting studies have been carried out but unfortunately they mostly focus on interpreting the surface species present under illumination and their evolution during the reaction. They however do not consider the explicit inclusion of light in the corresponding mechanism and

would thus need to be further improved in the near future. Embracing surface information in the mechanisms described in Tables 2 and 8 would be a task for the future. In this sense we note the "structural" parallelism in terms of the reaction rate dependence of the active charge carrier species between hole and electron related mechanisms described in Tables 2 and 8. The complex surface behavior of reaction intermediates, as exemplified in eqn (170)–(177), would thus open the "true" understanding of the differences between the main (hole and electron) charged species and their roles in the photo-catalytic performance.

So, we believe that the review highlights the up to date most exciting results in the use of spectro-kinetic tools for understanding photo-catalytic processes and sets up the theoretical framework required for their rigorous and general implementation. Possibly more important, the review would pave the pathway for the future application of spectro-kinetic concepts and tools. The building of information from several experimental techniques together with the explicit treatment of light to setting up a fully interpretable and experimentally supported photo-catalytic mechanism and its kinetic consequences appear as critical tasks for the future development of the photo-catalytic field. Such a progress is certainly a tool required to achieving an adequate level of "fundamental" understanding, similar to the one currently accessed in thermal catalytic processes.

Conflicts of interest

There are no conflicts to declare.

Acknowledgements

References

1 A. Kubacka, M. Fernández-García and G. Colón, *Chem. Rev.*, 2012, **112**, 1555–1614.

2 J. C. Colmenares and R. Luque, *Chem. Soc. Rev.*, 2014, **43**, 765–778.

3 V. Etacheri, C. Di Valentin, J. Schneider, D. Bahnemann and S. C. Pillai, *J. Photochem. Photobiol., C*, 2015, **25**, 1–29.

4 J. C. Colmenares and Y.-J. Xu, *Heterogeneous Photocatalysis From Fundamentals to Green Applications*, Springer-Verlag, Berlin Heidelberg, 2016.

5 D. Spasiano, R. Marotta, S. Malato, P. Fernandez-Ibañez and I. Di Somma, *Appl. Catal., B*, 2015, **171**, 90–123.

6 X. Chen, S. Shen, L. Guo and S. S. Mao, *Chem. Rev.*, 2010, **110**, 6503–6570.

7 D. Wang, T. Hisatomi, T. Takata, C. Pan, M. Katayama, J. Kubota and K. Domen, *Angew. Chem., Int. Ed.*, 2013, **52**, 11252–11256.

8 A. Dhakshinamoorthy, S. Navalon, A. Corma and H. Garcia, *Energy Environ. Sci.*, 2012, **5**, 9217–9233.

9 K. Li, B. Peng and T. Peng, *ACS Catal.*, 2016, **6**, 7485–7527.

10 W. Wang, G. Huang, J. C. Yu and P. K. Wong, *J. Environ. Sci.*, 2015, **34**, 232–247.

11 H. de Lasa, B. Serrano and M. Salaices, *Photocatalytic Reaction Engineering*, Springer US, Boston, MA, 2005.

12 X. Li, J. Yu and M. Jaroniec, *Chem. Soc. Rev.*, 2016, **45**, 2603–2636.

13 R. Marschall, *Adv. Funct. Mater.*, 2014, **24**, 2420.

14 S. Na Phattalung, S. Limpijumnong and J. Yu, *Appl. Catal., B*, 2017, **200**, 1–9.

15 M. Dahl, Y. Liu and Y. Yin, *Chem. Rev.*, 2014, **114**, 9853–9889.

16 K. R. Reddy, M. Hassan and V. G. Gomes, *Appl. Catal., A*, 2015, **489**, 1–16.

17 S. Bai, J. Jiang, Q. Zhang and Y. Xiong, *Chem. Soc. Rev.*, 2015, **44**, 2893–2939.

18 C. Sousa, S. Tosoni and F. Illas, *Chem. Rev.*, 2013, **113**, 4456–4495.

19 A. V. Akimov, A. J. Neukirch and O. V. Prezhdo, *Chem. Rev.*, 2013, **113**, 4496–4565.

20 T. Tachikawa and T. Majima, *Chem. Soc. Rev.*, 2010, **39**, 4802–4819.

21 M. A. Henderson, *Surf. Sci. Rep.*, 2011, **66**, 185–297.

22 B. Liu, X. Zhao, C. Terashima, A. Fujishima and K. Nakata, *Phys. Chem. Chem. Phys.*, 2014, **16**, 8751–8760.

23 A. Mills, C. O. Rourke and K. Moore, *J. Photochem. Photobiol., A*, 2015, **310**, 66–105.

24 Y. Boyjoo, H. Sun, J. Liu, V. K. Pareek and S. Wang, *Chem. Eng. J.*, 2017, **310**, 537–559.

25 A. H. Mamaghani, F. Haghighat and C.-S. Lee, *Appl. Catal., B*, 2017, **203**, 247–269.

26 V. Augugliaro, M. Bellardita, V. Loddo, G. Palmisano, L. Palmisano and S. Yurdakal, *J. Photochem. Photobiol., C*, 2012, **13**, 224–245.

27 Y. Nosaka and A. Y. Nosaka, *Chem. Rev.*, 2017, **117**, 11302–11336.

28 L. Österlund, *On Solar Hydrogen & Nanotechnology*, John Wiley & Sons, Ltd, Chichester, UK, 2010, pp. 189–238.

29 A. Kubacka, M. J. Muñoz-Batista, M. Ferrer and M. Fernández-García, *Appl. Catal., B*, 2013, **140–141**, 680–690.

30 V. Tomašić, F. Jović and Z. Gomzi, *Catal. Today*, 2008, **137**, 350–356.

31 A. Gora, B. Toepfer, V. Puddu and G. Li Puma, *Appl. Catal., B*, 2006, **65**, 1–10.

32 C. Guzmán, G. del Ángel, R. Gómez, F. Galindo-Hernández and C. Ángeles-Chavez, *Catal. Today*, 2011, **166**, 146–151.

33 H. Liu, Z. Lian, X. Ye and W. Shangguan, *Chemosphere*, 2005, **60**, 630–635.

34 M. L. Sauer and D. F. Ollis, *J. Catal.*, 1996, **158**, 570–582.

35 K.-H. Wang, H.-H. Tsai and Y.-H. Hsieh, *Appl. Catal., B*, 1998, **17**, 313–320.

36 G. Vincent, P. M. Marquaire and O. Zahraa, *J. Photochem. Photobiol., A*, 2008, **197**, 177–189.

37 X. Zhu, D. Chang, X. Li, Z. Sun, X. Deng and A. Zhu, *Chem. Eng. J.*, 2015, **279**, 897–903.

38 X.-Q. Deng, J.-L. Liu, X.-S. Li, B. Zhu, X. Zhu and A.-M. Zhu, *Catal. Today*, 2017, **281**, 630–635.

39 B. Toepfer, A. Gora and G. L. Puma, *Appl. Catal., B*, 2006, **68**, 171–180.

40 O. M. Alfano, M. I. Cabrera and A. E. Cassano, *J. Catal.*, 1997, **172**, 370–379.

41 G. Camera-Roda, V. Augugliaro, A. G. Cardillo, V. Loddo, L. Palmisano, F. Parrino and F. Santarelli, *Catal. Today*, 2015, **259**, 87–96.

42 G. Camera-roda, V. Loddo, L. Palmisano and F. Parrino, *Catal. Today*, 2017, **281**, 221–230.

43 C. Minero and D. Vione, *Appl. Catal., B*, 2006, **67**, 257–269.

44 M. M. Ballari, M. Hunger, G. Hüsken and H. J. H. Brouwers, *Appl. Catal., B*, 2010, **95**, 245–254.

45 K. Demeestere, A. De Visscher, J. Dewulf, M. Van Leeuwen and H. Van Langenhove, *Appl. Catal., B*, 2004, **54**, 261–274.

46 Y. Ku, C.-M. Ma and Y.-S. Shen, *Appl. Catal., B*, 2001, **34**, 181–190.

47 C. S. Turchi and D. F. Ollis, *J. Catal.*, 1990, **122**, 178–192.

48 G. E. Imoberdorf, H. A. Irazoqui, A. E. Cassano and O. M. Alfano, *Ind. Eng. Chem. Res.*, 2005, **44**, 6075–6085.

49 R. Terzian, N. Serpone, C. Minero, E. Pelizzetti and H. Hidaka, *J. Photochem. Photobiol., A*, 1990, **55**, 243–249.

50 Y. Yang, Y. Y. Guo, F. Liu, X. Yuan, Y. Y. Guo, S. Zhang, W. Guo and M. Huo, *Appl. Catal., B*, 2013, **142–143**, 828–837.

51 M. L. Satuf, R. J. Brandi, A. E. Cassano and O. M. Alfano, *Appl. Catal., B*, 2008, **82**, 37–49.

52 A. Manassero, M. L. Satuf and O. M. Alfano, *Environ. Sci. Pollut. Res.*, 2015, **22**, 926–937.

53 J. Marugán, R. van Grieken, A. E. Cassano and O. M. Alfano, *Appl. Catal., B*, 2008, **85**, 48–60.

54 R. J. Brandi, G. Rintoul, O. M. Alfano and A. E. Cassano, *Catal. Today*, 2002, **76**, 161–175.

55 M. A. Mueses, F. Machuca-Martinez and G. Li Puma, *Chem. Eng. J.*, 2013, **215–216**, 937–947.

56 A. Tolosana-Moranchel, J. A. Casas, J. Carbajo, M. Faraldos and A. Bahamonde, *Appl. Catal., B*, 2017, **200**, 164–173.

57 C. Casado, J. Marugán, R. Timmers, M. Muñoz and R. van Grieken, *Chem. Eng. J.*, 2017, **310**, 368–380.

58 C. S. Zalazar, M. D. Labas, C. A. Martín, R. J. Brandi, O. M. Alfano and A. E. Cassano, *Chem. Eng. J.*, 2005, **109**, 67–81.

59 C. S. Zalazar, R. L. Romero, C. A. Martín and A. E. Cassano, *Chem. Eng. Sci.*, 2005, **60**, 5240–5254.

60 M. M. Ballari, O. Alfano and A. E. Cassano, *Ind. Eng. Chem. Res.*, 2009, **48**, 1847–1858.

61 F. Salvadores, R. I. Minen, J. Carballada, O. M. Alfano and M. M. Ballari, *Chem. Eng. Technol.*, 2016, **39**, 166–174.

This journal is © The Royal Society of Chemistry 2019

Chem. Soc. Rev., 2019, **48**, 637–682 | 677

62 Q. L. Yu, M. M. Ballari and H. J. H. Brouwers, *Appl. Catal., B*, 2010, **99**, 58–65.

63 C. Passalía, M. E. Martínez Retamar, O. M. Alfano and R. J. Brandi, *Int. J. Chem. React. Eng.*, 2010, **8**, 1–28.

64 C. R. Esterkin, A. C. Negro, O. M. Alfano and A. E. Cassano, *AIChE J.*, 2005, **51**, 2298–2310.

65 G. Li Puma, I. Salvadó-Estivill, T. N. Obee and S. O. Hay, *Sep. Purif. Technol.*, 2009, **67**, 226–232.

66 M. J. Muñoz-Batista, A. Kubacka, M. N. Gómez-Cerezo, D. Tudela and M. Fernández-García, *Appl. Catal., B*, 2013, **140–141**, 626–635.

67 M. J. Muñoz-Batista, M. M. Ballari, A. E. Cassano, O. M. Alfano, A. Kubacka and M. Fernández-García, *Catal. Sci. Technol.*, 2014, **5**, 1521–1531.

68 B. Yu, W. He, N. Li, F. Zhou, Z. Shen, H. Chen and G. Xu, *Build. Environ.*, 2017, **115**, 130–146.

69 H. A. Irazoqui, J. Cerdá and A. E. Cassano, *AIChE J.*, 1973, **19**, 460–467.

70 A. E. Cassano, C. A. Martin, R. J. Brandi and O. M. Alfano, *Ind. Eng. Chem. Res.*, 1995, **34**, 2155–2201.

71 C. A. Parker, *Proc. R. Soc. London, Ser. A*, 1953, **220**, 104–116.

72 H. J. Kuhn, S. E. Braslavsky and R. Schmidt, *Pure Appl. Chem.*, 2004, **76**, 2105–2146.

73 S. L. Murov, I. Carmichael and G. L. Hug, *Handbook of Photochemistry*, Marcel Dekker, New York, 1993.

74 O. M. Alfano, A. E. Cassano, J. Marugán and R. van Grieken, in *Photocatalysis: Fundamentals and Perspectives*, ed. J. Schneider, D. Bahnemann, J. Ye, G. L. Puma and D. D. Dionysiou, The Royal Society of Chemistry, 2016, pp. 351–366.

75 M. N. Ozisik, *Radiative Transfer and Interactions with Conduction and Convection*, John Wiley & Sons, Wiley, New York, 1973.

76 S. E. Braslavsky, A. M. Braun, A. E. Cassano, A. V. Emeline, M. I. Litter, L. Palmisano, V. N. Parmon and N. Serpone, *Pure Appl. Chem.*, 2011, **83**, 931–1014.

77 M. L. Satuf, R. J. Brandi, A. E. Cassano and O. M. Alfano, *Ind. Eng. Chem. Res.*, 2005, **44**, 6643–6649.

78 J. J. Duderstadt and R. Martin, *Transport Theory*, Wiley, New York, 1979.

79 A. Brucato and L. Rizzuti, *Ind. Eng. Chem. Res.*, 1997, **36**, 4740–4747.

80 A. Brucato and L. Rizzuti, *Ind. Eng. Chem. Res.*, 1997, **37**, 4748–4755.

81 A. Brucato, A. E. Cassano, F. Grisafi, G. Montante, L. Rizzuti and G. Vella, *AIChE J.*, 2006, **52**, 3882–3890.

82 H. L. Otálvaro-Marín, M. A. Mueses and F. Machuca-Martínez, *Int. J. Photoenergy*, 2014, 1–8.

83 J. Colina-Márquez, F. Machuca-Martínez and G. Li Puma, *Environ. Sci. Technol.*, 2009, **43**, 8953–8960.

84 A. Busciglio, O. M. Alfano, F. Scargiali and A. Brucato, *Chem. Eng. Sci.*, 2016, **142**, 79–88.

85 R. Siegel and J. R. Howell, *Thermal Radiation Heat Transfer*, Taylor & Francis, New York, 2002.

86 M. F. Modest, *Radiative Heat Transfer*, Academic Press, New York, 2003.

87 G. Camera Roda and F. Santarelli, *Ind. Eng. Chem. Res.*, 2007, **46**, 7637–7644.

88 V. Pareek, S. Chong, M. Tadé and A. A. Adesina, *Asia-Pac. J. Chem. Eng.*, 2008, **3**, 171–201.

89 G. Spadoni, E. Bandini and F. Santarelli, *Chem. Eng. Sci.*, 1978, **33**, 517–524.

90 J. Moreira, B. Serrano, A. Ortiz and H. de Lasa, *Ind. Eng. Chem. Res.*, 2010, **49**, 10524–10534.

91 G. E. Imoberdorf, F. Taghipour, M. Keshmiri and M. Mohseni, *Chem. Eng. Sci.*, 2008, **63**, 4228–4238.

92 M. M. Ballari, R. Brandi, O. Alfano and A. Cassano, *Chem. Eng. J.*, 2008, **136**, 242–255.

93 J. Marugán, R. van Grieken, C. Pablos, M. L. Satuf and A. E. Cassano, *Chem. Eng. J.*, 2013, **224**, 39–45.

94 J. Marugán, R. van Grieken, A. E. Cassano and O. M. Alfano, *Catal. Today*, 2007, **129**, 143–151.

95 O. Fontelles-Carceller, M. J. Muñoz-Batista, J. C. Conesa, M. Fernández-García and A. Kubacka, *Appl. Catal., B*, 2017, **216**, 133–145.

96 S. M. Zacarías, M. L. Satuf, M. C. Vaccari and O. M. Alfano, *Ind. Eng. Chem. Res.*, 2012, **51**, 13599–13608.

97 G. Vella, G. E. Imoberdorf, A. Sclafani, A. E. Cassano, O. M. Alfano and L. Rizzuti, *Appl. Catal., B*, 2010, **96**, 399–407.

98 M. Briggiler Marcó, A. del, L. Quiberoni, A. C. Negro, J. A. Reinheimer and O. M. Alfano, *Chem. Eng. J.*, 2011, **172**, 987–993.

99 M. J. Muñoz-Batista, A. Kubacka, A. B. Hungría and M. Fernández-García, *J. Catal.*, 2015, **330**, 154–166.

100 D. K. Edwards, *Sol. Energy*, 1977, **19**, 401–402.

101 G. E. Imoberdorf, G. Vella, A. Sclafani, L. Rizzuti, O. M. Alfano and A. E. Cassano, *AIChE J.*, 2010, **56**, 1030–1044.

102 A. L. L. Zazueta, H. Destaillats and G. Li Puma, *Chem. Eng. J.*, 2013, **217**, 475–485.

103 J. Marugán, R. van Grieken, C. Pablos, M. L. Satuf, A. E. Cassano and O. M. Alfano, *Catal. Today*, 2015, **252**, 143–149.

104 U. Caudillo-Flores, M. Muñoz-Batista, A. Kubacka and M. Fernández-García, *ChemPhotoChem*, 2018, **2**, 777–785.

105 J. Schneider, M. Matsuoka, M. Takeuchi, J. Zhang, Y. Horiuchi, M. Anpo and D. W. Bahnemann, *Chem. Rev.*, 2014, **114**, 9919–9986.

106 H. A. Foster, I. B. Ditta, S. Varghese and A. Steele, *Appl. Microbiol. Biotechnol.*, 2011, **90**, 1847–1868.

107 Z. Wang, W. Ma, C. Chen, H. Ji and J. Zhao, *Chem. Eng. J.*, 2011, **170**, 353–362.

108 T. Rajh, N. M. Dimitrijevic, M. Bissonnette, T. Koritarov and V. Konda, *Chem. Rev.*, 2014, **114**, 10177–10216.

109 R. F. Howe and M. Gratzel, *J. Phys. Chem.*, 1987, **91**, 3906–3909.

110 O. Micic, Y. Zhang, K. R. Cromack, A. Trifunac and M. Thurnauer, *J. Phys. Chem.*, 1993, **97**, 13284–13288.

111 O. I. Micic, Y. Zhang, K. R. Cromack, A. D. Trifunac and M. C. Thurnauer, *J. Phys. Chem.*, 1993, **97**, 7277–7283.

112 Y. Nakaoka and Y. Nosaka, *J. Photochem. Photobiol., A*, 1997, **110**, 299–305.

678 | *Chem. Soc. Rev.*, 2019, **48**, 637–682

This journal is © The Royal Society of Chemistry 2019

113 D. C. Hurum, A. G. Agrios, K. A. Gray, T. Rajh and M. C. Thurnauer, *J. Phys. Chem. B*, 2003, **107**, 4545–4549.

114 T. Berger, M. Sterrer, O. Diwald, E. Knözinger, D. Panayotov, A. T. L. Thompson, J. J. T. Yates, O. Diwald, E. Knözinger, D. Panayotov, T. L. Thompson and J. J. T. Yates, *J. Phys. Chem. B*, 2005, **109**, 6061–6068.

115 M. Fittipaldi and D. Gatteschi, *Catal. Today*, 2013, **206**, 2–11.

116 T. Rajh, O. G. Poluektov and M. C. Thurnauer, *Chemical Physics of Nanostructured Semiconductors*, VSP, Utrecht&Boston, 2003, pp. 1–31.

117 I. R. Macdonald, S. Rhydderch, E. Holt, N. Grant, J. M. D. Storey and R. F. Howe, *Catal. Today*, 2012, **182**, 39–45.

118 T. Tachikawa and T. Majima, *J. Am. Chem. Soc.*, 2009, **131**, 8485–8495.

119 C. Mercado, Z. Seeley, A. Bandyopadhyay, S. Bose and J. L. McHale, *ACS Appl. Mater. Interfaces*, 2011, **3**, 2281–2288.

120 J. Zhang and Y. Nosaka, *J. Phys. Chem. C*, 2013, **117**, 1383–1391.

121 A. Kubacka, M. Ferrer, A. Martínez-Arias and M. Fernández-García, *Appl. Catal., B*, 2008, **84**, 87–93.

122 Y. Nosaka, S. Komori, K. Yawata, T. Hirakawa and A. Y. Nosaka, *Phys. Chem. Chem. Phys.*, 2003, **5**, 4731–4735.

123 G. Mamba and A. K. Mishra, *Appl. Catal., B*, 2016, **198**, 347–377.

124 W.-J. Ong, L.-L. Tan, Y. H. Ng, S.-T. Yong and S.-P. Chai, *Chem. Rev.*, 2016, **116**, 7159–7329.

125 M. J. Muñoz-Batista, O. Fontelles-Carceller, M. Ferrer, M. Fernández-García and A. Kubacka, *Appl. Catal., B*, 2016, **183**, 86–95.

126 Z. Lu, L. Zeng, W. Song, Z. Qin, D. Zeng and C. Xie, *Appl. Catal., B*, 2017, **202**, 489–499.

127 S. Liu, D. Li, H. Sun, H. M. Ang, M. O. Tadé and S. Wang, *J. Colloid Interface Sci.*, 2016, **468**, 176–182.

128 R. F. Howe and M. Gratzel, *J. Phys. Chem.*, 1985, **89**, 4495–4499.

129 M. Chiesa, M. C. Paganini, S. Livraghi and E. Giamello, *Phys. Chem. Chem. Phys.*, 2013, **15**, 9435.

130 S. Livraghi, M. Rolando, S. Maurelli, M. Chiesa, M. C. Paganini and E. Giamello, *J. Phys. Chem. C*, 2014, **118**, 22141–22148.

131 T. Xia and X. Chen, *J. Mater. Chem. A*, 2013, **1**, 2983.

132 X. Chen, L. Liu and F. Huang, *Chem. Soc. Rev.*, 2015, **44**, 1861–1885.

133 L. Lin, J. Huang, X. Li, M. A. Abass and S. Zhang, *Appl. Catal., B*, 2017, **203**, 615–624.

134 D. C. Hurum, K. A. Gray, T. Rajh, M. C. Thurnauer, D. C. H. And, K. A. Gray, T. R. And and M. C. Thurnauer, *J. Phys. Chem. B*, 2004, **109**, 977–980.

135 G. Li, N. M. Dimitrijevic, L. Chen, J. M. Nichols, T. Rajh and K. A. Gray, *J. Am. Chem. Soc.*, 2008, **130**, 5402–5403.

136 Z. Zheng, H. Liu, J. Ye, J. Zhao, E. R. Waclawik and H. Zhu, *J. Mol. Catal. A: Chem.*, 2010, **316**, 75–82.

137 M. Che and A. J. Tench, *Adv. Catal.*, 1983, **32**, 1–148.

138 K. Sobańska, A. Krasowska, T. Mazur, K. Podolska-Serafin, P. Pietrzyk and Z. Sojka, *Top. Catal.*, 2015, **58**, 796–810.

139 M. J. Elser and O. Diwald, *J. Phys. Chem. C*, 2012, **116**, 2896–2903.

140 R. Nakamura, Y. Nakato, R. Nakamura and Y. Nakato, *J. Am. Chem. Soc.*, 2004, **126**, 1290–1298.

141 Y. Kakuma, A. Y. Nosaka and Y. Nosaka, *Phys. Chem. Chem. Phys.*, 2015, **17**, 18691–18698.

142 Y.-F. Li, U. Aschauer, J. Chen and A. Selloni, *Acc. Chem. Res.*, 2014, **47**, 3361–3368.

143 M. Che, E. Giamello and A. J. Tench, *Colloids Surf.*, 1985, **13**, 231–248.

144 K. Komaguchi, T. Maruoka, H. Nakano, I. Imae, Y. Ooyama and Y. Harima, *J. Phys. Chem. C*, 2009, **113**, 1160–1163.

145 V. Brezová, Z. Barbieriková, M. Zukalová, D. Dvoranová and L. Kavan, *Catal. Today*, 2014, **230**, 112–118.

146 J. Green, E. Carter and D. M. Murphy, *Chem. Phys. Lett.*, 2009, **477**, 340–344.

147 J. Yang, C. Chen, H. Ji, W. Ma and J. Zhao, *J. Phys. Chem. B*, 2005, **109**, 21900–21907.

148 S. Dikalov, J. Jiang and R. P. Mason, *Free Radical Res.*, 2005, **39**, 825–836.

149 K. Ishibashi, A. Fujishima, T. Watanabe, K. Hashimoto, Ken-ichi Ishibashi, A. Fujishima, T. Watanabe and K. Hashimoto, *J. Phys. Chem. B*, 2000, **104**, 4934–4938.

150 J. B. Priebe, M. Karnahl, H. Junge, M. Beller, D. Hollmann and A. Brückner, *Angew. Chem., Int. Ed.*, 2013, **52**, 11420–11424.

151 T. Tachikawa, T. Yonezawa and T. Majima, *ACS Nano*, 2013, **7**, 263–275.

152 H. Irie, K. Kamiya, T. Shibanuma, S. Miura, D. A. Tryk, T. Yokoyama and K. Hashimoto, *J. Phys. Chem. C*, 2009, **113**, 10761–10766.

153 L. Liu, C. Zhao, J. T. Miller and Y. Li, *J. Phys. Chem. C*, 2017, **121**, 490–499.

154 D. Lahiri, V. Subramanian, B. A. Bunker and P. V. Kamat, *J. Chem. Phys.*, 2006, **124**, 204720.

155 Y. H. Li, C. Li and H. G. Yang, *J. Mater. Chem. A*, 2017, **5**, 20631–20634.

156 L. Amidani, A. Naldoni, M. Malvestuto, M. Marelli, P. Glatzel, V. Dal Santo and F. Boscherini, *Angew. Chem., Int. Ed.*, 2015, **54**, 5413–5416.

157 J. B. Priebe, J. Radnik, C. Kreyenschulte, A. J. J. Lennox, H. Junge, M. Beller and A. Brückner, *ChemCatChem*, 2017, **9**, 1025–1031.

158 M. J. Muñoz-Batista, D. Motta Meira, G. Colón, A. Kubacka and M. Fernández-García, *Angew. Chem., Int. Ed.*, 2018, **57**, 1199–1203.

159 Y. Nosaka, T. Daimon, A. Y. Nosaka and Y. Murakami, *Phys. Chem. Chem. Phys.*, 2004, **6**, 2917.

160 T. A. Konovalova, J. Lawrence and L. D. Kispert, *J. Photochem. Photobiol., A*, 2004, **162**, 1–8.

161 V. Brezová, P. Billik, Z. Vrecková and G. Plesch, *J. Mol. Catal. A: Chem.*, 2010, **327**, 101–109.

162 Y. Nosaka, M. Nishikawa and A. Nosaka, *Molecules*, 2014, **19**, 18248–18267.

163 C. Murata, T. Hattori and H. Yoshida, *J. Catal.*, 2005, **231**, 292–299.

This journal is © The Royal Society of Chemistry 2019

Chem. Soc. Rev., 2019, **48**, 637–682 | **679**

164 H. Chen, C. E. Nanayakkara and V. H. Grassian, *Chem. Rev.*, 2012, **112**, 5919–5948.

165 A. J. Maira, J. M. Coronado, V. Augugliaro, K. L. Yeung, J. C. Conesa and J. Soria, *J. Catal.*, 2001, **420**, 413–420.

166 S. Sun, J. Ding, J. Bao, C. Gao, Z. Qi, X. Yang, B. He and C. Li, *Appl. Surf. Sci.*, 2012, **258**, 5031–5037.

167 F. Zhang, X. Zhu, J. Ding, Z. Qi, M. Wang, S. Sun, J. Bao and C. Gao, *Catal. Lett.*, 2014, **144**, 995–1000.

168 M. Nagao and Y. Suda, *Langmuir*, 1989, **5**, 42–47.

169 F. Zhang, M. Wang, X. Zhu, B. Hong, W. Wang, Z. Qi, W. Xie, J. Ding, J. Bao, S. Sun and C. Gao, *Appl. Catal., B*, 2015, **170–171**, 215–224.

170 J. M. Coronado and J. Soria, *Catal. Today*, 2007, **123**, 37–41.

171 L. Cao, Z. Gao, S. L. Suib, T. N. Obee, S. O. Hay and J. D. Freihaut, *J. Catal.*, 2000, **196**, 253–261.

172 S. V. Awate, R. K. Sahu, M. D. Kadgaonkar, R. Kumar and N. M. Gupta, *Catal. Today*, 2009, **141**, 144–151.

173 L.-C. Chen, G.-T. Pan, T. C.-K. Yang, T.-W. Chung and C.-M. Huang, *J. Hazard. Mater.*, 2010, **178**, 644–651.

174 G. R. Bertolini, L. R. Pizzio, A. Kubacka, M. J. Muñoz-Batista and M. Fernández-García, *Appl. Catal., B*, 2018, **225**, 100–109.

175 U. Caudillo-Flores, M. J. Muñoz-Batista, F. Ung-Medina, G. Alonso-Núñez, A. Kubacka, J. A. Cortés and M. Fernández-García, *Chem. Eng. J.*, 2016, **299**, 393–402.

176 V. Augugliaro, S. Coluccia, V. Loddo, L. Marchese, G. Martra, L. Palmisano and M. Schiavello, *Appl. Catal., B*, 1999, **20**, 15–27.

177 G. Marcì, M. Addamo, V. Augugliaro, S. Coluccia, E. García-López, V. Loddo, G. Martra, L. Palmisano and M. Schiavello, *J. Photochem. Photobiol., A*, 2003, **160**, 105–114.

178 R. Méndez-Román and N. Cardona-Martínez, *Catal. Today*, 1998, **40**, 353–365.

179 M. Fernández-García, A. Fuerte, M. D. Hernández-Alonso, J. Soria and A. Martínez-Arias, *J. Catal.*, 2007, **245**, 84–90.

180 A. R. Almeida, J. A. Moulijn, G. Mul, J. A. Moulijn and G. Mul, *J. Phys. Chem. C*, 2008, **112**, 1552–1561.

181 M. D. Hernández-Alonso, A. R. Almeida, J. A. Moulijn and G. Mul, *Catal. Today*, 2009, **143**, 326–333.

182 J. T. Carneiro, C.-C. Yang, J. A. Moma, J. A. Moulijn and G. Mul, *Catal. Lett.*, 2009, **129**, 12–19.

183 A. R. Almeida, J. A. Moulijn and G. Mul, *J. Phys. Chem. C*, 2011, **115**, 1330–1338.

184 X. Yang, Y. Cao, H. Yu, H. Huang, H. Wang and F. Peng, *Catal. Sci. Technol.*, 2017, **7**, 4431–4436.

185 T. van der Meulen, A. Mattson and L. Österlund, *J. Catal.*, 2007, **251**, 131–144.

186 A. A. Davydov, *Infrared spectroscopy of adsorbed species on the surface of transition metal oxides*, Wiley, 1990.

187 B. D. Fraters, R. Amrollahi and G. Mul, *J. Catal.*, 2015, **324**, 119–126.

188 T. Chen, Z. Feng, G. Wu, J. Shi, G. Ma, A. Pinliang Ying and C. Li, *J. Phys. Chem. C*, 2007, **111**, 8005–8014.

189 U. Diebold, *Surf. Sci. Rep.*, 2003, **48**, 53–229.

190 O. Fontelles-Carceller, M. J. Muñoz-Batista, E. Rodríguez-Castellón, J. C. Conesa, M. Fernández-García and A. Kubacka, *J. Catal.*, 2017, **347**, 157–169.

191 M. El-Roz, P. Bazin, M. Daturi and F. Thibault-Starzyk, *Phys. Chem. Chem. Phys.*, 2015, **17**, 11277–11283.

192 M. El-Roz, P. Bazin, M. Daturi and F. Thibault-Starzyk, *ACS Catal.*, 2013, **3**, 2790–2798.

193 J. M. Coronado, S. Kataoka, I. Tejedor-Tejedor and M. A. Anderson, *J. Catal.*, 2003, **219**, 219–230.

194 Z. Yu and S. S. C. Chuang, *J. Catal.*, 2007, **246**, 118–126.

195 D. V. Kozlov, E. A. Paukshtis and E. N. Savinov, *Appl. Catal., B*, 2000, **24**, L7–L12.

196 A. C. Sola, D. Garzón Sousa, J. Araña, O. González Díaz, J. M. Doña Rodríguez, P. Ramírez de la Piscina and N. Homs, *Catal. Today*, 2016, **266**, 53–61.

197 S. Obregón, M. J. Muñoz-Batista, M. Fernández-García, A. Kubacka and G. Colón, *Appl. Catal., B*, 2015, **179**, 468–478.

198 O. Fontelles-Carceller, M. J. Muñoz-Batista, J. C. Conesa, A. Kubacka and M. Fernández-García, *Mol. Catal.*, 2018, **446**, 88–97.

199 M. Zhang, Q. Wang, C. Chen, L. Zang, W. Ma and J. Zhao, *Angew. Chem., Int. Ed.*, 2009, **48**, 6081–6084.

200 A. Yamakata, Taka-aki Ishibashi and H. Onishi, *J. Phys. Chem. B*, 2002, **106**, 9122–9125.

201 D. A. Panayotov, S. P. Burrows and J. R. Morris, *J. Phys. Chem. C*, 2012, **116**, 6623–6635.

202 A. Mattsson and L. Österlund, *J. Phys. Chem. C*, 2010, **114**, 14121–14132.

203 C. E. Nanayakkara, J. K. Dillon and V. H. Grassian, *J. Phys. Chem. C*, 2014, **118**, 25487–25495.

204 J. G. Highfield, M. H. Chen, P. T. Nguyen and Z. Chen, *Energy Environ. Sci.*, 2009, **2**, 991–1002.

205 H. Zhang, P. Zhou, H. Ji, W. Ma, C. Chen and J. Zhao, *Appl. Catal., B*, 2018, **224**, 376–382.

206 J. Hansen, R. Bebensee, U. Martinez, S. Porsgaard, E. Lira, Y. Wei, L. Lammich, Z. Li, H. Idriss, F. Besenbacher, B. Hammer and S. Wendt, *Sci. Rep.*, 2016, **6**, 1–11.

207 G. M. Haselmann and D. Eder, *ACS Catal.*, 2017, **7**, 4668–4675.

208 T. H. Tan, J. Scott, Y. H. Ng, R. A. Taylor, K.-F. Aguey-Zinsou and R. Amal, *ACS Catal.*, 2016, **6**, 8021–8029.

209 M. J. Muñoz-Batista, U. Caudillo-Flores, F. Ung-Medina, M. del Carmen Chávez-Parga, J. A. Cortés, A. Kubacka and M. Fernández-García, *Appl. Catal., B*, 2017, **201**, 400–410.

210 F. Arsac, D. Bianchi, J. M. Chovelon, C. Ferronato and J. M. Herrmann, *J. Phys. Chem. A*, 2006, **110**, 4202–4212.

211 F. Arsac, D. Bianchi, J. M. Chovelon, C. Ferronato and J. M. Herrmann, *J. Phys. Chem. A*, 2006, **110**, 4213–4222.

212 P. F. Rossi, G. Busca, V. Lorenzelli, O. Saur and J. C. Lavalley, *Langmuir*, 1987, **3**, 52–58.

213 V. Augugliaro, H. Kisch, V. Loddo, M. J. López-Muñoz, C. Márquez-Alvarez, G. Palmisano, L. Palmisano, F. Parrino and S. Yurdakal, *Appl. Catal., A*, 2008, **349**, 189–197.

214 C. Keresszegi, D. Ferri, T. Mallat and A. Baiker, *J. Phys. Chem. B*, 2004, **109**, 958–967.

215 H. Lampert, W. Mikenda and A. Karpfen, *J. Phys. Chem. A*, 1997, **101**, 2254–2263.

216 A. M. Johnson, S. Trakhtenberg, A. S. Cannon and J. C. Warner, *J. Phys. Chem. A*, 2007, **111**, 8139–8146.

680 | *Chem. Soc. Rev.*, 2019, **48**, 637–682

This journal is © The Royal Society of Chemistry 2019

217 K. S. Finnie, J. R. Bartlett and J. L. Woolfrey, *Langmuir*, 1998, **14**, 2744–2749.

218 G. Y. Popova, T. V. Andrushkevich, Y. A. Chesalov and E. S. Stoyanov, *Kinet. Catal.*, 2000, **41**, 805–811.

219 S. Sun, J. Ding, J. Bao, C. Gao, Z. Qi and C. Li, *Catal. Lett.*, 2010, **137**, 239–246.

220 C. Zhang, H. He and K. Tanaka, *Appl. Catal., B*, 2006, **65**, 37–43.

221 J. Raskó, T. Kecskés and J. Kiss, *J. Catal.*, 2004, **226**, 183–191.

222 X. Zhu, C. Jin, X.-S. Li, J.-L. Liu, Z.-G. Sun, C. Shi, X. Li and A.-M. Zhu, *ACS Catal.*, 2017, **7**, 6514–6524.

223 Z. Topalian, B. I. Stefanov, C. G. Granqvist and L. Österlund, *J. Catal.*, 2013, **307**, 265–274.

224 M. D. Hernández-Alonso, I. Tejedor-Tejedor, J. M. Coronado, M. A. Anderson and J. Soria, *Catal. Today*, 2009, **143**, 364–373.

225 E. Carter, A. F. Carley and D. M. Murphy, *ChemPhysChem*, 2007, **8**, 113–123.

226 H. Uetsuka, M. A. Henderson, A. Sasahara and H. Onishi, *J. Phys. Chem. B*, 2004, **108**, 13706–13710.

227 Li-Fen Liao, Wen-Chun Wu, Chia-Yuan Chen and J.-L. Lin, *J. Phys. Chem. B*, 2001, **105**, 7678–7685.

228 S.-Z. Chu, S. Inoue, K. Wada, D. Li and H. Haneda, *J. Mater. Chem.*, 2003, **13**, 866–870.

229 L. Österlund, A. Mattsson and P. O. Andersson, *Nanostructured Materials and Nanotechnology II: Ceramic Engineering and Science Proceedings*, Wiley-Blackwell, 2009, pp. 19–35.

230 B. Kraeutler and A. J. Bard, *J. Am. Chem. Soc.*, 1978, **100**, 5985–5992.

231 N. M. Dimitrijevic, I. A. Shkrob, D. J. Gosztola and T. Rajh, *J. Phys. Chem. C*, 2012, **116**, 878–885.

232 J. Araña, O. González Díaz, M. Miranda Saracho, J. M. Doña Rodríguez, J. A. Herrera Melián and J. Pérez Peña, *Appl. Catal., B*, 2001, **32**, 49–61.

233 R. Eisenberg and D. E. Hendriksen, *Adv. Catal.*, 1979, **28**, 79–172.

234 F. P. Rotzinger, J. M. Kesselman-Truttmann, S. J. Hug, V. Shklover and M. Grätzel, *J. Phys. Chem. B*, 2004, **108**, 5004–5017.

235 L.-F. Liao, C.-F. Lien and J.-L. Lin, *Phys. Chem. Chem. Phys.*, 2001, **3**, 3831–3837.

236 Y. Nosaka, M. Kishimoto and J. Nishino, *J. Phys. Chem. B*, 1998, **102**, 10279–10283.

237 G. N. Ekström and A. J. McQuillan, *J. Phys. Chem. B*, 1999, **103**, 10562–10565.

238 K. D. Dobson, P. A. Connor and A. J. McQuillan, *J. Phys. Chem. B*, 1997, **102**, 10279–10283.

239 I. Dolamic and T. Bürgi, *J. Catal.*, 2007, **248**, 268–276.

240 I. Dolamic and T. Bürgi, *J. Phys. Chem. B*, 2006, **110**, 14898–14904.

241 M. Zhang, C. Chen, W. Ma and J. Zhao, *Angew. Chem., Int. Ed.*, 2008, **47**, 9730–9733.

242 Z. Yu and S. S. C. Chuang, *J. Phys. Chem. C*, 2007, **111**, 13813–13820.

243 T. C.-K. Yang, S.-F. Wang, S. H.-Y. Tsai and S.-Y. Lin, *Appl. Catal., B*, 2001, **30**, 293–301.

244 S. Tefan Neat, J. A. Maciaagullo, P. Concepcio and H. Garcia, *J. Am. Chem. Soc.*, 2014, **136**, 15969–15976.

245 C.-C. Yang, Y.-H. Yu, B. van der Linden, J. C. S. Wu and G. Mul, *J. Am. Chem. Soc.*, 2010, **132**, 8398–8406.

246 V. F. Kiselev and O. V. Krylov, *Adsorption and Catalysis on Oxides of Transition Metals*, Springer Berlin Heidelberg, 1989.

247 J. C. S. Wu and Y.-T. Cheng, *J. Catal.*, 2006, **237**, 393–404.

248 C.-H. Lin and H. Bai, *Ind. Eng. Chem. Res.*, 2004, **43**, 5983–5988.

249 I. Nakamura, S. Sugihara and K. Takeuchi, *Chem. Lett.*, 2000, 1276–1277.

250 G. Ramis, G. Busca, F. Bregani and P. Forzatti, *Appl. Catal.*, 1990, **64**, 259–278.

251 M. M. Kantcheva, V. P. Bushev and K. I. Hadjiivanov, *J. Chem. Soc., Faraday Trans.*, 1992, **88**, 3087.

252 R. Nakamura, A. Imanishi, A. Kei Murakoshi and Y. Nakato, *J. Am. Chem. Soc.*, 2003, **125**, 7443–7450.

253 M. A. Debeila, N. J. Coville, M. S. Scurrell, G. R. Hearne and M. J. Witcomb, *J. Phys. Chem. B*, 2004, **108**, 18254–18260.

254 X. Dong, W. Zhang, Y. Sun, J. Li, W. Cen, Z. Cui, H. Huang and F. Dong, *J. Catal.*, 2018, **357**, 41–50.

255 X. Li, W. Zhang, W. Cui, Y. Sun, G. Jiang, Y. Zhang, H. Huang and F. Dong, *Appl. Catal., B*, 2018, **221**, 482–489.

256 X. Li, X. Yan, X. Lu, S. Zuo, Z. Li, C. Yao and C. Ni, *J. Catal.*, 2018, **357**, 59–68.

257 J. A. Anderson, *Catal. Today*, 2012, **181**, 171–176.

258 M. Shand and J. A. Anderson, *Catal. Sci. Technol.*, 2013, **3**, 879.

259 J. F. Montoya, I. Ivanova, R. Dillert, D. W. Bahnemann, P. Salvador and J. Peral, *J. Phys. Chem. Lett.*, 2013, **4**, 1415–1422.

260 J. M. Kesselman, N. S. Lewis and M. R. Hoffmann, *Environ. Sci. Technol.*, 1997, **31**, 2298–2302.

261 X. H. Lin, Y. Miao and S. F. Y. Li, *Catal. Sci. Technol.*, 2017, **7**, 441–451.

262 W. Choi and M. R. Hoffmann, *Environ. Sci. Technol.*, 1995, **29**, 1646–1654.

263 J. Cunningham and S. Srijaranai, *J. Photochem. Photobiol., A*, 1988, **43**, 329–335.

264 G. Yin, X. Huang, T. Chen, W. Zhao, Q. Bi, J. Xu, Y. Han and F. Huang, *ACS Catal.*, 2018, **8**, 1009–1017.

265 G. L. Chiarello, D. Ferri and E. Selli, *J. Catal.*, 2011, **280**, 168–177.

266 L. Rideh, A. Wehrer, D. Ronze and A. Zoulalian, *Ind. Eng. Chem. Res.*, 1997, **36**, 4712–4718.

267 D. Spasiano, R. Marotta, I. Gargano, I. Di Somma, G. Vitiello, G. D'Errico and R. Andreozzi, *Chem. Eng. J.*, 2014, **249**, 130–142.

268 M. Antonopoulou, A. Giannakas, Y. Deligiannakis and I. Konstantinou, *Chem. Eng. J.*, 2013, **231**, 314–325.

269 Q. Gu, J. Long, L. Fan, L. Chen, L. Zhao, H. Lin and X. Wang, *J. Catal.*, 2013, **303**, 141–155.

This journal is © The Royal Society of Chemistry 2019

Chem. Soc. Rev., 2019, **48**, 637–682 | 681

270 M. J. Muñoz-Batista, M. N. Gómez-Cerezo, A. Kubacka, D. Tudela and M. Fernández-García, *ACS Catal.*, 2014, **4**, 63–72.

271 M. J. Muñoz-Batista, A. Kubacka and M. Fernández-García, *ACS Catal.*, 2014, **4**, 4277–4288.

272 J. M. Coronado, M. E. Zorn, I. Tejedor-Tejedor and M. A. Anderson, *Appl. Catal., B*, 2003, **43**, 329–344.

273 C. B. Mendive, D. W. Bahnemann and M. A. Blesa, *Catal. Today*, 2005, **101**, 237–244.

274 G. Mul, W. Wasylenko, M. S. Hamdy and H. Frei, *Phys. Chem. Chem. Phys.*, 2008, **10**, 3131–3137.

275 W. Xu, D. Raftery and J. S. Francisco, *J. Phys. Chem. B*, 2003, **107**, 4537–4544.

276 A. Mattsson, M. Leideborg, K. Larsson, G. Westing and L. Österlund, *J. Phys. Chem. B*, 2006, **110**, 1210–1220.

277 J. Henych, V. Štengl, A. Mattsson and L. Österlund, *Photochem. Photobiol.*, 2015, **91**, 48–58.

278 X. Yan, Y. Xu, B. Tian, J. Lei, J. Zhang and L. Wang, *Appl. Catal., B*, 2018, **224**, 305–309.

279 X. L. Wang, W. Liu, Y.-Y. Yu, Y. Song, W. Q. Fang, D. Wei, X.-Q. Gong, Y.-F. Yao and H. G. Yang, *Nat. Commun.*, 2016, **7**, 11918.

682 | *Chem. Soc. Rev.*, 2019, **48**, 637–682

This journal is © The Royal Society of Chemistry 2019